

ANALYSIS OF SHALLOW BURIED REINFORCED CONCRETE BOX STRUCTURES
SUBJECTED TO AIRBLAST LOADS

By

KAY HYANG CHEE

A THESIS PRESENTED TO THE GRADUATE SCHOOL
OF THE UNIVERSITY OF FLORIDA IN PARTIAL FULFILLMENT
OF THE REQUIREMENTS FOR THE DEGREE OF
MASTER OF SCIENCE

UNIVERSITY OF FLORIDA

2008

© 2008 Kay Hyang Chee

To my lovely wife

ACKNOWLEDGMENTS

I thank my advisor, Dr Theodor Krauthammer, for his advice and guidance. I want to express my appreciation to Dr Serdar Astarlioglu for his valuable suggestions and help in the programming aspects. I am grateful to the Defence Science and Technology Agency, Singapore, for the postgraduate scholarship. I thank all of my friends at the Center for Infrastructure Protection and Physical Security, University of Florida and Maguire Village, for a great stay and experience in Gainesville.

Last of all, I thank my dear wife, Hiong Suan, for all she has done for me and her willingness to sacrifice many things over the last two years.

TABLE OF CONTENTS

	<u>page</u>
ACKNOWLEDGMENTS	4
LIST OF TABLES	7
LIST OF FIGURES	8
LIST OF SYMBOLS	12
ABSTRACT.....	16
CHAPTER	
1 INTRODUCTION.....	17
1.1 Problem Statement	17
1.2 Objectives and Scope	18
1.3 Research Significance	18
2 BACKGROUND AND LITERATURE REVIEW	19
2.1 Introduction.....	19
2.2 Blast Loads.....	19
2.2.1 Airblast from High Explosive	20
2.2.2 Nuclear Devices	21
2.3 Effects on Buried Structures	22
2.3.1 Soil Arching Effect	22
2.4 Dynamic Structural Behavior and Analysis.....	24
2.4.1 Single-Degree-of-Freedom (SDOF) System.....	27
2.4.2 Transformation Factors for Equivalent SDOF	28
2.4.3 Numerical Integration (Newmark-Beta method)	29
2.5 Behavior of Reinforced Concrete Slabs.....	30
2.5.1 Flexural Behavior: Johansen's Yield Line Theory	30
2.5.2 Flexural Behavior: Membrane Action	31
2.5.3 Slab Compressive Membrane	33
2.5.4 Slab Tensile Membrane.....	38
2.5.5 Reinforced Concrete Slab Flexural Model.....	39
2.5.6 Direct Shear Behavior	40
2.5.7 Hawkins Shear Model.....	41
2.5.8 Dynamic Resistance Function and Response.....	43
2.6 Pressure-Impulse Diagrams and their Application	46
2.6.1 Characteristics of P-I Diagram.....	46
2.6.2 Numerical Approach to P-I Diagram	48
2.6.3 Multiple Failure Modes.....	48
2.7 Summary	50

3	METHODOLOGY	51
3.1	Introduction.....	51
3.2	Flexural Mode.....	51
3.2.1	Externally Applied Thrust.....	51
3.2.2	Numerical Approach for Resistance Curve Calculation	54
3.2.3	Variation of Mass and Load Factor.....	58
3.3	Soil Structural Interaction	60
3.3.1	Influence of Parameters on Soil Arching Effect	60
3.3.2	Effect on SDOF Load and Mass Factor	61
3.4	Direct Shear Mode	65
3.4.1	Resistance Curve.....	65
3.4.2	Shear Mass and Load Factors	67
3.5	Shear Failure Mode for Slab	68
3.6	Program Flowchart.....	70
3.7	Summary	70
4	RESULTS AND DISCUSSIONS.....	73
4.1	Introduction.....	73
4.2	Validation with Experimental Data.....	73
4.2.1	Test FH1.....	74
4.2.2	Test FH2.....	77
4.2.3	Test FH3.....	81
4.2.4	Test FH4.....	84
4.2.5	Test FH5.....	88
4.2.6	Test FH6.....	92
4.2.7	Summary	96
4.3	Assessment by P-I Diagrams	96
4.4	Summary	100
5	CONCLUSIONS AND RECOMMENDATIONS	101
5.1	Summary	101
5.2	Conclusions.....	101
5.3	Recommendations for Future Study	102
	APPENDIX EXPERIMENT TEST ON SHALLOW BURIED FLAT ROOF STRUCTURES	103
	LIST OF REFERENCES.....	113
	BIOGRAPHICAL SKETCH	115

LIST OF TABLES

<u>Table</u>		<u>page</u>
4-1	Summary of results	96
A-1	Parameters for FoamHest tests.....	106
A-2	Test FH1 input parameters.....	107
A-3	Test FH2 input parameters.....	108
A-4	Test FH3 input parameters.....	109
A-5	Test FH4 input parameters.....	110
A-6	Test FH5 input parameters.....	111
A-7	Test FH6 input parameters.....	112

LIST OF FIGURES

<u>Figure</u>	<u>page</u>
2-1 Blast pressure-time curve.....	21
2-2 Soil arching demonstrated by trap door experiment.....	23
2-3 Soil arching as function of depth of burial.....	24
2-4 Uniform beam subject to arbitrary load.....	25
2-5 Yield lines development in a uniformly loaded simply supported slab.....	31
2-6 Load-deflection curve for two-way RC slab with laterally restrained edges.....	33
2-7 Assumed yield line pattern for uniformly loaded slab with restrained edges.....	34
2-8 Plastic hinges of a restrained strip	34
2-9 Portion of strip between plastic hinges	35
2-10 Conditions at positive moment yield section	37
2-11 Uniformly loaded plastic tensile membrane.....	39
2-11 Flexural resistance model for slab.....	40
2-13 Slab in direct shear failure mode	41
2-14 Hawkins model for direct shear stress-slip relationship.....	42
2-15 Equivalent SDOF systems for structural element.....	44
2-16 Dynamic flexural resistance functions.....	45
2-17 Dynamic direct shear resistance function.....	46
2-18 Typical response spectra and P-I diagram	47
2-19 Search algorithm for P-I diagram	49
2-20 Pressure-Impulse diagram with two failure modes.....	49
3-1 Model for externally applied thrust.....	52
3-2 Calculation of externally applied thrust.....	53
3-3 Stress and strain distributions across reinforced concrete section.....	54

3-4	Restrained strip with external thrust	55
3-5	Portion of strip between plastic hinges with external thrust	55
3-6	Variation of load and mass factor	58
3-7	Variation of soil arching factor with friction angle and burial depth	61
3-9	Variation of λ_L	63
3-10	Variation of λ_M	65
3-11	Direct shear model for two-way slab	66
3-12	Direct shear resistance curve for two-way slab	67
3-13	Deformed shape for direct shear response	68
3-14	Slab in shear failure mode.....	69
3-15	Resistance curve for slab with shear failure mode.....	71
3-16	Program flowchart	72
4-1	Post test view of FH1	75
4-2	FH1 flexural displacement time history.....	75
4-3	FH1 flexural resistance function.....	76
4-4	FH1 direct shear displacement time history.....	76
4-5	FH1 direct shear resistance function.....	77
4-6	Post test view of FH2.....	78
4-7	FH2 flexural displacement time history.....	79
4-8	FH2 flexural resistance function.....	79
4-9	FH2 direct shear displacement time history.....	80
4-10	FH2 direct shear resistance function.....	80
4-11	Post test view of FH3	82
4-12	FH3 direct shear displacement time history.....	82
4-13	FH3 direct shear resistance function.....	83

4-14	FH3 flexural displacement time history.....	83
4-15	FH3 flexural resistance function.....	84
4-16	Post test view of FH4.....	85
4-17	FH4 flexural displacement time history.....	86
4-18	FH4 flexural resistance function.....	86
4-19	FH4 direct shear displacement time history.....	87
4-20	FH4 direct shear resistance function.....	87
4-21	Post test view of FH5.....	88
4-22	FH5 direct shear displacement time history.....	90
4-23	FH5 direct shear resistance function.....	90
4-24	FH5 flexural displacement time history.....	91
4-25	FH5 displacement time history	91
4-26	FH5 resistance function	92
4-27	Post test view of FH6.....	93
4-28	FH6 flexural displacement time history.....	94
4-29	FH6 flexural resistance function.....	94
4-30	FH6 direct shear displacement time history.....	95
4-31	FH6 direct shear resistance function.....	95
4-32	FH1 Pressure-Impulse diagram.....	97
4-33	FH2 Pressure-Impulse diagram.....	97
4-34	FH3 Pressure-Impulse diagram.....	98
4-35	FH4 Pressure-Impulse diagram.....	98
4-36	FH5 Pressure-Impulse diagram.....	99
4-37	FH6 Pressure-Impulse diagram.....	99
A-1	Experiment test configuration for FH3	104

A-2	Construction dimensions and details of FH1	105
A-3	Construction dimensions and details of FH5	105

LIST OF SYMBOLS

A_c	Concrete cross-sectional area
A_{sb}	Area of reinforcement
c	Neutral axis depth at Section 1
c'	Neutral axis depth at Section 2
C'_c	Concrete compressive force at Section 1
C_c	Concrete compressive force at Section 2
C'_s	Steel compressive force at Section 1
C_s	Steel compressive force at Section 2
C_a	Soil arching ratio
C	Damping
E	Elastic modulus
E_c	Concrete elastic modulus
f'_c	Concrete cylinder strength
f'_s	Tensile strength of the reinforcement
f_y	Yield strength of steel reinforcement
F_e	Equivalent force
$F(x,t)$	Arbitrary distributed force
H	Depth of burial
h	Thickness of slab
I	Moment of inertia
I	Impulse
K	Spring stiffness
K_e	Equivalent stiffness
K_e	Elastic stiffness of direct shear degree-of-freedom

K_u	Negative stiffness at segment CD of Hawkins model
K_M	Mass factor
K_L	Load factor
K_o	Coefficient of static lateral earth pressure
K_r	Generalized (modal) stiffness for the r^{th} mode
L	Length of structure
L_x	Long span of slab
L_y	Long span of slab
m	Unit mass
m_u'	Resisting moment at Section 1
m_u	Resisting moment at Section 2
M	Lumped mass
M_e	Equivalent mass
M_r	Generalized (modal) mass
N	External thrust
n_u	Membrane force
$p(t)$	Pressure function
P_B	Average pressure acting on structure
P_S	Uniform pressure acting on soil surface
P_0	Peak load
P_o	Atmospheric pressure
P_r	Generalized (modal) force of the r^{th} mode
P_{so}	Peak pressure
q	Displacement of the selected representative point
\dot{q}	Velocity of the selected representative point

\ddot{q}	Acceleration of the selected representative point
R	Dynamic resistance function
R_1	Residual function 1
R_2	Residual function 2
S	Surround stiffness
t_a	Time of arrival
t_o	Positive phase duration
t_o^-	Negative phase duration
t	Strip outward lateral movement
t	Time
t_d	Loading function time duration
T'	Steel tensile force at Section 1
T	Steel tensile force at Section 2
T_x	Yield force of reinforcement per unit width in the x-direction
T_y	Yield force of reinforcement per unit width in the y-direction
T	Kinetic energy
T_n	Natural period
V	Shear force
V	Potential energy
w	Beam displacement
w	Uniform load per unit area
W	Width of structure
x_i	Displacement
\dot{x}_i	Velocity
\ddot{x}_i	Acceleration

x_{\max}	Maximum displacement
β	Newmark-Beta integration constant
β_1	Ratio of depth of the equivalent ACI stress block to neutral-axis depth
ε	Axial strain
ε_{si}	Steel strain
ε_{ci}	Concrete strain
ε_{cu}	Concrete ultimate strain at failure
θ	Virtual rotation
δ	Slab central displacement
ϕ	Angle of internal friction
$\phi(x)$	Shape function
$\phi_r(x)$	Normal vibration modes for the beam
λ_L	Ratio of load factors
λ_M	Ratio of mass factors
ρ_{vt}	Ratio of total reinforcement area to the area of plane that it crosses
δq_r	Virtual displacement
Δt	Time step interval
Δ_{\max}	Maximum shear slip
τ_e	Direct shear resistance (elastic)
τ_L	Limiting direct shear capacity
τ_m	Maximum direct shear resistance
ω'	Natural circular frequency
ξ	Damping ratio

Abstract of Thesis Presented to the Graduate School
of the University of Florida in Partial Fulfillment of the
Requirements for the Degree of Master of Science

ANALYSIS OF SHALLOW BURIED REINFORCED CONCRETE BOX STRUCTURES
SUBJECTED TO AIRBLAST LOADS

By

Kay Hyang Chee

May 2008

Chair: Theodor Krauthammer
Major: Civil Engineering

A numerical method for the dynamic analysis of shallow-buried reinforced concrete box-type structures subjected to air blast loadings is presented in this study. The proposed method was based on the Single-Degree-of-Freedom (SDOF) approach, where two loosely coupled SDOF systems were considered to take into account the flexural and direct shear mode of structural response. The effects of compression and tension membrane in reinforced concrete slabs and soil-structural interaction were considered in the study. The resistance functions for the structure for each structural response mode were generated and used in the dynamic analysis.

The issue of soil-structure interaction and relationship with structural behavior, in terms of soil arching effect was examined in more detail. A rational model was proposed to incorporate the soil arching effect and a varying SDOF equivalent load and mass factors in the dynamic analysis.

The algorithm was implemented in a computer program. Results of the study were validated using available experimental data from a number of buried reinforced concrete boxes that were tested by other investigators.

CHAPTER 1 INTRODUCTION

1.1 Problem Statement

Recognizing the potential of soil as a protective medium long ago, man has built underground and buried structures to provide shelter and refuge from his potential enemy. By doing so, the soil's performance in the provision of protection to the structure is harnessed through its inertia effects and its ability to diffuse load and dissipate energy. Commonly, reinforced concrete is used as the construction material in protective engineering applications due to its suitable properties and economical value. In addition, most underground or buried structures can usually be approximated as box-type structures. Therefore, in protective engineering applications, the design and evaluation of the performance of a buried reinforced concrete box structures under transient severe loading is an important consideration.

Since the behavior of buried reinforced concrete box structure under the effects of intense pressure pulses applied to the soil surface is of interest, the structural element located closest to the applied load will strongly affect the performance of the entire structure. Therefore, the behavior of a buried structure can be adequately represented by the response of the roof slab which form part of the rectangular box structure.

The design of structural elements under transient loading requires dynamic analysis to be carried out to determine the response characteristics, such as the displacement time history and reaction forces. Analytical studies have been performed previously by various researchers using finite element codes or single-degree-of-freedom (SDOF) models. The SDOF approach is comparatively a simple tool, but with an accurate prediction of the structural behavior, it is a useful tool in preliminary design or parametric studies and can be combined with more advanced analytical techniques to reduce the total computational time and cost.

1.2 Objectives and Scope

This study aims to develop a reliable, simple and accurate analytical approach and numerical procedure to perform dynamic analysis for the design and evaluation of buried reinforced concrete box structure against airblast loads. The procedure will consider non-linear resistance mechanisms for reinforced concrete slab structure in the flexural and direct shear mode of behavior.

The scope of this study is limited to reinforced concrete slabs subjected to transient uniformly distributed airblast pressure load on the soil surface. This study includes modification of the resistance function to consider in-plane compressive force due to internal membrane effect and external thrust due to wave propagation through the soil. The SDOF equivalent load and mass factors are also varied with respect to the slab response regime. This study also includes the evaluation of the dynamic soil arching effect and its corresponding effect on the SDOF load and mass factors. The proposed procedure is to be validated with available experimental test data in order to evaluate its accuracy.

1.3 Research Significance

This study can offer a methodology for a reliable, simple and accurate dynamic analysis engine to study the behavior of a shallow-buried reinforced concrete box structure. The approach includes rational and physics-based resistance functions, taking into account the effect of soil structural interaction (e.g. wave propagation and soil arching effect) and improves on the approach to approximate the real continuous system into an equivalent SDOF system in order to provide an accurate numerical result.

CHAPTER 2 BACKGROUND AND LITERATURE REVIEW

2.1 Introduction

Since humans recognized the potential of soil as a protective medium, underground structure have been constructed to provide shelter and refuge from their enemy. In order to design an underground structure or to evaluate its structural performance, the first requirement is to characterize the expected performance under the specified design loads. With the necessary loading applied, the relevant mode of structural behavior has to be modeled accurately and the response results from dynamic analysis can be used for design purpose. If the main design concern is a specific response limit state (rotation, failure, etc.), a suitable computational aid to use is a Pressure-Impulse diagram.

In this study, the form of loading considered is from blast and the corresponding response of reinforced concrete box structures roof slabs. A brief introduction to blast loads and its effects on buried structures are presented in Sections 2.2 and 2.3. Blast loadings are transient and the response is highly dependent on the peak load and duration. The dynamic structural behavior and analysis are reviewed in Section 2.4. Section 2.5 focuses on the different structural response mode for reinforced concrete slabs and their corresponding resistance model under static and dynamic loading. Lastly, the background of pressure-impulse diagrams and their applications are presented in Section 2.6.

2.2 Blast Loads

Generally, the most common sources of explosions and blast loads are derived from either chemical (High Explosive, HE) or nuclear materials. The environment created by an explosion consists of the following effects:

- Airblast
- Groundshock

- Ejecta
- Fragments
- Fire, thermal and chemical (nuclear explosions only)
- Radiation (nuclear explosions only)
- Electromagnetic pulse (EMP) (nuclear explosions only)

2.2.1 Airblast from High Explosive

In an open air High Explosive (HE) explosion, the reaction generates gases at very high pressure and temperature, causing a violent expansion of these explosive gases and the surrounding air is forced out of the volume it occupies. The shock front is essentially vertical, reflecting the sudden rise in pressure due to the explosion. It is a layer of compressed air, forms in front of the explosive gases. As the gases expand and cool, their pressure decreases. The pressure of the blast wave front also falls with increasing distance from source. Eventually, the pressure falls a little below atmospheric pressure because the momentum of the moving gas molecules. The gases are over-expanded near the explosion location and a reversal of flow towards the source occurs. This is the negative phase which is characterized by a pressure lower than the ambient air pressure. Eventually, the pressure and temperature of the gases returns to equilibrium (Smith and Hetherington 1994, Tedesco et al. 1998, Krauthammer 2008).

An idealized pressure-time function for an airblast shockwave in free air is shown in Figure 2-1, where P_0 is the atmospheric pressure; P_{s0} is the peak pressure; t_a is the time of arrival; t_0 is the positive phase duration and t_0^- is the negative phase duration.

The impulse of the blast wave is defined as the area under the pressure time curve and can be calculated simply by

$$I = \int_{t_a}^{t_a+t} p(t) dt \quad (2-1)$$

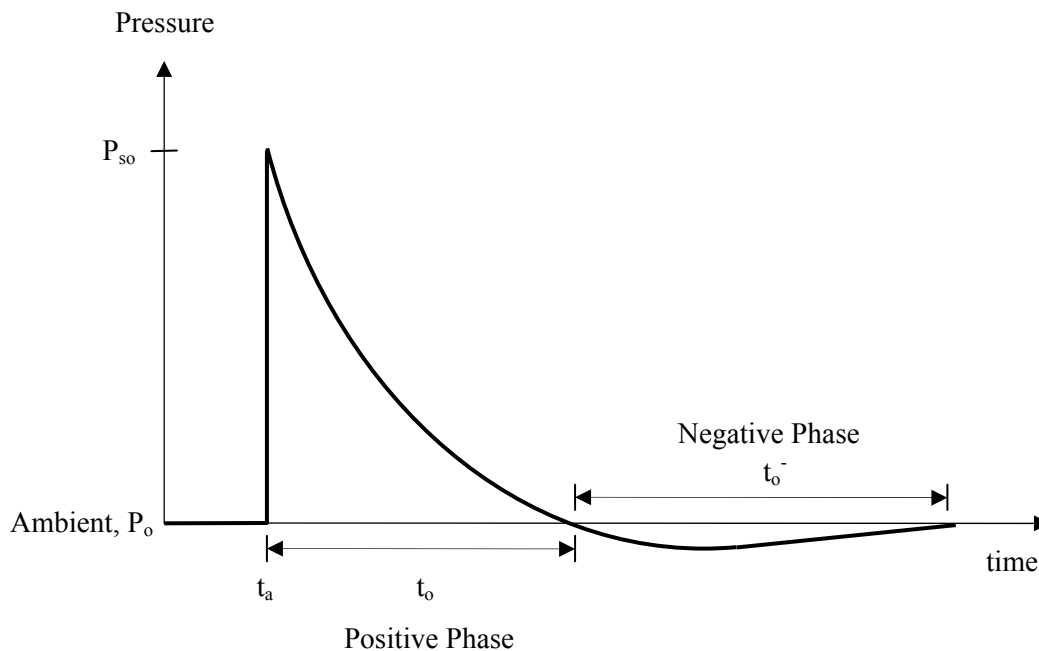


Figure 2-1. Blast pressure-time curve.

2.2.2 Nuclear Devices

A nuclear device can deliver its explosive effects from air burst, surface burst or shallow burst. When the nuclear device is exploded at an altitude below 100,000 ft, about 50% of the released energy will result in blast and shock (ASCE 1985). For high altitude bursts above 100,000 ft, they generate only strong EMP effects (which should be considered in facility design) but are of little interest to the structural engineer.

The characteristics of the blast pressure wave in a nuclear explosion are similar to those of a high explosive (HE) explosion and are a function of the weapon yield, the height of burst and the distance from the burst. There is also dynamic pressure which results from the mass flow behind the shock front. The dynamic pressure is a function of the gas density and the flow velocity. As with the HE explosion, there is both a positive and negative phase for the over-pressure and for the dynamic pressure (Krauthammer 2008).

2.3 Effects on Buried Structures

Although buried structures offered protection from aerially delivered weapons and airborne blast effects, but these structures can be vulnerable to the transient stresses propagated through the soil and rock in which they have been constructed (Smith and Hetherington 1994). Other types of loadings such as buried charges or structural penetration are also important but they are not considered in this study.

A shock wave will be induced in the soil when an air blast is applied to the free soil surface (soil-air interface). The shock wave travels downwards in the vertical direction until meeting with the structure. Based on data from soil stress gages and interface pressure gages in nuclear tests, the shock front can be considered as quite planar (Krauthammer et al. 1986). The possible modulation in the interface pressures will appear as a result of wave reflections and soil-structure interaction effects, including soil-arching. The resultant pressure time history may not be uniformly distributed over the roof slab of the buried structure.

2.3.1 Soil Arching Effect

Loads acting on the buried structure are influenced by the interaction between the structure and the surrounding soil. An effect of such interaction is soil arching and it is defined as the ability of a soil to transfer loads through a system of shear stresses from one location to another in response to a relative displacement between the locations. A stiffer structure in the soil tends to attract more loads, while stress will be diverted from or around buried structures that are less stiff (Kiger 1988).

Soil arching occurs when there is a relative motion between structure and soil. The classical approach for computing soil arching is by the use of the “trapdoor” mechanism (see Figure 2-2), as discussed in Terzaghi and Peck (1948). There are two types of soil arching, namely:

- Passive arching: The structure moves away from the loading soil, and the soil cannot follow it due to shear resistance.
- Active arching: The structure is pushed into the soil.

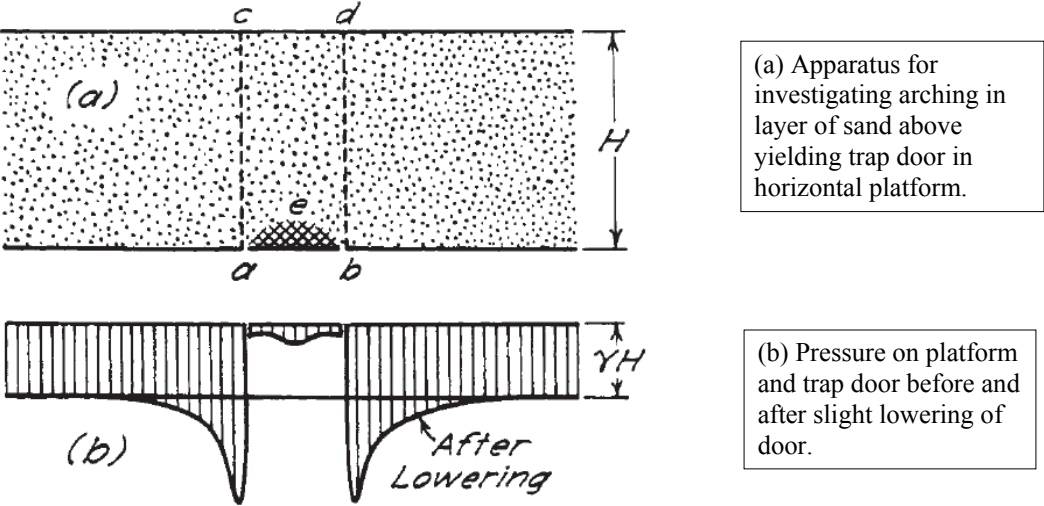


Figure 2-2. Soil arching demonstrated by trap door experiment (Terzaghi and Peck 1948).

The soil arching ratio C_a is defined as the ratio of the average pressure on the unsupported clear span of the structure to the applied surface structure. For a shallow burial depth, the arching ratio is given by Equation 2-2 (ASCE 1985 and Kiger 1988):

$$C_a = \frac{P_B}{P_S} = \exp\left[\frac{-2K_o \cdot \tan(\phi) \cdot (W + L)H}{W \cdot L}\right] \tag{2-2}$$

where P_B is the average pressure acting on structure; P_S is the uniform pressure acting on soil surface; K_o is the coefficient of static lateral earth pressure; ϕ is the angle of internal friction in the soil and W, L, H are the width, length and depth of burial of the structure respectively.

Typical arching factors for rectangular and arch structures are shown in Figure 2-3.

Besides reducing the average pressure acting on the buried structure, the actual pressure distribution is also no longer uniform due to soil arching. With a responding roof slab, the

pressure at the center will be smaller while towards the edge the pressure is much higher. A parabolic pressure distribution can be assumed (Kiger 1988).

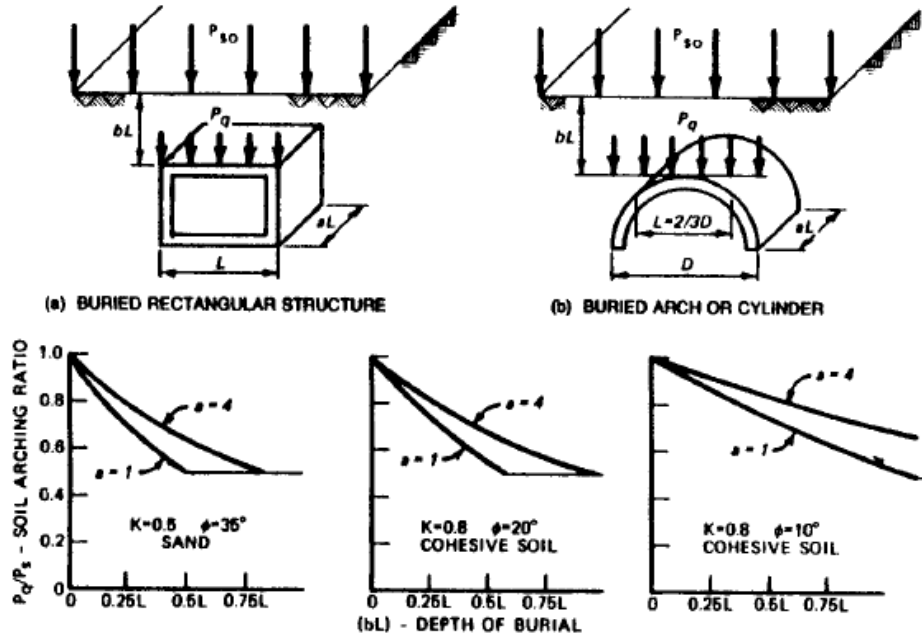


Figure 2-3. Soil arching as function of depth of burial (ASCE 1985).

2.4 Dynamic Structural Behavior and Analysis

Structural behavior under time dependent loading can be obtained by dynamic analysis.

The dynamic equilibrium of a system can be described by the equation of motion. An important result from the equation is the displacement time history of the structure subjected to a time-varying load (Tedesco et al. 1998).

All structures are in reality distributed mass and stiffness systems and are referred to as distributed systems, or continuous systems. Each system consists of an infinite number of degrees of freedom and can be considered as a discrete small element connected by springs to all other elements. The governing equations for continuous system can be expressed in partial differential equations and analytical or closed-form solutions can be obtained only for relatively simple continuous systems with well-defined boundary conditions.

Using an example of a uniform beam subjected to an arbitrary distributed force $F(x,t)$ as shown in Fig 2-4, the equation of motion for the system is given by

$$EI \frac{\partial^4 w}{\partial x^4} + m \frac{\partial^2 w}{\partial t^2} = F(x,t) \quad (2-3)$$

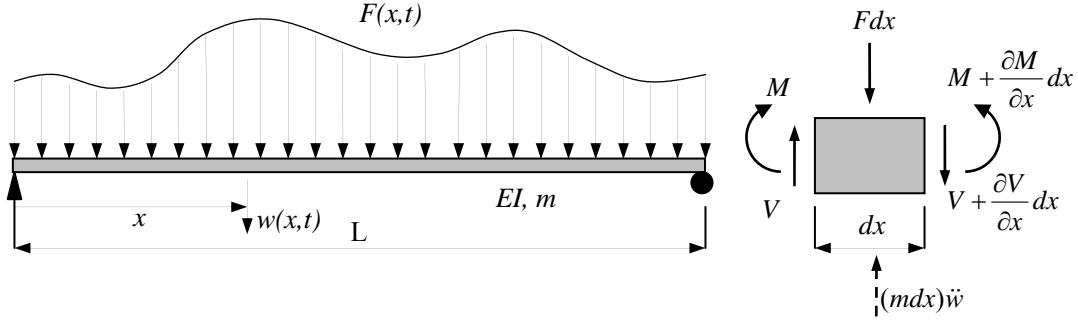


Figure 2-4. Uniform beam subject to arbitrary load.

The normal vibration modes for the beam $\phi_r(x)$ must satisfy the boundary conditions and

$$EI \frac{\partial^4 \phi_r(x)}{\partial x^4} - m\omega_r^2 \phi_r(x) = 0 \quad (2-4)$$

where $\phi_r(x)$ represents the normal vibration mode shape for the r^{th} mode.

The normal modes are orthogonal functions that must satisfy the mass orthogonality relationship

$$\int_0^L m \phi_r(x) \phi_s(x) dx = \begin{cases} 0 & \text{for } r \neq s \\ M_r & \text{for } r = s \end{cases} \quad (2-5)$$

where the generalized (modal) mass is given by

$$M_r = \int_0^L m \phi_r^2(x) dx \quad (2-6)$$

The general solution in terms of the normal modes $\phi_r(x)$ and normal coordinates $q_r(t)$,

$$w(x,t) = \sum_{r=1}^{\infty} \phi_r(x) q_r(t) \quad (2-7)$$

Establishing the kinetic and potential energy gives

$$T = \frac{1}{2} \int_0^L m \dot{w}^2(x,t) dx = \frac{1}{2} \sum_{r=1}^{\infty} M_r \dot{q}_r^2 \quad (2-8)$$

$$V = \int_0^L EI \left[\frac{\partial^2 w(x,t)}{\partial x^2} \right]^2 dx = \sum_{r=1}^{\infty} K_r q_r^2 \quad (2-9)$$

where K_r is the generalized (modal) stiffness for the r^{th} mode.

Finally, the generalized (modal) force of the r^{th} mode P_r must be determined from the work done by the applied force $F(x,t)$ acting through the virtual displacement δq_r . Therefore

$$\delta W = \int_0^L F(x,t) \left[\sum_{r=1}^{\infty} \phi_r(x) \delta q_r \right] dx = \sum_{r=1}^{\infty} \delta q_r \int_0^L F(x,t) \phi_r(x) dx \quad (2-10)$$

and
$$P_r = \int_0^L F(x,t) \phi_r(x) dx \quad (2-11)$$

Substituting the above expressions for T , V and P_r into the Lagrange's equations

$$\frac{d}{dt} \left(\frac{\partial T}{\partial \dot{q}_r} \right) - \frac{\partial T}{\partial q_r} + \frac{\partial V}{\partial q_r} = P_r \quad (2-12)$$

the equation of motion in normal coordinates is

$$M_r \ddot{q}_r + K_r q_r = P_r \quad (2-13)$$

Equation 2-13 represents the uncoupled equations of motion for $r = 1, 2, 3, \dots, \infty$.

For approximation to the continuous system of a real structure, only a few of the lower modes have responses of any significance for practical purposes, and in some cases only the fundamental mode is of importance. Depending on the chosen approximation, the real system can be considered as either a multi-degree-of-freedom (MDOF) system or a single-degree-of-freedom (SDOF) system.

2.4.1 Single-Degree-of-Freedom (SDOF) System

As mentioned in the previous section, in reality all structural system consists of an infinite number of degrees of freedom. An infinite number of independent spatial coordinates are necessary to completely define the geometric location of all the masses and stiffness of a structure (Tedesco et al. 1998). However, it is frequently possible to approximate the real system to a single degree of freedom having equivalent parameters of load, mass and stiffness where the fundamental mode of response is significant. It is advantageous to model the structure as a Single-Degree-of-Freedom (SDOF) as this approximate method permit rapid analysis of complex structures with reasonable accuracy (Biggs 1964). SDOF formulation gives designer valuable information on the dynamic characteristics of the system and they are usually used in preparation of detailed analysis using more advanced methods (Krauthammer 1998).

The equivalent system is selected so that the deflection of the concentrated mass is the same as that for some significant representative point on the structure, e.g. midspan of beam or center of slab. Since the time scale is not altered, the response of the equivalent system, defined in terms of displacement and time, will be exactly the same as the chosen representative point. As presented in the previous section, the equation of motion for a structure system (Equation 2-13) can be simplified for the SDOF system (inclusive of damping) as

$$M_e \ddot{q} + C \dot{q} + K_e q = F_e \quad (2-14)$$

where M_e , C , K_e and F_e are the equivalent mass, damping, stiffness and force; q, \dot{q}, \ddot{q} is the displacement, velocity and acceleration value of the selected representative point.

The constants of the equivalent system are evaluated on the basis of an assumed shape function for the deflected structure. When the total load, mass, resistance and stiffness of the

real structure are multiplied by the corresponding “transformation factors”, we obtain the parameters for the equivalent single-degree-of-freedom system.

2.4.2 Transformation Factors for Equivalent SDOF

To convert an actual continuous structure into an equivalent single-degree-of-freedom system, the equivalent parameters of the system like the equivalent mass and equivalent loading and resistance function have to be evaluated. Biggs (1964) used transformation factors, denoted by K , to convert the real system into the equivalent system.

The equivalent mass of a SDOF system for a structure with continuous mass can be determined by Equation 2-15 and the mass factor, K_M , is defined as the ratio of the equivalent mass to the actual total mass of the structure (Biggs 1964).

$$M_e = \int_L m \phi^2(x) dx \quad (2-15)$$

$$K_M = \frac{M_e}{M_t} = \frac{\int_L m \phi^2(x) dx}{M_t} \quad (2-16)$$

The equivalent force on the SDOF system for distributed loads can be found by Equation 2-17 and the load factor, K_L , is defined as the ratio of the equivalent to actual total force

$$F_e = \int_L p(x) \phi(x) dx \quad (2-17)$$

$$K_L = \frac{F_e}{F_t} = \frac{\int_L p(x) \phi(x) dx}{F_t} \quad (2-18)$$

where m is the unit mass, $p(x)$ is the distributed loading acting on structure and $\phi(x)$ is the assumed shape function on which the equivalent system is based.

Biggs (1964) had tabulated transformation factors for beams and slabs with various types of support conditions. For a fixed end beam or one-way slab, the load factor varies from 0.50 for

the plastic case to 0.64 for the elastic-plastic case and 0.53 for the elastic case. For the mass factor, it varies from 0.33 for plastic case to 0.50 for the elastic-plastic case and 0.41 for the elastic case.

2.4.3 Numerical Integration (Newmark-Beta method)

The analytical, or closed-form, solution of the equation of motion can be cumbersome even for relatively simple excitations. Therefore, for most practical problems, numerical evaluation technique is employed to obtain the dynamic response (Tedesco et al. 1998).

In this study, the Newmark-Beta method is used in the direct integration of the equation of motion and is briefly summarized below (Newmark and Rosenblueth 1971):

- A. For an equivalent SDOF system, the equation of motion is as follows:

$$m\ddot{x} + c\dot{x} + kx = F(t) \quad (2-19)$$

- B. Let the values of x_i , \dot{x}_i and \ddot{x}_i be known at time $t = t_i$. Let $t_{i+1} = t_i + \Delta t$, where Δt is the time step interval. Assume a value of \ddot{x}_{i+1} .

- C. Compute the value $\dot{x}_{i+1} = \dot{x}_i + (\ddot{x}_i + \ddot{x}_{i+1}) \frac{\Delta t}{2}$ (2-20)

- D. Compute the value $x_{i+1} = x_i + \dot{x}_i \Delta t + \left(\frac{1}{2} - \beta\right) \ddot{x}_i (\Delta t)^2 + \beta \ddot{x}_{i+1} (\Delta t)^2$ (2-21)

- E. Compute a new approximation to \ddot{x}_{i+1} using equation of motion (Equation 2-19)

- F. Repeat steps B to D beginning with the newly computed \ddot{x}_{i+1} , until a satisfactory degree of convergence is attained.

- G. Step B is consistent with a straight line approximation to \ddot{x} in the interval considered. If $\beta = 1/4$, the method is consistent with a straight line variation of \dot{x} in the same interval (constant average acceleration). If $\beta = 1/6$, method corresponds to a parabolic variation. In this study, it was set as $\beta = 1/6$.

- H. The numerical method starts at $t=0$, the time instant when the load is applied. The initial condition is that the mass is at rest. $\ddot{x}_0 = \frac{F(t=0)}{m}$, $x_0 = \dot{x}_0 = 0$.

This numerical integration method is unconditionally stable. However, a proper value of the time step interval must be chosen to ensure sufficient accuracy. The time step is dependent on the natural period of the system (T_n) and the loading function time duration (t_d). According to Bathe (1996) and Clough and Penzien (1993), the chosen time step is given by

$$\Delta t \leq \text{Min}\left(\frac{T_n}{10}, \frac{t_d}{12}\right) \quad (2-22)$$

2.5 Behavior of Reinforced Concrete Slabs

A reinforced concrete box effectively is made up a number of reinforced concrete slabs. Therefore, it is essential to first understand the load resisting mechanism of reinforced concrete slabs. This section discusses the two possible failure mechanisms, namely the flexural and direct shear mode, and their respective resistance-displacement functions.

Sections 2.5.1 and 2.5.2 discuss the structural behavior of reinforced concrete slabs in flexure using yield line theory and consideration of actual membrane actions respectively. Sections 2.5.3 and 2.5.4 focus on the compressive membrane and tensile membrane behavior. Section 2.5.5 presents a rational flexural model for slabs which was proposed by Krauthammer et al. (1986). Section 2.5.6 discusses the direct shear mode of failure for slabs and the Hawkins model for direct shear failure is presented in Section 2.5.7. Lastly, the dynamic resistance functions and response is covered in Section 2.5.8.

2.5.1 Flexural Behavior: Johansen's Yield Line Theory

The Johansen's yield line theory is a method for the limit analysis of reinforced concrete slabs. The ultimate load of the slab is calculated by postulating a collapse mechanism that is compatible with the boundary conditions (Park and Gamble 2000). The moments at the plastic hinge lines are the ultimate moments of resistance of the sections, and the ultimate load is determined using the principle of virtual work or equations of equilibrium.

A yield line refers to a line in the plane of the slab about which plastic rotation occurs and across which the reinforcing bars are yielding. When a slab is progressively loaded to failure, yielding of the tension steel occurs at section of maximum moment with a large change in section curvature while the moment remains almost constant at the ultimate moment of resistance. As the load is increased, the yield line propagates from the point at which yielding originated until eventually the yield lines have formed in sufficient numbers to divide the slab into segments that can form a collapse mechanism. The positions of the yield lines developed are governed by the arrangement of reinforcement, boundary conditions and loading (Park and Gamble 2000). The development of the yield line pattern for a uniformly loaded simply supported rectangular slab is shown in Figure 2-5.

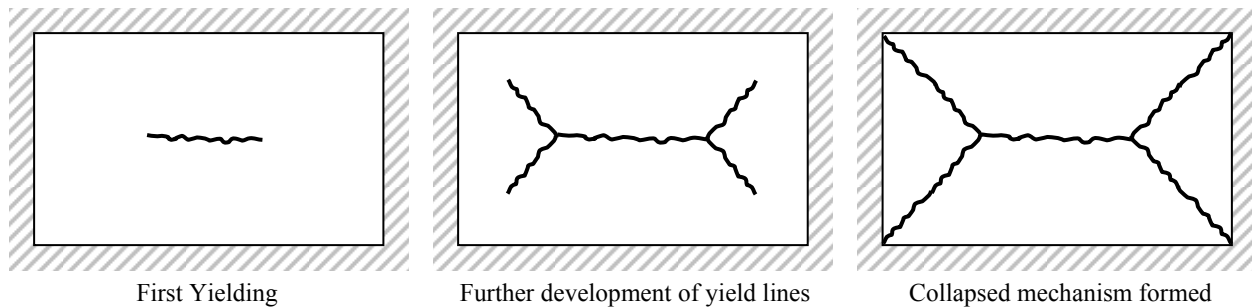


Figure 2-5. Yield lines development in a uniformly loaded simply supported slab (Park and Gamble 2000).

2.5.2 Flexural Behavior: Membrane Action

The resistance of reinforced concrete slabs computed using the traditional approach (e.g. ACI 2005) of one-way or two-way slabs formulation will be adequate for normal design applications, but they are not accurate representations of the actual capacity of the slabs. Often under the extreme loading conditions in the blast and shock environment, compressive and tensile membrane actions in slabs can enhance the ultimate structural capacity of the slab. Typical design serviceability requirements like deflections and cracking need not be enforced in

some field of applications such as protective design, since moderate to severe degree of damage may be acceptable under such extreme loading.

Figure 2-6 shows the typical load-central deflection curve of a uniformly loaded two-way rectangular slab with laterally restrained edges (Park and Gamble 2000). When the applied load is increased from point A to B, although the initial resistance is developed by conventional two-way slab mechanism, a compression membrane mechanism sets in with the corresponding increase in the central deflection due to the restraint of the outward movement of the slab edges. The induced compressive membrane force in the slabs results in an enhancement of the flexural strength. Tests have demonstrated that the ultimate load may be significantly (about two to eight times) higher than that given by the Johansen's yield line theory (Section 2.5.1), particularly if the boundary restraint is stiff, high span-depth ratio and small reinforcement steel ratio (Park and Gamble 2000).

With continued loading and increase of the deflection beyond point B, the load carried by the slab decreases rapidly because of a reduction in the compressive membrane force. As point C is approached, the membrane forces in the central region of the slab change from compressive to tensile.

Beyond point C, with an increased loading, the effect of restrained edges sets in and allows the slab reinforcement to act as a plastic tensile membrane with full-depth cracking of the concrete over the central region of the slab due to the large stretch of the slab surface. The slab continues to carry further load with an increase in deflection until point D when the reinforcement fractures. Tests have indicated that for heavily reinforced slabs the load at point D can exceed the ultimate load at point B. Therefore, in many cases tensile membrane action also provides a useful means of preventing catastrophic failure at ultimate conditions.

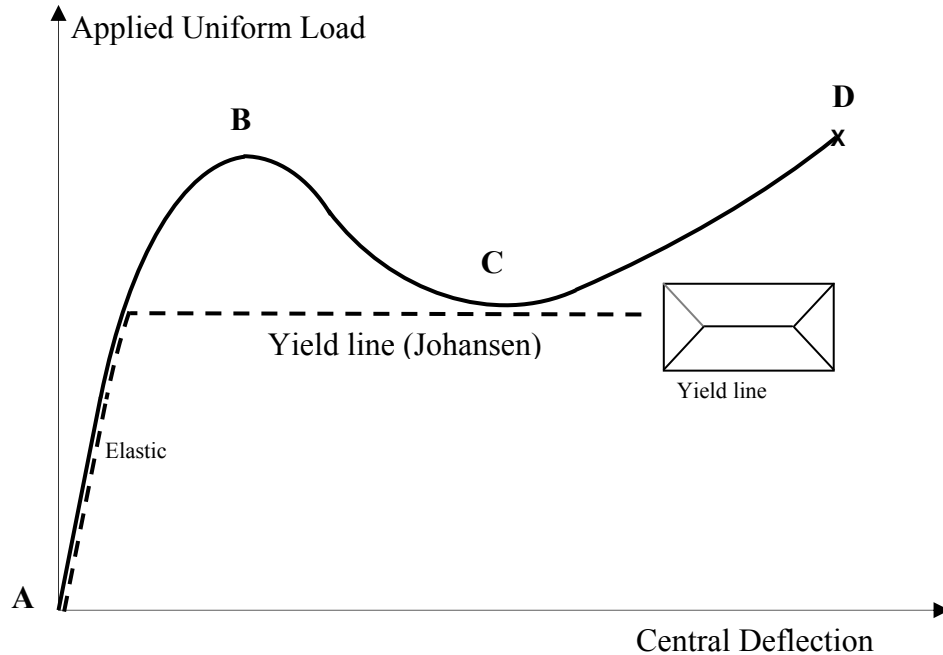


Figure 2-6. Load-deflection curve for two-way RC slab with laterally restrained edges.

2.5.3 Slab Compressive Membrane

The compressive membrane behavior of slabs covers two ranges of deflections, point A to B and point B to C (as shown in Figure 2-7). As the load is increased from A to B, the slab behavior is initially elastic, combined with inelastic behavior at critical sections at higher loads. Yield line pattern for the slab is fully developed at point B. As deflection increases from B to C, the deformation is mainly caused by plastic rotation at the yield lines. Therefore, the slab is deforming as a mechanism in the range BC. Plastic theory can be developed first for a restrained strip and then extended to a two-way slab.

For a two-way slab, it can be assumed to be composed of strips running in the x- and y-directions. The strips have the same thickness as the slab. The x-direction strips contain only x-direction steel and the y-direction strips contain only y-direction steel.

The yield line pattern of the slab is as shown in Figure 2-7. Then yield sections of the strips lie on the yield lines and have the same deflection as the actual slab. The corner yield lines

are simplified to be at 45° to the edges (Park and Gamble 2000). This simplification of assuming corner lines at 45° results in not more than 3% error in theoretical ultimate load for slabs with all edges fixed against restraint (Park and Gamble 2000).

Each of these strips can be analyzed using the plastic theory presented in Park and Gamble (2000). A fixed-end strip with plastic hinges developed is shown in Figure 2-8. This strip is initially of length L and is fully restrained against rotation and vertical translation at the ends. The ends of the strip are considered to be partially restrained against lateral displacement, and the outward lateral movement at the other end is t .

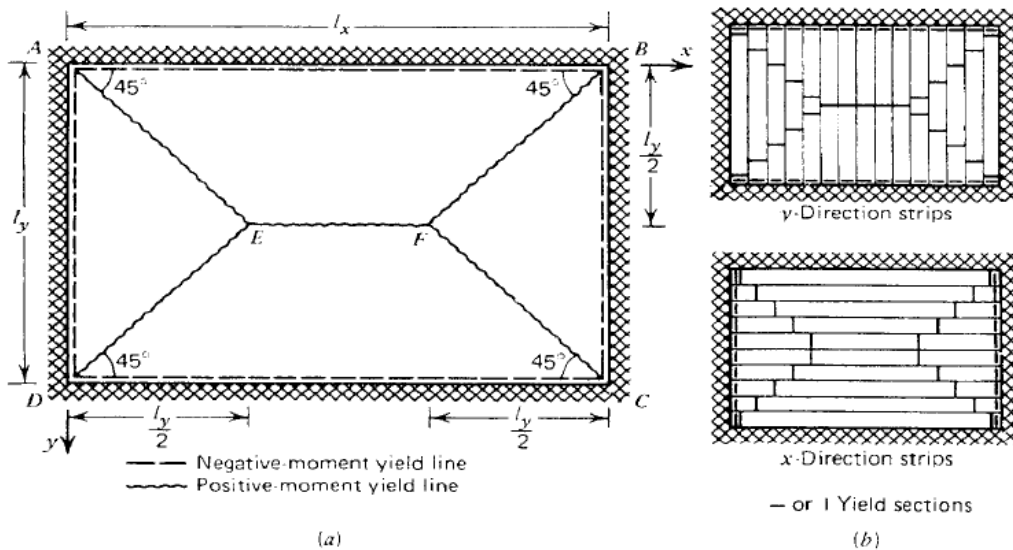


Figure 2-7. Assumed yield line pattern for uniformly loaded slab with restrained edges (Park and Gamble 2000). A) Actual slab. B) Systems of strips.

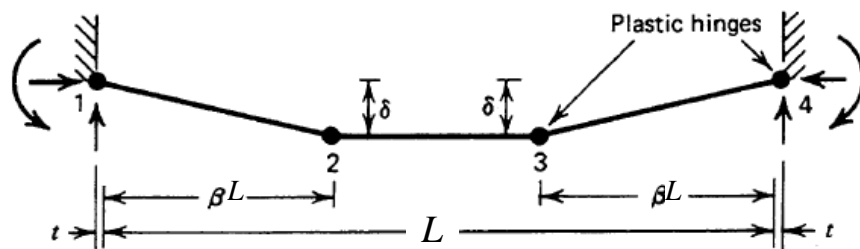


Figure 2-8. Plastic hinges of a restrained strip (Park and Gamble, 2000).

Compressive membrane action is dependent on the restriction of small lateral displacement, and the behavior of the strip is sensitive to any lateral displacements that may occur. The lateral displacement t may be calculated from the movement of the boundary system under the action of the membrane force (Park and Gamble 2000).

The strip shown in Figure 2-8 is considered to have symmetrically positioned plastic hinges. The symmetry assumption leads to the necessary assumptions that the top steel at opposite ends must be equal and the bottom steel is constant along the length. The top and bottom steel may be different. It is assumed that at each plastic hinge that the tension steel has yielded and the concrete has reached its compressive strength

The portions of the strip between the plastic hinges are assumed to remain straight. The sum of the elastic, creep and shrinkage axial strain, ε , will be constant. The change in dimensions of end Section 12 due to ε and t is shown in Figure 2-9.

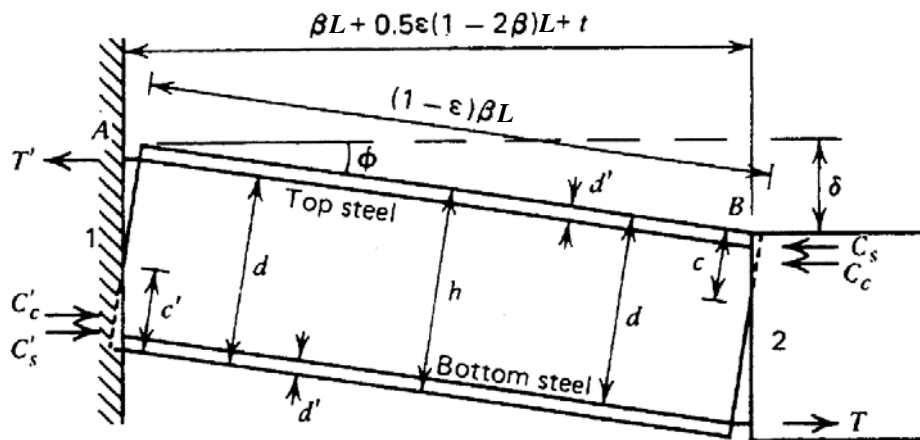


Figure 2-9. Portion of strip between plastic hinges (Park and Gamble 2000).

Based on the geometry of the deformations, the compatibility equation can be written as

$$c' + c = h - \frac{\delta}{2} - \frac{\beta L^2}{2\delta} \left(\varepsilon + \frac{2t}{L} \right) \quad (2-23)$$

where c' and c are the neutral axis depths at yield Sections 1 and 2 respectively, and h is the thickness of the strip.

For equilibrium, the membrane forces acting on Sections 1 and 2 of the strip are equal,

$$C'_c + C'_s - T' = C_c + C_s - T \quad (2-24)$$

where C'_c and C_c are the concrete compressive forces, C'_s and C_s are the steel compressive forces and T' and T are the steel tensile forces, acting on cross-sections 1 and 2 respectively.

The concrete compressive forces can be written for a unit width strip as

$$C'_c = 0.85f'_c\beta_1c' \quad (2-25)$$

$$C_c = 0.85f'_c\beta_1c \quad (2-26)$$

where f'_c is the concrete cylinder strength and β_1 is the ratio of the depth of the equivalent ACI rectangular stress block to the neutral-axis depth (ACI 2005).

Using Equations 2-24, 2-25 and 2-26,

$$c' - c = \frac{T' - T - C'_s + C_s}{0.85f'_c\beta_1} \quad (2-27)$$

Solving simultaneously Equations 2-6 and 2-10, the neutral axis depths are given as

$$c' = \frac{h}{2} - \frac{\delta}{4} - \frac{\beta L^2}{2\delta} \left(\varepsilon + \frac{2t}{L} \right) + \frac{T' - T - C'_s + C_s}{1.7f'_c\beta_1} \quad (2-28)$$

$$c = \frac{h}{2} - \frac{\delta}{4} - \frac{\beta L^2}{2\delta} \left(\varepsilon + \frac{2t}{L} \right) - \frac{T' - T - C'_s + C_s}{1.7f'_c\beta_1} \quad (2-29)$$

Figure 2-10 the shows the conditions at a positive-moment yield section of unit width. The stress resultants at the section C_c , C_s and T are statically equivalent to the membrane force n_u , acting at mid depth, and the resisting moment m_u , summed about the mid depth axis. Therefore, for a unit width strip,

$$n_u = C_c + C_s - T = 0.85 f'_c \beta_1 c + C_s - T \quad (2-30)$$

$$m_u = 0.85 f'_c \beta_1 c (0.5h - 0.5\beta_1 c) + C_s (0.5h - d') + T (d - 0.5h) \quad (2-31)$$

where c is given by Equation 2-28. For a negative moment yield section, m_u' is given by an equation similar to Equation 2-31, and for equilibrium $n_u' = n_u$.

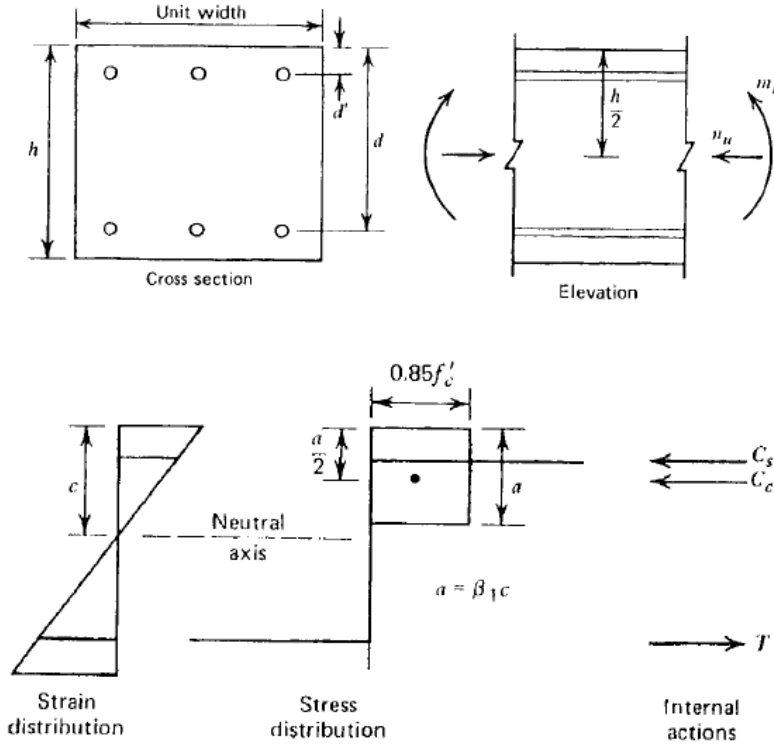


Figure 2-10. Conditions at positive moment yield section (Park and Gamble 2000).

Considering end sections 12 or 34 of the strip, the sum of the moments of the stress resultants at the yield sections about an axis at mid-depth at one end can be written as

$$m_u' + m_u - n_u \delta = 0.85 f'_c \beta_1 h \left[\frac{h}{2} \left(1 - \frac{\beta_1}{2}\right) + \frac{\delta}{4} (\beta_1 - 3) + \frac{\beta L^2}{4\delta} (\beta_1 - 1) \left(\varepsilon + \frac{2t}{L}\right) + \frac{\delta^2}{8h} \left(2 - \frac{\beta_1}{2}\right) \right. \\ \left. + \frac{\beta L^2}{4h} \left(1 - \frac{\beta_1}{2}\right) \left(\varepsilon + \frac{2t}{L}\right) - \frac{\beta_1 \beta^2 L^4}{16h\delta^2} \left(\varepsilon + \frac{2t}{L}\right)^2 \right] \\ - \frac{1}{3.4 f'_c} (T' - T - C'_s + C_s)^2 + (C'_s + C_s) \left(\frac{h}{2} - d' - \frac{\delta}{2}\right) \\ + (T' + T) \left(d - \frac{h}{2} + \frac{\delta}{2}\right) \quad (2-32)$$

If Sections 12 or 34 of the strip is given a virtual rotation θ , the virtual work done at the yield sections is given by

$$(m'_u + m_u - n_u \delta)\theta \quad (2-33)$$

By equating the work done (Equation 2-33) to the work done by the loading on the strip, an equation relating the deflection of the strip to the load carried can then be obtained (Park and Gamble 2000).

2.5.4 Slab Tensile Membrane

Towards the end of the compressive membrane action range, the large stretch of the slab surface causes the cracks at the central region of the slab to penetrate across the whole thickness of the slab depth, and the load is entirely carried by the reinforcing bars acting as a tensile membrane through catenary action. With further deflection (beyond point C in Figure 2-6), the region of tensile membrane action gradually spreads throughout the slab, and the load carried increases until the steel reinforcement starts to fracture at point D. Figure 2-11 shows the forces acting on a uniformly loaded plastic tensile membrane for a rectangular slab.

In Park and Gamble (2000), a linear relationship between load and deflection (Equation 2-34) for a uniformly loaded slab is given as an approximation for the tensile membrane region of point C-D of Figure 2-6.

$$\frac{wL_y^2}{T_y \delta} = \frac{\pi^3}{4 \sum_{n=1,3,5,\dots}^{\infty} \frac{(-1)^{(n-1)/2}}{n^3} \left\{ 1 - 1/\cosh\left(\frac{n\pi L_x}{2L_y} \sqrt{\frac{T_y}{T_x}}\right) \right\}} \quad (2-34)$$

where w is the uniform load per unit area, δ is the central deflection, L_x and L_y are the long and short span of the slab, T_x and T_y are the yield force of the reinforcement per unit width in the x- and y-directions respectively.

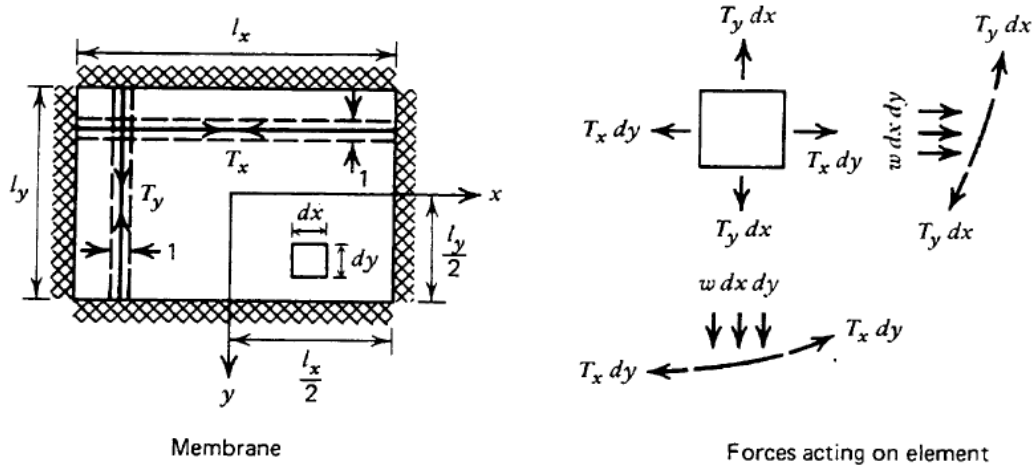


Figure 2-11. Uniformly loaded plastic tensile membrane.

2.5.5 Reinforced Concrete Slab Flexural Model

The plastic theory and its assumptions in the Section 2.5.3 are only applicable at large deflections. Therefore, the initial portion of the load deflection relationship will not be representative at deflections when the slab is still within the elastic or elastic-plastic regime.

Krauthammer (1984) and Krauthammer et al. (1986) proposed a rational model to rectify the shortcoming. A second order polynomial is fitted to segment A-B and a straight line is fitted to segment B-C. To better describe the tensile membrane resistance, a straight line which is not required to pass through the origin is proposed for segment C-D. The proposed model is shown in Figure 2-12.

Park and Gamble (2000) reported that a good estimate of the ultimate load of the slab would be obtained at a central deflection of about half the slab thickness (actually half the effective depth). The flexural model as shown in Figure 2-12 is completed with approximations that the displacements at point B and point C at $0.5h$ and h respectively, where h is the slab thickness. Krauthammer et al (1986) showed that this approach was able to represent accurately based on comparison against experimental test data.

This approach was modified by Frye (2002) to consider the differences for slender, intermediate and deep slabs. For slender slabs, the corresponding central deflections at point B and C are $0.5h$ and $1.0h$. For deep slabs, the corresponding central deflections at point B and C are $0.07h$ and $0.17h$. For intermediate slabs, the displacement and resistance is linearly interpolated between the slender and deep models.

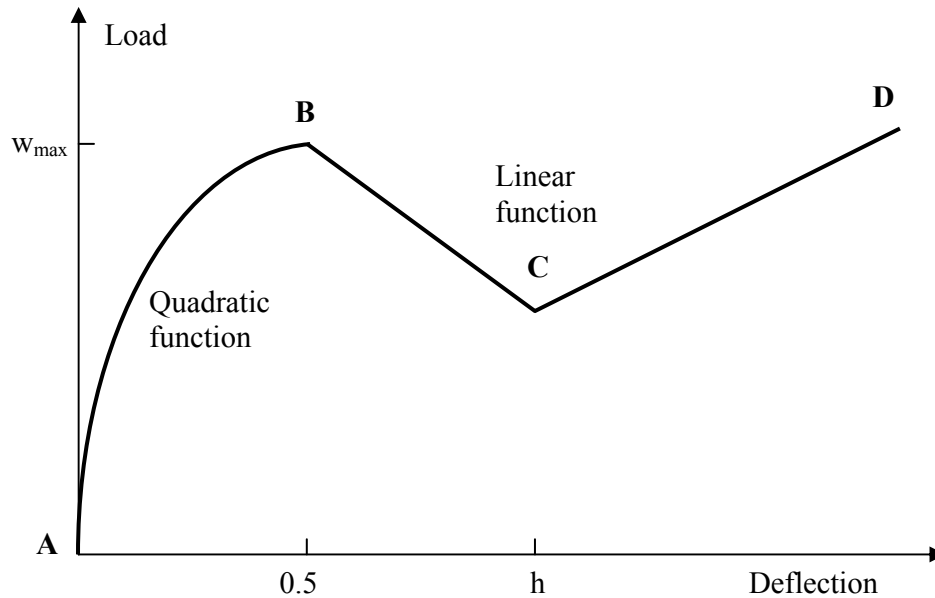


Figure 2-11. Flexural resistance model for slab (Krauthammer 1984).

2.5.6 Direct Shear Behavior

Kiger and Getchell (1980-1982) and Slawson (1984) both reported that reinforced concrete slabs exhibited another type of behavior under severe and rapid loading. Beside failure in flexural mode, some slabs failed in a direct shear mode. A photograph of a test specimen which failed in a direct shear is shown in Figure 2-13.

This type of shear failure is characterized by slipping and large displacement along the vertical interface shear plane (Krauthammer et al. 1986). The shear failure produced a vertical failure plane at the edge of roof and both the top and bottom steel exhibited necking and were severed nearly flush with the failure plane (Crawford et al. 1983). Direct shear failure will occur

at the very early stage of the loading, usually a fraction of a millisecond, and before any significant dynamic flexural response can be observed. Similarly, once the slab survived the initial loading phase without failure in direct shear mode, it was observed that a flexural mode of failure will dominate which will occur at a much later time.

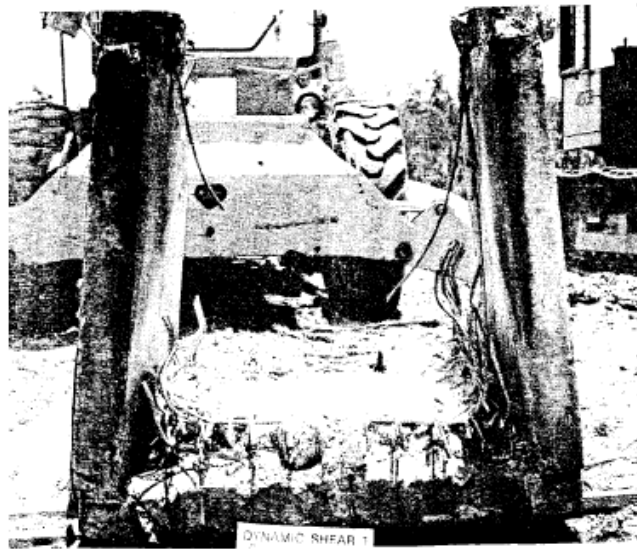


Figure 2-13. Slab in direct shear failure mode (Slawson 1984).

Crawford et al. (1999) consider this direct shear mode of failure as an important element in the blast effects design process. This mode is associated with geometric or load discontinuity, but not with flexure, and is caused by the high shear inertia forces which do not exist under static or slow dynamic loads.

2.5.7 Hawkins Shear Model

The direct shear model used in this study is based on a model proposed by Hawkins (1972). The model describes the static interface shear transfer in RC members with well-anchored main reinforcement in the absence of axial forces. Krauthammer et al. (1986) modified the model to account for the effects of compression and rate effects by applying an enhancement factor of 1.4 (see Figure 2-14). This same approach is used for this present study.

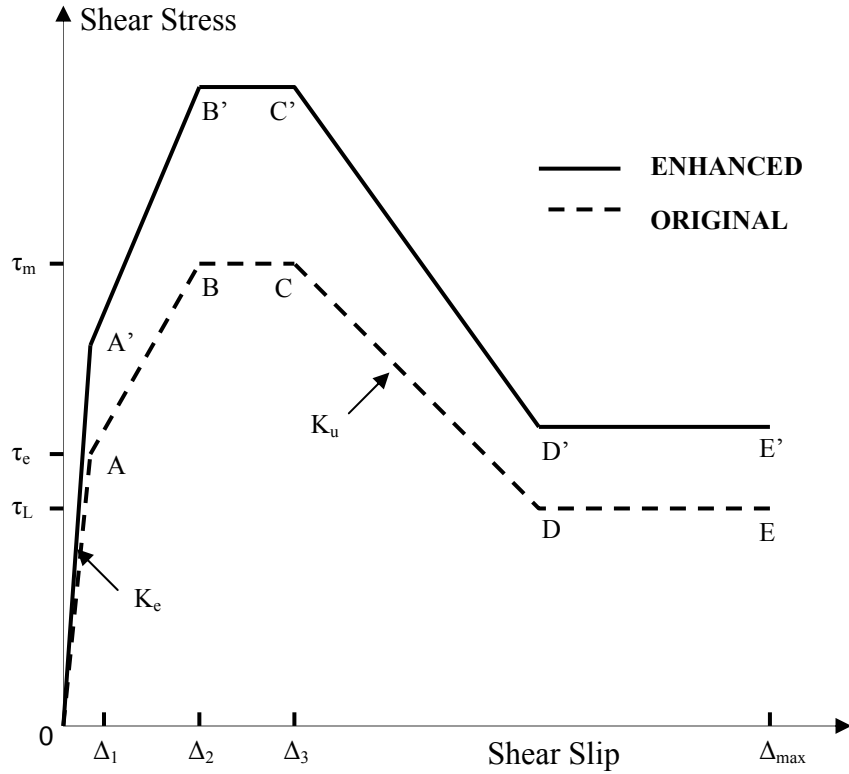


Figure 2-14. Hawkins model for direct shear stress-slip relationship (Krauthammer et al. 1986).

A detailed description of the model is given below.

Region OA: The response is assumed elastic and the slope, K_e , is defined by the shear resistance, τ_e , for a slip of 0.004 inch. The resistance is given by the following expression

$$\tau_e = 165 + 0.157 f'_c \tag{2-35}$$

where both τ_m and f'_c are in psi. The response should be taken to be elastic and not greater than $\tau_m / 2$.

Region AB: The slope of the curve decrease continuity with increasing displacements until a maximum strength, τ_m is reached at a slip of 0.012 inch. The maximum strength is given by

$$\tau_m = 8\sqrt{f'_c} + 0.8\rho_{vt}f_y \tag{2-36}$$

where both τ_m , f'_c and f_y are in psi, ρ_{vt} is the ratio of total reinforcement area to the area of plane that it crosses and f_y is the yield strength of the reinforcement.

Region BC: The shear capacity remains constant with increasing slips. Point C corresponds to a slip of 0.024 inch.

Region CD: The slope of the curve is negative, constant and independent of the amount of reinforcement crossing the shear plane. The slope is given by

$$K_u = 2000 + 0.75 f'_c \quad (2-37)$$

Region DE: The capacity remains essentially constant until failure occurs at a slip of Δ_{max} . For a well anchored bar, the slip for failure in inches is given by

$$\Delta_{max} = 2 \left(\frac{e^x - 1}{120} \right) \quad (2-38)$$

where

$$x = \frac{900}{2.86 \sqrt{\frac{f'_c}{d_b}}} \quad (2-39)$$

and d_b is the bar diameter (in inch).

The limiting shear capacity, τ_L is given by

$$\tau_L = \frac{0.85 A_{sb} f'_s}{A_c} \quad (2-40)$$

where A_{sb} is the area of reinforcement, f'_s is the tensile strength of the reinforcement and A_c is the cross-sectional area.

2.5.8 Dynamic Resistance Function and Response

The governing equation of motion for the equivalent SDOF system (see Fig 2-15) is given by the following (Krauthammer et al. 1990).

$$\text{Flexural} \quad \ddot{x}(t) + 2\xi\omega' \dot{x}(t) + \frac{R}{M_e} = \frac{F_e(t)}{M_e} \quad (2-41)$$

$$\text{Direct Shear} \quad \ddot{y}(t) + 2\xi\omega' \dot{y}(t) + \frac{R}{M_e} = \frac{V(t)}{M_e} \quad (2-42)$$

where $x(t)$, $\dot{x}(t)$ and $\ddot{x}(t)$ are the flexural displacement, velocity and acceleration respectively;
 $y(t)$, $\dot{y}(t)$ and $\ddot{y}(t)$ are the direct shear slip, velocity and acceleration respectively;
 M_e is the equivalent mass;
 R is the dynamic resistance function;
 ω' is the natural circular frequency;
 ξ is the damping ratio;
 $F_e(t)$ is the equivalent forcing function; and
 $V(t)$ is the dynamic shear force

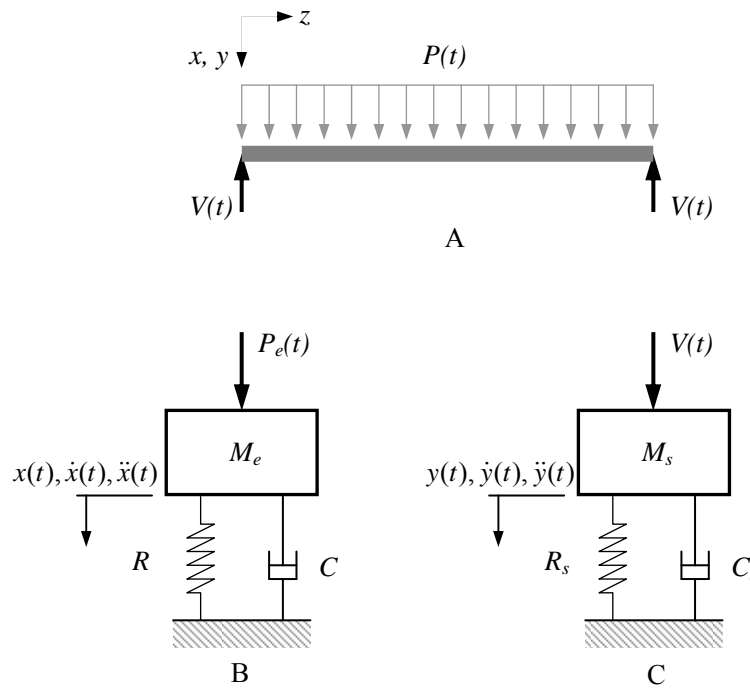


Figure 2-15. Equivalent SDOF systems for structural element (Krauthammer et al. 1990).
A) Continuous structural system. B) Flexural Response. C) Direct Shear Response.

The modeling of unloading-reloading paths is important in the analysis of a non-linear dynamic behavior. For an elastic perfectly plastic resistance function, the typical loading and unloading path is as shown in Figure 2-16A (Tedesco et al. 1998). Krauthammer et al. (1990) proposed a more realistic hysteretic loading-unloading looping as shown in Figure 2-16B.

As the loading acting on the slab increases, the resistance-displacement follows the resistance curve in the corresponding direction, (from Point O to Point A to Point B). If flexural failure (Point C) is not reached and unloading occurs, positive unloading path is assumed to follow a straight line BD, which has a stiffness value equals to the initial stiffness. Beyond Point D where negative unloading occurs, the unloading path is assumed to follow the straight line DB', where B' is a mirror image of the point of the last maximum displacement attained at Point B. Reloading path (e.g. EF) is assumed to remain parallel to BD and then traces towards Point B. If the reloading exceeds the displacement at Point B, it will reload along the resistance curve and Point B will march forward. The procedure will repeat for the next unloading cycle with a new position of Points B and B'. The unloading-reloading paths will affect the amount of internal damping from the hysteretic energy dissipation. For the direct shear mode of behavior, the unloading-reloading of the resistance curve follows the same procedures for the flexural resistance curve.

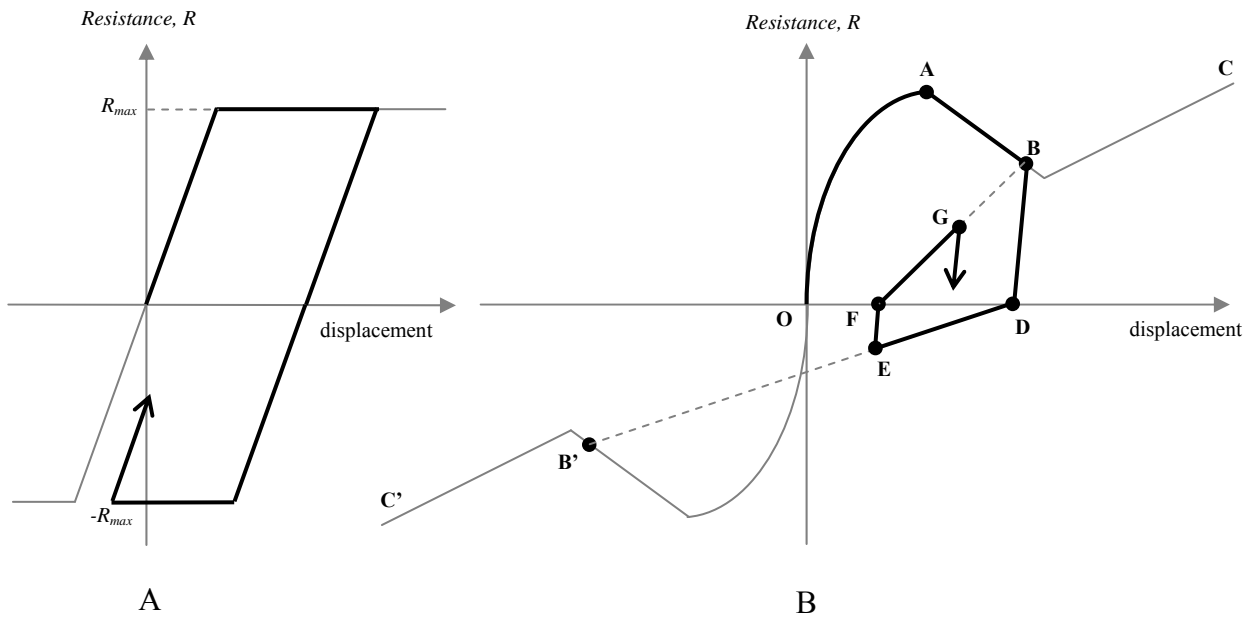


Figure 2-16. Dynamic flexural resistance functions. A) Typical elastic perfectly plastic function. B) Hysteretic loading-unloading.

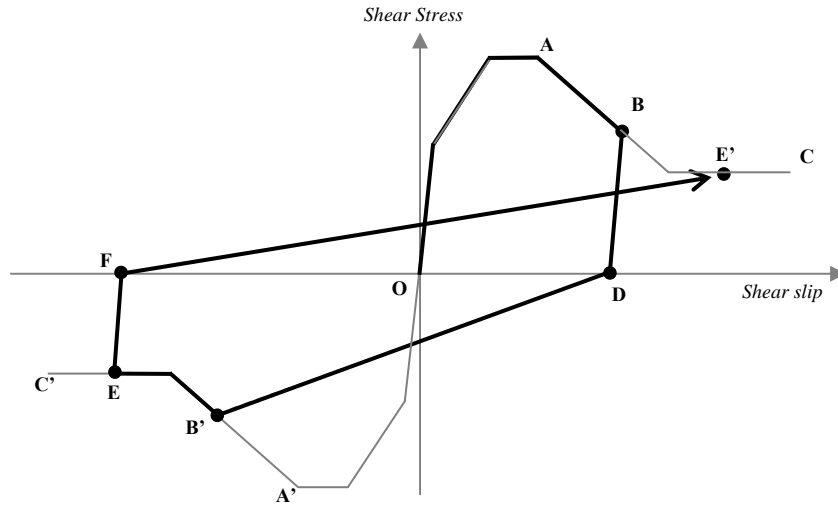


Figure 2-17. Dynamic direct shear resistance function.

2.6 Pressure-Impulse Diagrams and their Application

For structural dynamic analysis and design, it is often the final states (e.g. maximum displacement and stresses) of utmost relevance, instead of a detailed response time history of the structure. Pressure-impulse (P-I) diagrams are characteristic curves that describe the behavior of a structural component under different time dependent loads. These diagrams, often known as “iso-damage curves”, were developed to aid the assessment of structure against blast (May and Smith 1995). Detailed studies on pressure-impulse diagrams for beam and slab have been covered by Soh and Krauthammer (2004) and Ng (2004). Therefore, only a brief introduction on pressure-impulse diagrams and their applications will be covered.

2.6.1 Characteristics of P-I Diagram

A typical response spectrum for an undamped, perfectly elastic SDOF system is shown in Figure 2-18(a). In this figure, x_{\max} is the maximum displacement, M is the lumped mass, K is the spring stiffness, P_0 is the peak load, t_d is the load duration and T is the natural period. By defining a different set of axes, the same response spectrum can be transformed into a P-I diagram, Figure 2-18(b). The response spectrum focuses the influence of scaled time on the

system response, while the P-I diagram shows the combination of peak load and impulse for a given damage level (Soh and Krauthammer 2004).

With a damage level defined, the P-I curve indicates the combination of pressure and impulse values that will cause the specified damage. The curve divides the P-I diagram into two regions which indicate either failure or non-failure cases. Pressure and impulse points falling to the right and above the threshold curve indicates failure in excess of the specified damage level criterion. To the left and below the curve indicates no failure is induced.

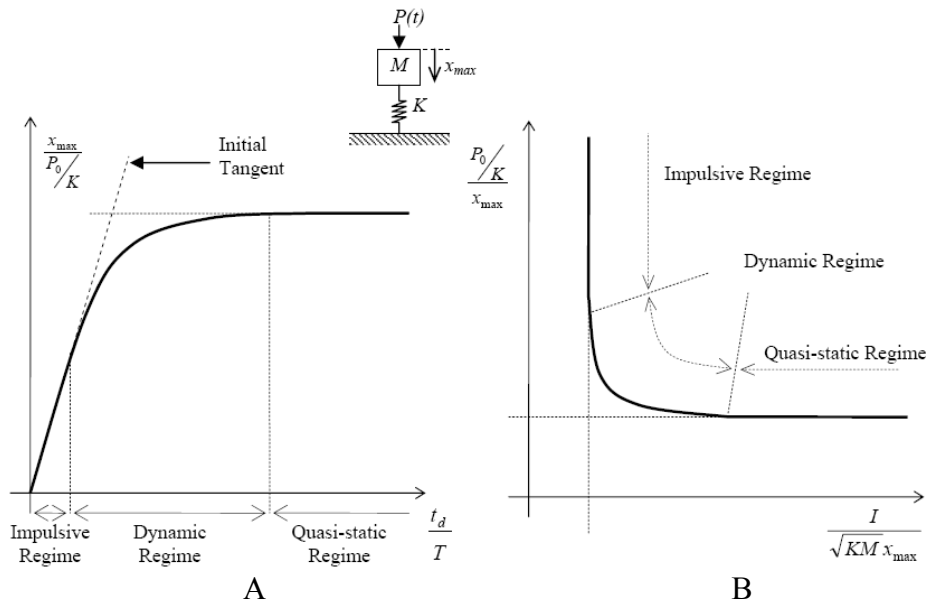


Figure 2-18. Typical response spectra and P-I diagram (Soh and Krauthammer 2004). A) Shock Spectrum. B) P-I diagram.

In structural dynamics, there is a strong relationship between the structural response and the ratio of the load duration to the natural period of the structure (Biggs 1964, Clough and Penzien 1993). This relationship can be categorized into the impulsive, dynamic and quasi-static regimes. As seen in Figure 2-18, the P-I diagram better differentiates the impulsive and quasi-static regimes, in the form of vertical and horizontal asymptotes.

2.6.2 Numerical Approach to P-I Diagram

Closed –form solutions of P-I diagram can be obtained for idealized structures subjected to a simplified load pulse (Ng 2004). However, in order to allow complex non-linear resistance functions and complex loading conditions to be considered, a numerical approach to generate the P-I diagram must be adopted. P-I diagram can be generated numerically by performing many single dynamic analysis. Each result from a dynamic analysis will determine whether the pressure and impulse combination is in the failure or non-failure region. With sufficient runs, a threshold curve can be plotted. Since it is computationally expensive to run all possible pressure and impulse combinations, an efficient search algorithm must be employed to locate the required threshold points (Krauthammer et al. 2008).

Soh and Krauthammer (2004) and Ng (2004) developed numerical procedures to numerically generate P-I diagram. Blasko et al. (2007) developed a more efficient search algorithm. The procedure uses a single radial search direction, originating from a pivot point (I_p , P_p) which is located in the failure zone of the P-I diagram (see Figure 2-19). Iterations using Bisection method are carried to generate the threshold curve. This approach can be applied effectively to any structural system for which a resistance function can be defined. The pressure-impulse diagrams which will be presented in the later part of this study are generated numerically using this same approach.

2.6.3 Multiple Failure Modes

In general, the response and failure for most structures can occur in more than one mode. Although flexure is usually the predominant mode, but under certain circumstances, failure may occur in other mode (e.g. direct shear). If there exists two a single failure modes, the P-I diagram will consists of two threshold curves, each representing a failure mode. The true threshold curve will therefore be represented by the lower bound of the two curves as shown by

the dotted line (see Figure 2-20). With the two threshold curves plotted, it is possible to identify the actual failure mode by plotting the pressure-impulse combination and examining which region the point is located.

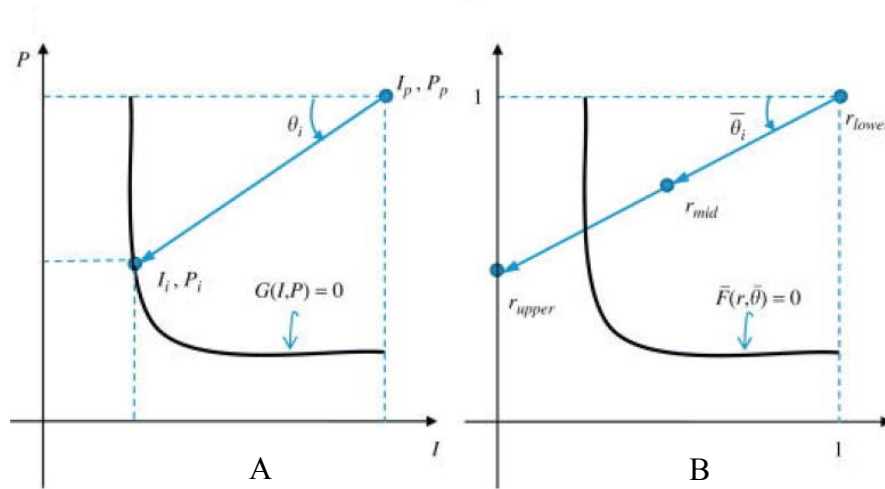


Figure 2-19. Search algorithm for P-I diagram (Blasko et al. 2007). A) Establish pivot point. B) Data pivot search

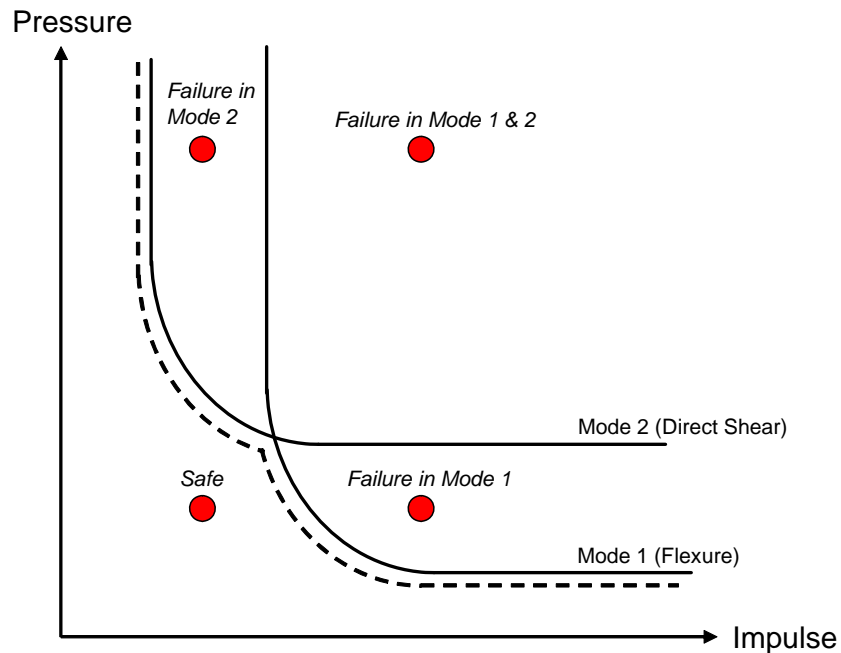


Figure 2-20. Pressure-Impulse diagram with two failure modes.

2.7 Summary

The background of the effects of blast loads on buried structures and the dynamic structural behavior and analysis were presented in this chapter. Pressure-impulse diagrams and their application were also briefly discussed. The different mode of behavior for reinforced concrete slabs under loading was discussed in greater detail in this chapter.

This chapter is the basis for the methodology to derive the numerical method for the dynamic analysis of shallow-buried reinforced concrete box-type structures subjected to air blast loadings in Chapter 3.

CHAPTER 3 METHODOLOGY

3.1 Introduction

For dynamic analysis of any structures, the material and constitutive models of the structure must first be derived in order to describe the relationship between the dynamic resistance (e.g. bending moment, shear forces) and the structure response (e.g. displacement). Then a suitable dynamic structural model (e.g. continuous system, multi degree of freedom, single degree of freedom) can be chosen to accurately represent the mechanical characteristics of the structure.

This chapter covers the methodology to generate the resistance functions for reinforced concrete slabs and the buried box structure in both the flexural mode (Section 3.2) and direct shear mode (Section 3.4). The issue of soil arching and the required modifications to the load and mass factors are discussed in details in Section 3.4. The effect of shear failure on the slab resistance is also discussed in Section 3.5. Lastly, a flowchart of the procedure is presented in Section 3.6.

3.2 Flexural Mode

As described in Section 2.4.1, the center point of the slab is chosen as the reference point for the single-degree-of-freedom system and the slab response is in accordance with the resistance function described in Section 2.5.4. However, for a buried box structure, several modifications have to be introduced into the approach described in Section 2.5.2 in order to account for certain conditions that will affect the system behavior.

3.2.1 Externally Applied Thrust

The peak structural resistance in the compression membrane mode can be enhanced if there is an external in-plane compressive force being applied to the slab (Krauthammer 1984).

The in-plane compressive force may exist in the form of prestressing force (Meamarian et al, 1994) or due to horizontal component of the vertical forces for a box structure buried in soil (Krauthammer et al. 1986).

For the box type structures under consideration, the in-plane compressive forces are generated by the horizontal component of the pressure pulse that propagates vertically through the soil from the air blast load on the surface (see Figure 3-1). These compressive forces vary with time and therefore have to be calculated at every time step of the analysis.

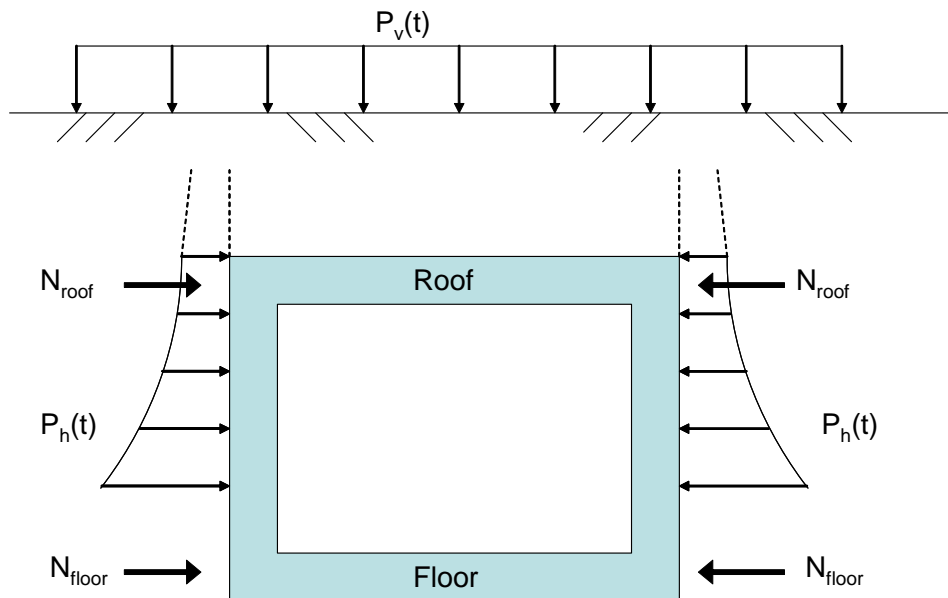


Figure 3-1. Model for externally applied thrust (Krauthammer et al. 1986).

In this study, the following procedure is implemented:

1. The wall is subdivided into n number of layers (see Figure 3-2). The depth at the mid-depth of each of the n layers is calculated and denoted as h_i . The time of arrival at each layer can be calculated by considering the seismic wave velocity of the soil.
2. The vertical pressure pulse in the soil is traced at each time step and the horizontal stress component is converted into point loads acting the each of the n layers.

3. The horizontal stresses generated by the propagating pressure pulse in the soil can be computed as a ratio of the vertical stress. The ratio is the coefficient of static lateral earth pressure, K_0 . The ratio is dependent on the effective friction angle of the soil and it can be estimated as about 1.0 for clay and about 0.5 for sand (Krauthammer et al. 1986).
4. The compressive thrust at the roof and floor can then be calculated from the points load acting at each layer. The compressive thrust, N_x and N_y , will be used in the formulation for the calculation of the enhanced membrane peak resistance.
5. When the whole vertical pressure pulse propagates beyond the floor level of the buried box structure, the compressive thrust (due to static earth pressure) remains constant and therefore need not be re-evaluated again at the further time steps.

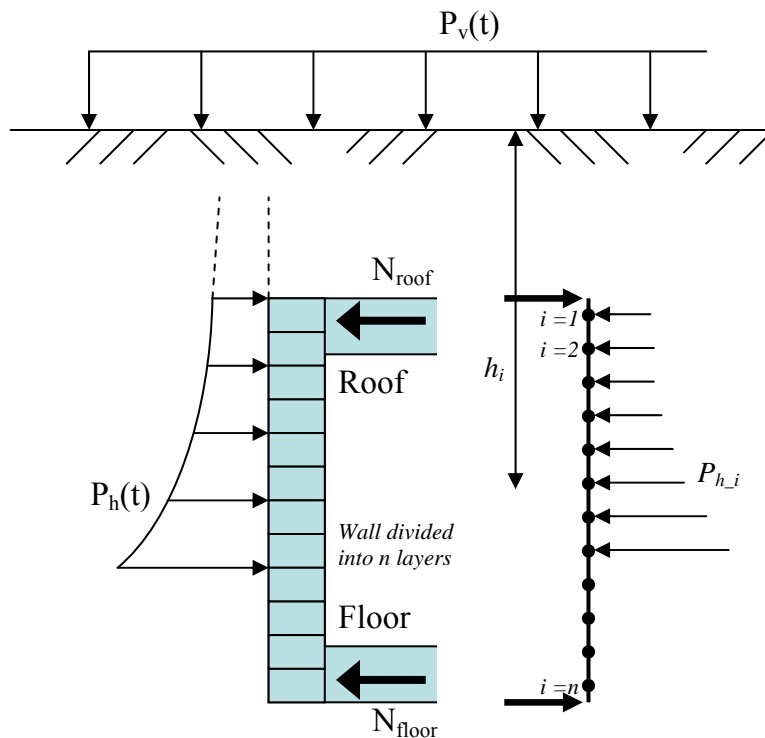


Figure 3-2. Calculation of externally applied thrust.

3.2.2 Numerical Approach for Resistance Curve Calculation

Following the plastic theory described in Section 2.5, some modifications were introduced in order to calculate the slab resistance at point B and point C (see Figure 2-5) more accurately. An externally applied thrust is included in the formulation. Instead of using the approximation of using the ACI stress block for the concrete compressive stress, the approach in this study is to divide the concrete into layers parallel to the neutral axis and the stresses and forces for all layers are determined based on the appropriate stress-strain relationship chosen (see Figure 3-3).

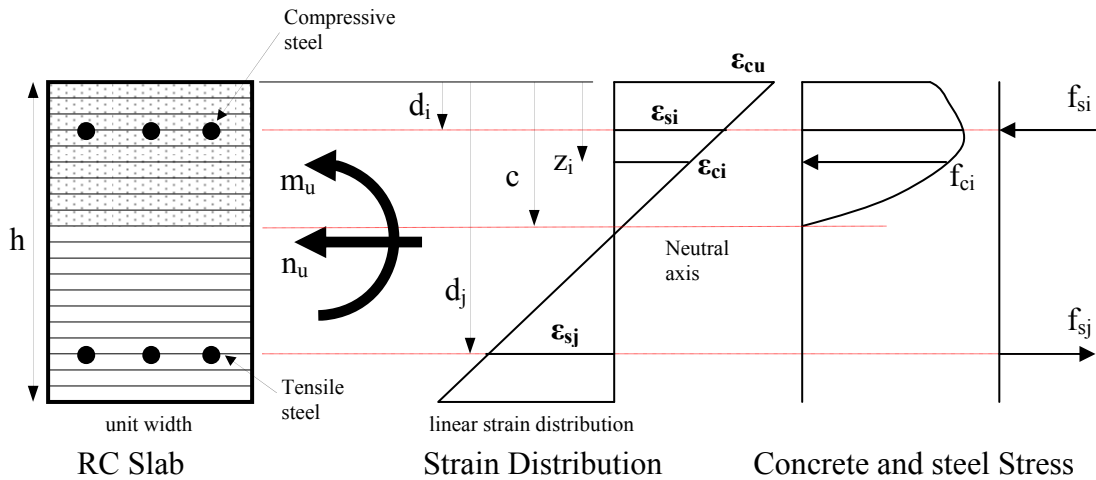


Figure 3-3. Stress and strain distributions across reinforced concrete section.

In this study, the concrete stress-strain relationship was based on the Hognestad model (MacGregor and Wight 2005) whereas for the reinforcing steel, the stress-strain model by Park and Paulay (1975) was used.

In Figures 3-4 and 3-5, the restrained strip with plastic hinges is applied with an external thrust. Using similar compatibility and equilibrium equations presented in Section 2.5.2, an iterative procedure is implemented in order to find the neutral axis depths that will be satisfied for each strip displacement. With the neutral axis depth, the corresponding axial forces and

moment in the strips can then be calculated. The slab resistance at point B and C of the resistance curve can then be determined based on the strips forces and moment.

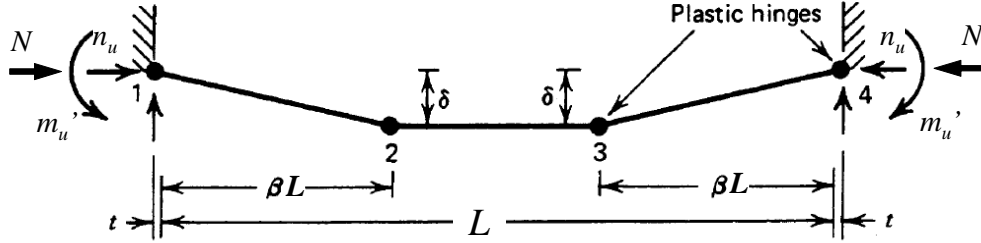


Figure 3-4. Restrained strip with external thrust.

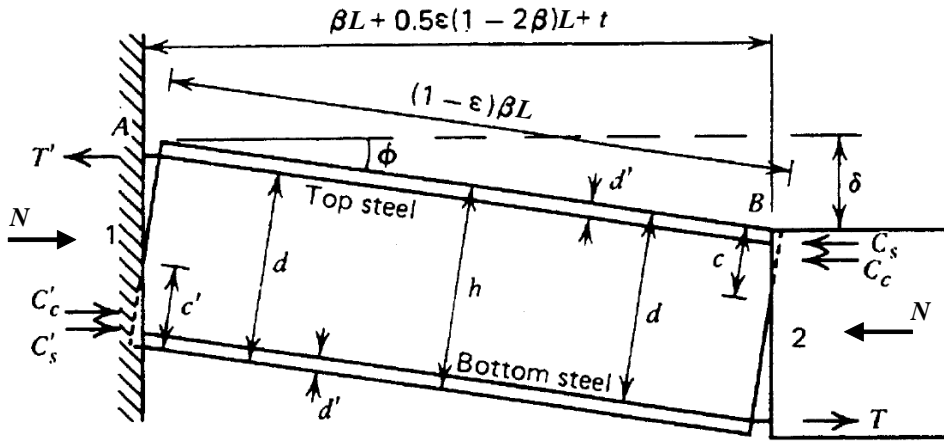


Figure 3-5. Portion of strip between plastic hinges with external thrust.

Based on the strain distribution and stress strain relationship (Figure 3-3), the concrete and steel stress for a unit width of the slab at yield Section 2 (Figure 3-5) can be expressed as a function of the neutral axis depth, c .

$$f_{si} = Fn(\varepsilon_{si}) = Fn\left(\frac{\varepsilon_{cu}}{c}(c - d_i)\right) \quad (3-1)$$

$$f_{ci} = Fn(\varepsilon_{ci}) = Fn\left(\frac{\varepsilon_{cu}}{c}(c - z_i)\right) \quad (3-$$

where ε_{si} and ε_{ci} are the steel and concrete strain, ε_{cu} is the ultimate concrete strain at failure, d_i

is the depth of reinforcing steel, z_i is the depth of concrete layer, c is the neutral axis depth and $F_n()$ represent the material stress-strain function.

The forces and moment for the steel and concrete can be expressed as

$$F_{si} = f_{si} A_{si} \quad (3-3)$$

$$F_{ci} = f_{ci} \Delta z \quad (3-4)$$

$$m_{si} = F_{si} (h/2 - d_{si}) \quad (3-5)$$

$$m_{ci} = F_{ci} (h/2 - z_i) \quad (3-6)$$

where F_{si} and F_{ci} are the steel and concrete layer force, m_{si} and m_{ci} are the steel and concrete layer moment about mid-height of slab section, A_{si} is the steel area, Δz is the concrete layer thickness, h is the slab thickness.

The total section moment, m_u , and axial force, n_u , can be calculated as:

$$m_u = \sum_i^{steel\ layers} m_{si} + \sum_i^{concrete\ layers} m_{ci} \quad (3-7)$$

$$n_u = \sum_i^{steel\ layers} F_{si} + \sum_i^{concrete\ layers} F_{ci} \quad (3-8)$$

Similarly, for yield Section 1 (Figure 3-5), m_u' and n_u' can also be expressed as a function of the neutral axis depth, c' .

Based on the geometry of the deformations, the compatibility equation can be written as

$$c' + c = h - \frac{\delta}{2} - \frac{\beta L^2}{2\delta} \left(\varepsilon + \frac{2t}{L} \right) \quad (3-9)$$

$$\text{and } \left(\varepsilon + \frac{2t}{L} \right) = \frac{n_u}{h.E_c} + \frac{2(n_u - N)}{L.S} = \varepsilon_{total} \quad (3-10)$$

where t is the outward lateral movement of the slab, E_c is the concrete elastic modulus and S is the surround stiffness.

For equilibrium, the membrane forces at Section 1 and 2 are equal

$$n_u = n'_u \quad (3-11)$$

Equations 3-10 and 3-11 can be rearranged and written as a function in c and c' :

$$R_1(c, c') = c' + c - h + \frac{\delta}{2} + \frac{\beta L^2}{2\delta} \left(\frac{n_u}{h.E_c} + \frac{2(n_u - N)}{L.S} \right) = 0 \quad (3-12)$$

$$R_2(c, c') = n_u - n'_u = 0 \quad (3-13)$$

For any displacement value, δ , the values of the neutral axis depth c and c' can be determined by solving Equations 3-12 and 3-13. In this study, Newton-Raphson iteration (Zienkiewicz and Taylor 2005) is used to solve the two equations numerically. With values of the neutral axis depth c and c' , the values of m_u , m'_u and n_u for each strip can be calculated using Equations 3-7 and 3-8.

By equating the internal virtual work done (Equation 2.16) to the external virtual work done by the loading on the strip, the load carried by the strip can be obtained for any assumed displacement value of the strip.

As presented in Section 2.6.2, the whole slab is assumed to be divided into x-direction and y-direction strips. With an assumed deflection value at the center of the slab, the strip deflection can be calculated and the force and moments in each strip are solved using the above procedure. The maximum slab resistance can then be determined using the appropriate displacement value at Point B on the slab resistance curve.

The resistance at Point C on the resistance curve is also calculated using the same procedure. The only difference is that the membrane forces are set as zero. The resistance at Point C corresponds to the Johansen's yield line load.

3.2.3 Variation of Mass and Load Factor

As presented in Section 2.4.2, to convert a continuous structure into an equivalent single-degree-of-freedom system, the equivalent parameters like the equivalent mass and equivalent loading and resistance function have to be evaluated using the appropriate mass and load factor.

Instead of applying a constant mass and load factor for analysis, a variation of the load and mass factor is proposed. As shown in Figure 3-6, the variation of the factors corresponds to the resistance curve for the slab. In the compressive membrane region of the resistance curve, the factors will varied from the elastic value at point A to the elastic-plastic value and then to the fully plastic value at point B, where the resistance is at the maximum. For the region represented by Point C to Point D, the factors used are the tension membrane value. A linear variation is assumed for the factors in between Points A to D.

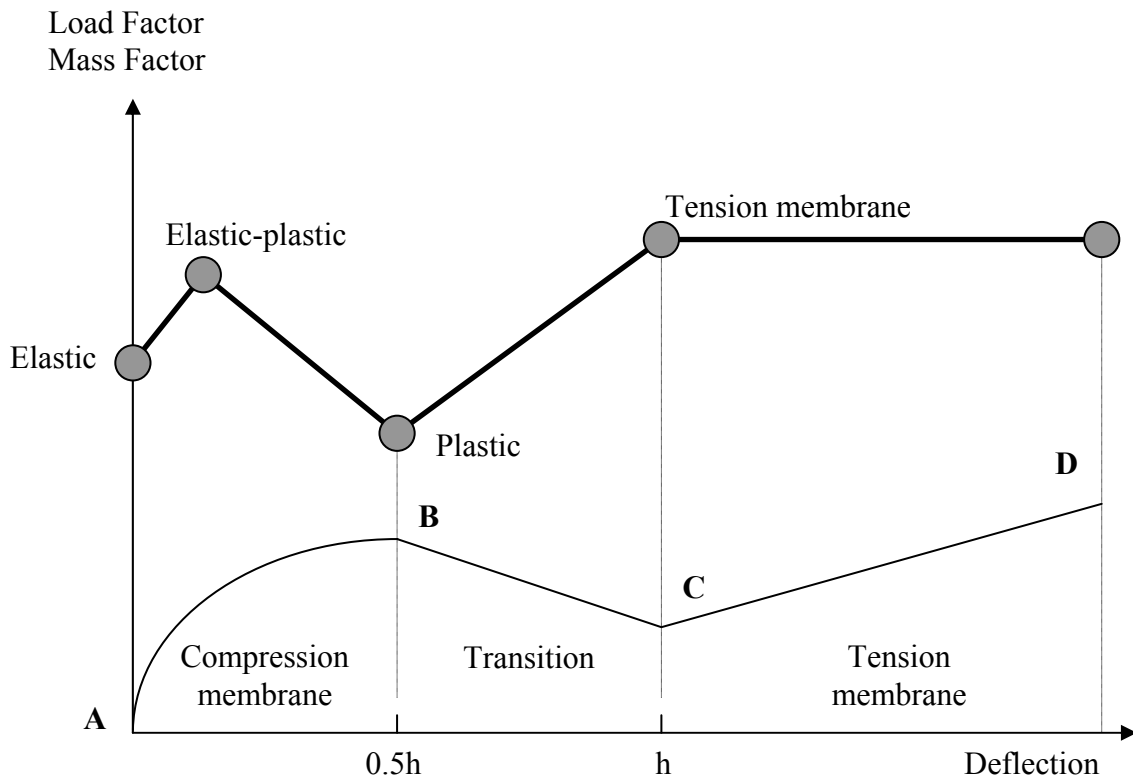


Figure 3-6. Variation of load and mass factor.

As mentioned in Section 2.4.2, the load and mass factors for beams and slabs under various loading and support conditions for different range of response can be found in Biggs (1964). The values for the load and mass factors for the tension membrane can also be found using the same approach. Taking a fixed end beam or one-way slab under uniform load as an example, the load and mass factor for the tension membrane can be calculated using Equations 2-16 and 2-18.

For the beam (or one-way slab) of length L in tension membrane, under a uniform applied load, the deformed shape can be assumed as a parabola. Therefore, the deformed shape function can be written as

$$\phi(x) = \frac{4}{L}x - \frac{4x^2}{L^2} \quad \text{for } 0 \leq x \leq L \quad (3-14)$$

From Equations 2-16 and 2-18,

$$K_M = \frac{M_e}{M_t} = \frac{\int_0^L m \phi^2(x) dx}{m.L} = \frac{\int_0^L \left(\frac{4}{L}x - \frac{4x^2}{L^2} \right)^2 dx}{L} \quad (3-15)$$

$$K_M = \frac{8}{15} = 0.533$$

$$K_L = \frac{F_e}{F_t} = \frac{\int_0^L p(t) \phi(x) dx}{p(t).L} = \frac{p(t) \int_0^L \left(\frac{4}{L}x - \frac{4x^2}{L^2} \right) dx}{p(t).L} \quad (3-16)$$

$$K_L = \frac{2}{3} = 0.667$$

Using the same approach, once the deflected shape for two-way slabs have been assumed, the load and mass factors can be obtained by integration over the entire slab surface.

3.3 Soil Structural Interaction

As presented in Section 2.3.1, one of important effect caused by the interaction between the structure and the surrounding soil is soil arching. Buried reinforced concrete box structures are usually much stiffer than their surrounding soil medium and will tend to attract load. Experimental data also showed that the pressure acting on the flexible center of the roof slab is significantly less than the applied overpressure acting on the free soil surface. The roof edges are relatively stiffer since they are supported by the walls and the pressure acting there are much higher. The pressure distribution is therefore not uniform.

The load reduction due to soil arching is accounted for by using the soil arching factor, C_a , as given by Equation 2-2. The load distribution effect has to be accounted for by adjusting the load and mass factors.

3.3.1 Influence of Parameters on Soil Arching Effect

The soil arching factor, C_a , represent the ratio of the average pressure acting on the roof slab to the applied surface pressure. Looking at Equation 2-2, we can see that the factors that will influence the value of the arching factor includes, the friction angle ϕ , the span ratio of the roof slab and the depth of burial of the roof slab.

Bowles (1996) provides some representative values for the angle of friction for different types of soil. Friction angle for cohesionless soils vary from 20° for loose silty sand to about 46° for dense sand. For cohesive soils such as clay, the friction angle is appreciably smaller than cohesionless soil. For saturated clayey soil with very small shear strength, the friction angle can be assumed as zero and there will be no soil arching effect.

The depth of burial for the roof slab is expressed as a ratio of the short span of the slab and in this study for shallow buried box structures, the ratio of burial depth to short span is limited to

a maximum value of 1.0. With regards to the slab span ratio, the arching ratio will be the maximum for a square slab, given the same soil properties and burial depth.

The variation of the soil arching factor (for a slab span ratio =1) with respect to the friction angle and burial depth is shown in Fig 3-7. From Figure 3-7, one can assume conservatively that the soil arching factor C_a will varies from a value of 0.3 (maximum soil arching effect) to a value of 1.0 (no soil arching) for different combination of parameters, including the friction angle, burial depth and span ratio.

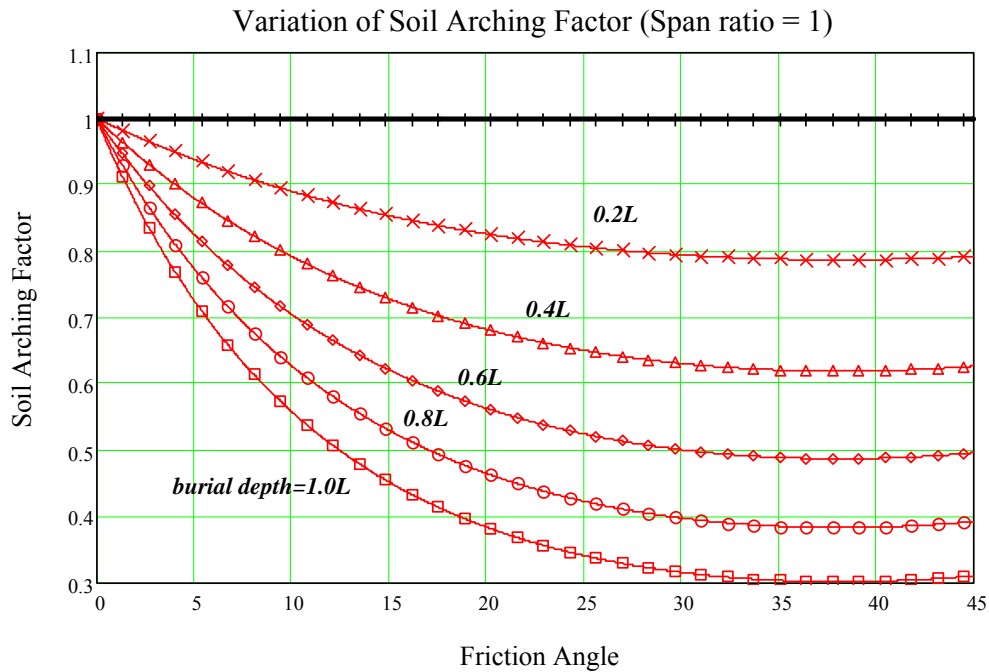


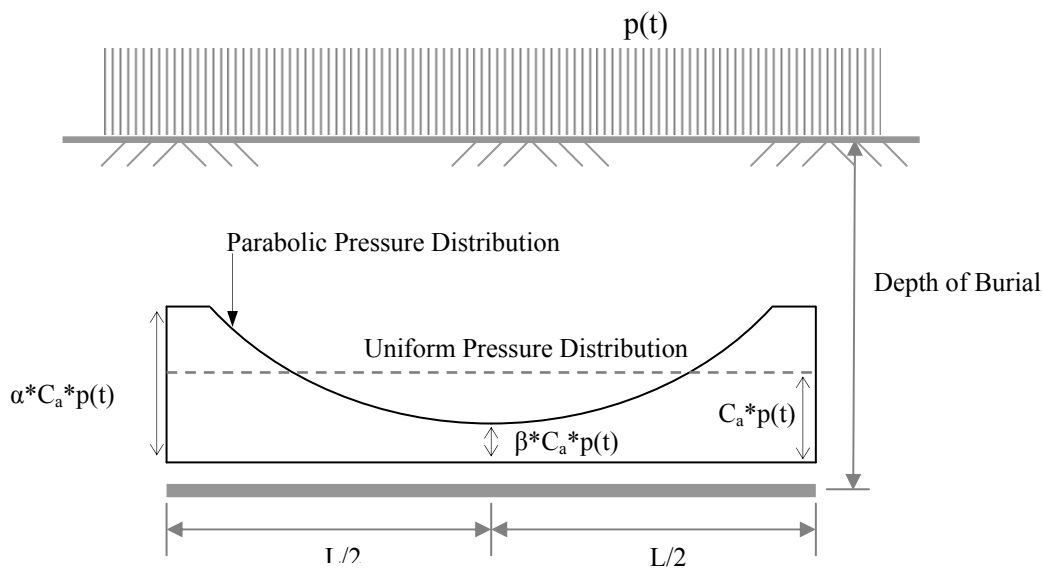
Figure 3-7. Variation of soil arching factor with friction angle and burial depth.

3.3.2 Effect on SDOF Load and Mass Factor

As presented in Section 2.4.2, the load factor and mass factor can be calculated based on the Equations 2-16 to 2-18. For a uniform loading case, Biggs (1964) had tabulated these factors for beam and slab with different support conditions.

Soil arching effect changes the load distribution and the uniform pressure applied on the soil surface is no longer uniform at the buried slab level. It is assumed that the pressure

distribution due to soil arching now follows a parabolic shape (Figure 3-8). The pressure at the centre of the slab or beam is assumed to be a factor β of the uniform pressure given by $C_a * p(t)$, where $p(t)$ is the applied pressure at the soil surface. Factor β will vary between 1 and 0, whereby value of 1 represent there is no soil arching effect; and value of 0 represent the presence of a maximum soil arching. Factor β will give an indication on the relative strength of the soil arching effect, based on the soil and geometric properties given in Section 3.3.1.



.Figure 3-8. Parabolic pressure distribution under soil arching.

Based on the assumed parabolic pressure distribution and Equation 2-18, one can calculate the new load factor, K_L , which will account for the effect of non-uniform pressure distribution acting on the slab in the equivalent SDOF system. The ratio λ_L defined by:

$$\lambda_L = \frac{K'_L}{K_L} \tag{3-17}$$

where K'_L is the load factor with soil arching parabolic pressure; and K_L is the normal load factor under uniform load.

The variation of ratio λ_L is plotted in Figure 3-9 for the four different cases, namely the elastic, elastic-plastic, plastic and tension membrane. The plot shows how the load factor changes with the soil arching factor. A linear function between the soil arching factor, C_a , and the ratio λ_L can be derived based on the plot. This function was used in the computer code to adjust the load factors used in the dynamic analysis based on the calculated arching factor value.

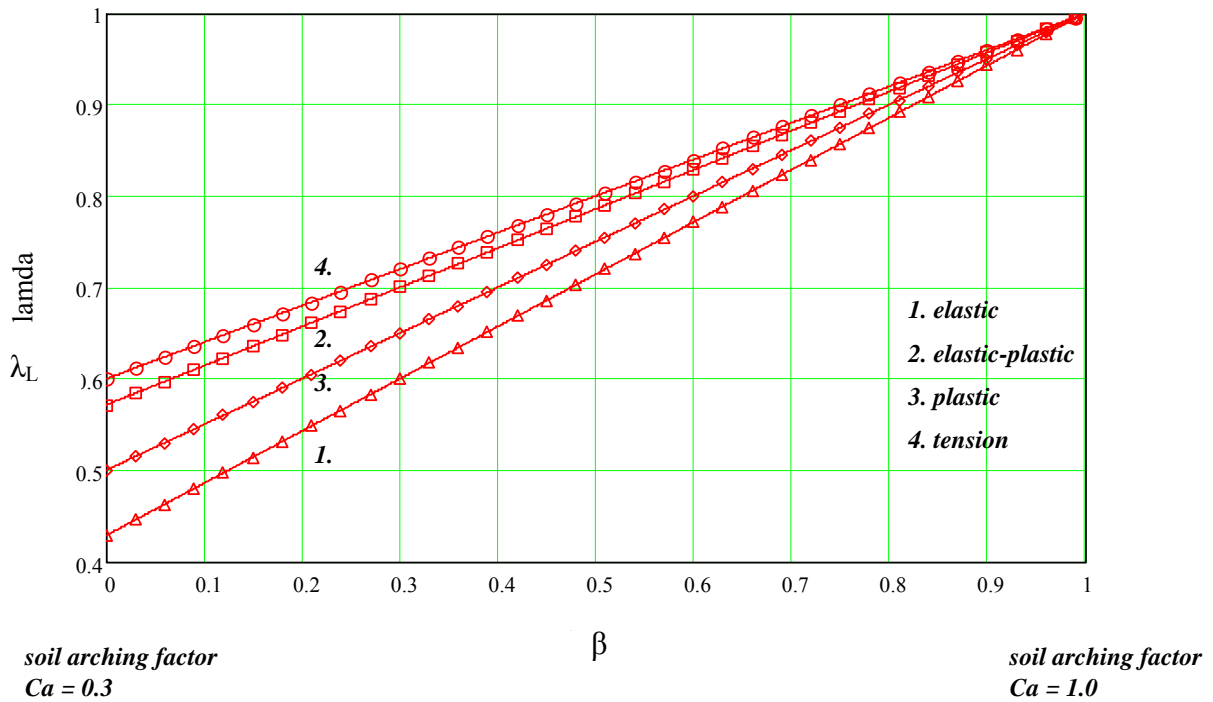


Figure 3-9. Variation of λ_L .

Based on Figure 3-9,

$$\lambda_{L_Elastic} = 0.816C_a + 0.1837 \quad (3-18A)$$

$$\lambda_{L_ElasticPlastic} = 0.612C_a + 0.3877 \quad (3-18B)$$

$$\lambda_{L_Plastic} = 0.714C_a + 0.2857 \quad (3-18C)$$

$$\lambda_{L_Tension} = 0.571C_a + 0.4286 \quad (3-18D)$$

Similarly, the mass factor has also to be adjusted due to soil arching effect. The mass factor for the structural slab will remain the same since soil arching does not actually affect it. Instead, the weight of the soil overburden which is acting on the slab will also be affected in the same manner described above. Due to active soil arching, more weight of the soil will be acting at the edges where the slab is stiffer and lesser weight on the center. Therefore, with a strong soil arching effect, it can be expected that less soil mass is active in the system response.

Using the same parabolic distribution profile for the soil mass, one can calculate the new soil mass factor, K_M , which will account for the soil arching effect on soil mass participation in the equivalent SDOF system. The ratio λ_M defined by:

$$\lambda_M = \frac{K'_M}{K_M} \quad (3-19)$$

where K'_M is the mass factor with soil arching parabolic profile; and K_M is the normal soil mass factor with uniform mass distribution.

The variation of ratio λ_M is plotted in Figure 3-10 for the four different cases, namely the elastic, elastic-plastic, plastic and tension membrane. The plot shows how the soil mass factor changes with the soil arching factor. A linear function between the soil arching factor, C_a , and the ratio λ_M can be derived based on the plot. This function is used in the computer code to adjust the soil mass factors based on the calculated arching factor value.

Based on Figure 3-10,

$$\lambda_{M_Elastic} = 1.039 C_a - 0.039 \quad (3-20A)$$

$$\lambda_{M_ElasticPlastic} = 0.863 C_a + 0.137 \quad (3-20B)$$

$$\lambda_{M_Plastic} = 1.0 C_a \quad (3-20C)$$

$$\lambda_{M_Tension} = 0.816 C_a + 0.1837 \quad (3-20D)$$

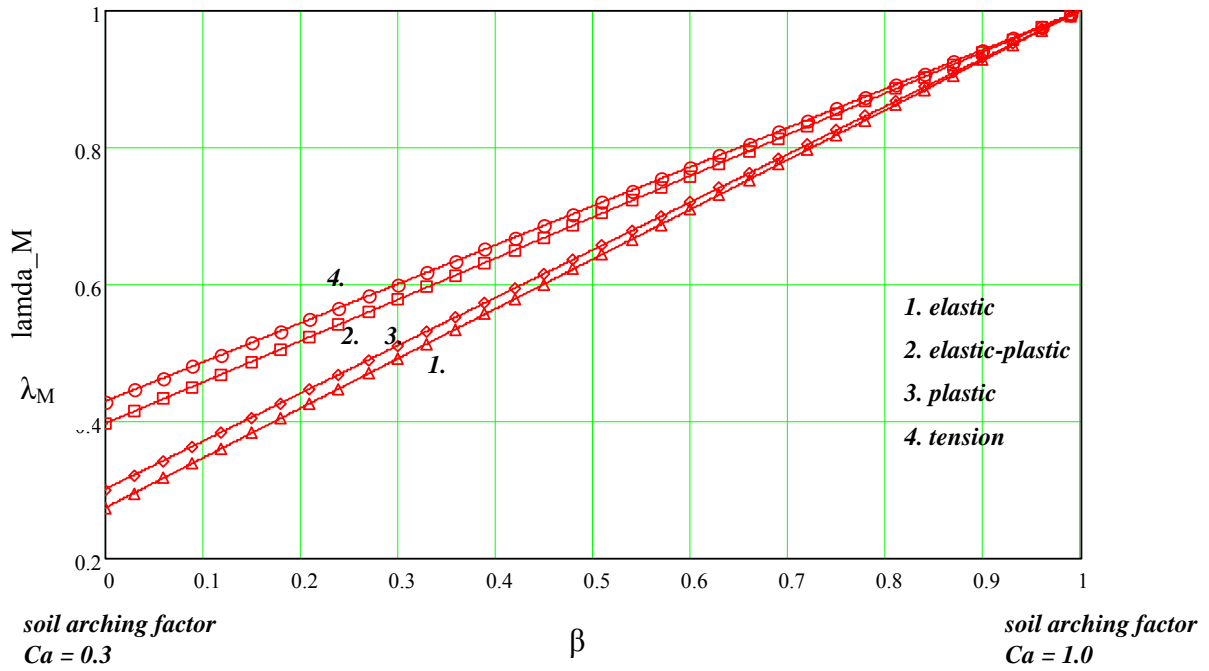


Figure 3-10. Variation of λ_M .

3.4 Direct Shear Mode

In the dynamic response for reinforced concrete slabs, beside the usual dominant flexural mode, it had been experimentally observed that slabs when subjected to severe impulsive loading have also shown to exhibit direct shear mode of failure.

3.4.1 Resistance Curve

As presented in Section 2.5.7, the direct shear model used in this study is based on a model proposed by Hawkins (1972) and modified by Krauthammer et al. (1986).

For reinforced concrete beam or one-way slab, the formulation presented in Section 2.5.6 can be used to generate the direct shear resistance curve. For a two-way slab where the longitudinal reinforcing steel in the x-direction and y-direction are different, the following approach is adopted to find the effective resistance curve.

The governing direct shear SDOF equation of motion can be written as

$$M_{ex} \ddot{w}_x(t) + C_x \dot{w}_x(t) + R_x = V_x(t) \quad (3-21)$$

$$M_{ey} \ddot{w}_y(t) + C_y \dot{w}_y(t) + R_y = V_y(t) \quad (3-22)$$

where M_{ex} and M_{ey} are the equivalent mass in x- and y-direction; C_x and C_y are the damping, R_x and R_y are the direct shear resistance; $V_x(t)$ and $V_y(t)$ are the dynamic shear force; and $\dot{w}(t)$ and $\ddot{w}(t)$ are the direct shear slip velocity and acceleration.

As shown in Figure 3-11, it is assumed that the reinforcement is the same at the supports for each x- and y-direction. Since the direct shear failure occurs at the very early stage of the loading, one can assume that the flexural mode of deformation is not significant and the whole slab displaced downwards as a rigid body motion. Therefore, Equations 3-21 and 3-22 can be simplified to

$$w_s(t) = w_x(t) = w_y(t); \dot{w}_s(t) = \dot{w}_x(t) = \dot{w}_y(t); \ddot{w}_s(t) = \ddot{w}_x(t) = \ddot{w}_y(t)$$

$$(M_{ex} + M_{ey}) \ddot{w}_s(t) + (C_x + C_y) \dot{w}_s(t) + (R_x + R_y) = (V_x(t) + V_y(t))$$

$$M_s \ddot{w}_s(t) + C_s \dot{w}_s(t) + R_s = V_s(t) \quad (3-23)$$

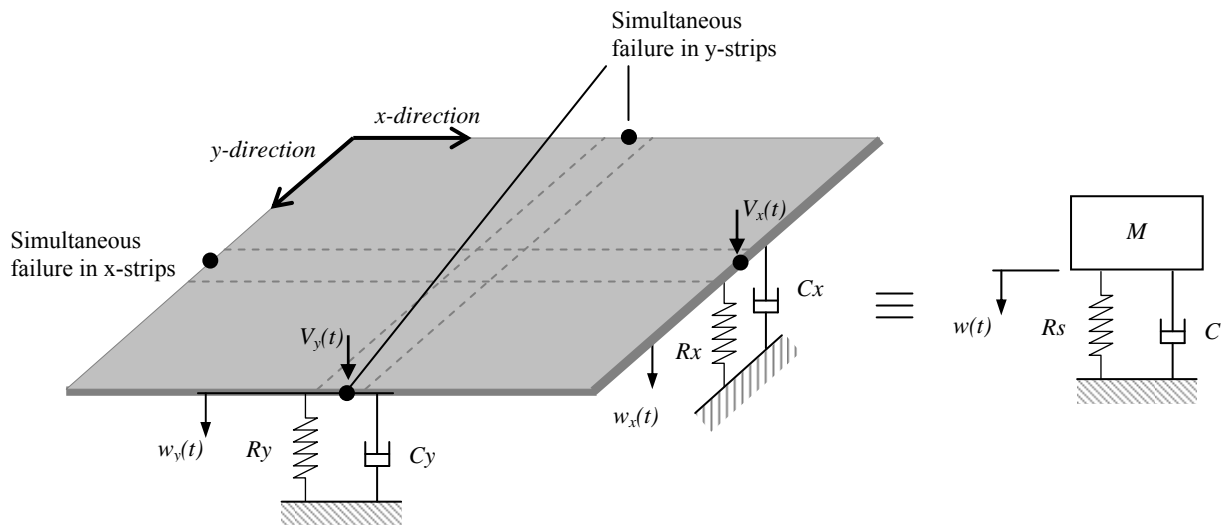


Figure 3-11. Direct shear model for two-way slab.

Therefore, the equivalent resistance for a two-way slab can be obtained by considering the resistance in the x-direction and y-direction and adding them together (see Figure 3-12).

The equivalent mass and loading for the single-degree-of-freedom system in direct shear was calculated by applying the appropriate transformation factors, using the same procedures presented in Section 2.4.2. The shear mass and load factors are presented in the next section.

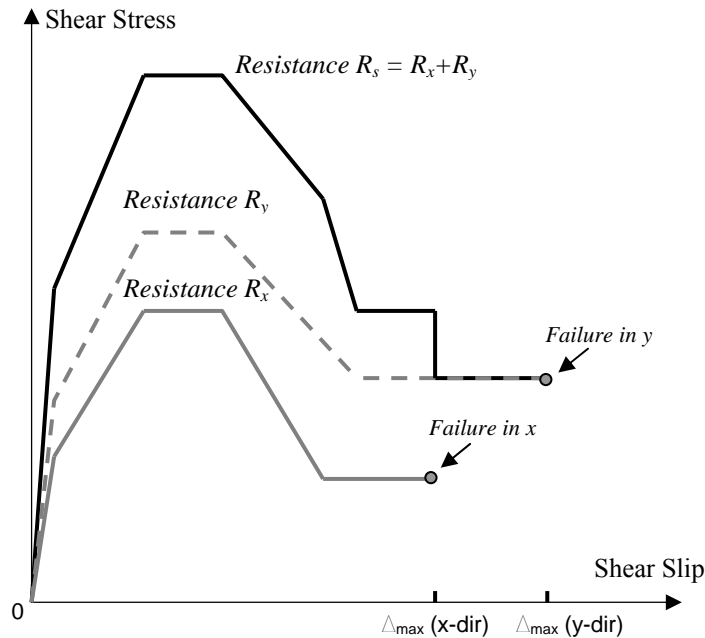


Figure 3-12. Direct shear resistance curve for two-way slab.

3.4.2 Shear Mass and Load Factors

The equivalent shear mass and load factors are computed based on the assumed mode and deformed shape of the slab under direct shear failure mode. Since the assumption for the slab under flexural mode deformation is a symmetrical plastic hinge formation, it requires that the steel reinforcement at the either sides of the support is the same. Therefore, simultaneous shear failure at the supports will occur and the deformed shape is as shown in Figure 3-13.

Based on the deformed shape, a shear mass factor of 1.0 can be taken for the structural slab. In addition, for a buried box structure, the mass of the soil overburden has to be considered

as well. Since the direct shear failure (if it was to occur) happened very early in the loading stage and the entire roof slab was pushed into the box, followed by the soil overburden, soil arching effect can be assumed be neglected in direct shear mode. Therefore, the entire mass of the soil overburden can be assumed be effective.

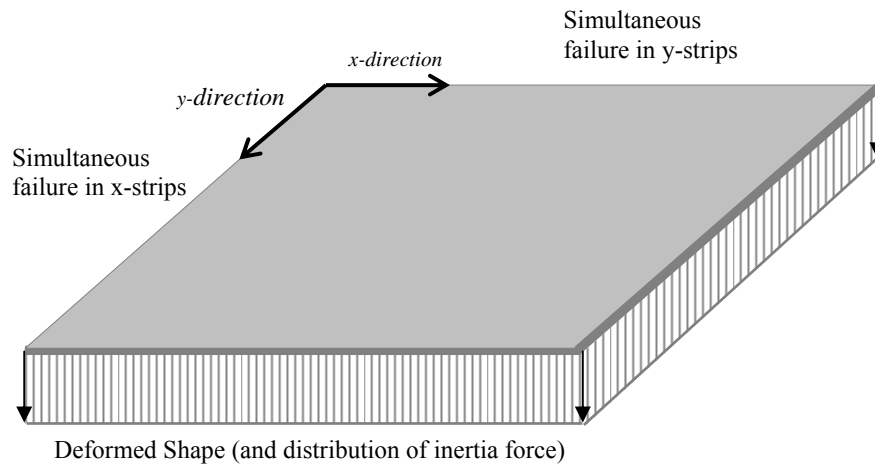


Figure 3-13. Deformed shape for direct shear response.

Using the same assumed deformed shape, the shear load and resistance factor can also be taken as 1.0, where the total resistance and loading for the entire slab is used in the SDOF equation of motion.

3.5 Shear Failure Mode for Slab

The flexural and direct shear modes of behavior of reinforced concrete slab have been considered in the previous Sections. Shear is generally not critical when slabs carry distributed loads and supported by walls or beams since the maximum shear force per unit length is relatively small (Park and Gamble 2000).

However, shear failure can become critical when the span to effective depth ratio is small and the corresponding flexural resistance due to membrane action increases. A photograph of a test specimen tested by Slawson (1984) which failed in a shear mode is shown in Figure 3-14. The shear failure occurs near the wall support where the shear stress level is the highest.



Figure 3-14. Slab in shear failure mode (Slawson 1984).

In order to model the shear failure mode, it was proposed to implement a simplified modification to the flexural resistance curve as shown in Figure 3-15. When the applied load is increased from point A, the initial resistance will follow the path towards point B, which is representative of the flexure resistance in the compressive membrane zone. With continued loading and if the shear strength of the slab section is lower than the maximum flexural resistance, w_{\max} , the slab will failed in shear at point B'. With the increase of load and deflection beyond point B', the slab will continue to deform in the flexure mode towards the Johansen's yield line load (point C). Beyond point C, the slab will behave in the tension membrane mode until the slab reinforcement failed at point D.

The nominal shear strength of a reinforced concrete section is given by:

$$V_n = V_c + V_s \quad (3-24)$$

where V_n is the nominal shear strength, V_c and V_s are the shear strength provided by concrete and steel reinforcement respectively.

Nawy (2000) states that for a deep beam or one-way slab section, where the clear span to effective depth ratio is less than 5, the shear resisting force of concrete and shear reinforcement can be calculated using the following expressions.

$$V_c = 2\sqrt{f'_c} b_w d \quad (3-25)$$

$$V_s = \left(\frac{A_v}{s_v} \frac{1+l_n/d}{12} + \frac{A_{vh}}{s_h} \frac{11-l_n/d}{12} \right) f_y d \quad (3-26)$$

where b_w is the width; d is the effective depth; f'_c is the concrete strength; f_y is the steel yield strength; l_n is the clear span of beam/slab; A_v is the total area of vertical reinforcement; A_{vh} is the total area of horizontal reinforcement; s_v is the horizontal spacing of the vertical reinforcement and s_h is the vertical spacing of the horizontal reinforcement.

3.6 Program Flowchart

The flowchart of the proposed procedure to generate the resistance function and solving the equation of motion for the required dynamic response is shown in Figure 3-16.

The approach consists of two SDOF systems for evaluating the flexural response and the direct shear response separately. For the flexural mode or response, the resistance function has to be re-calculated at each time step since the maximum resistance is dependent on the wall force for a buried box structure.

For the plotting of Pressure-Impulse diagram, this program will be used to solve the system for each pressure-impulse iteration run in order to generate the threshold curve, following the process described in Section 2.6.2.

3.7 Summary

This chapter presented the methodology to generate the resistance function for buried box structure for both flexural and direct shear mode of behavior. A variation of the load and mass

factor with respect to the resistance curve and the modification on these factors due to soil arching effect were discussed. The modification to consider shear failure mode was also presented.

The proposed methodology was implemented in a computer language and the numerical analysis results generated will be presented in Chapter 4.

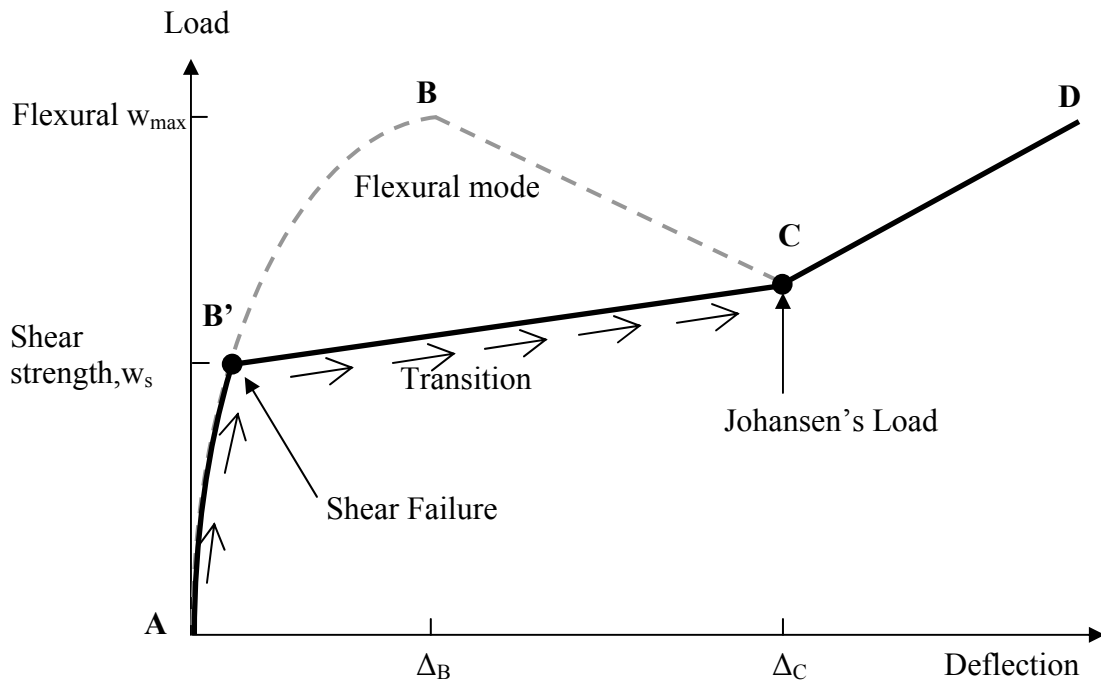


Figure 3-15. Resistance curve for slab with shear failure mode.

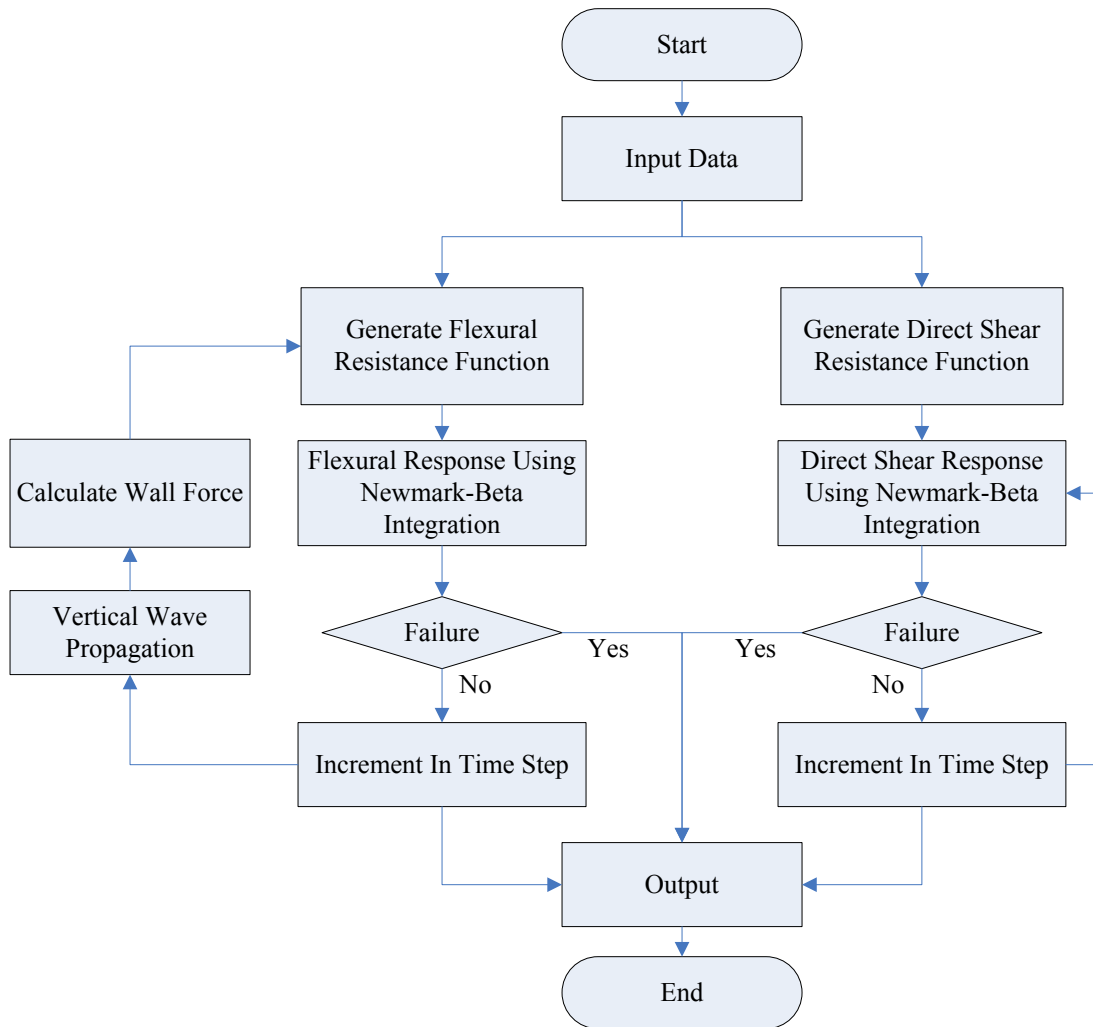


Figure 3-16. Program flowchart.

CHAPTER 4 RESULTS AND DISCUSSIONS

4.1 Introduction

The proposed procedure discussed in Chapter 3 was implemented in a computer programming language to test its viability. The results generated using the procedure are compared with the available data from past experimental work carried out on shallow buried reinforced concrete box structures subjected to airblast loading. This validation of the numerical procedure will be presented in Section 4.2. In Section 4.3, the assessment on the same set of experimental results using Pressure-Impulse diagrams was demonstrated.

4.2 Validation with Experimental Data

The capability of the proposed numerical procedure to perform dynamic analysis for reinforced concrete box structure subjected to airblast loads is presented. Experimental data from the tests conducted by Kiger and Getchell (1980) was used to validate the proposed methodology presented in Chapter 3.

The experimental test series conducted by Kiger and Getchell (1980) consisted of a total number of seven tests on shallow buried reinforced concrete box structures subjected to airblast loads. The airblast loads was a simulation of a distant nuclear explosion with a sharp rise time and a uniform pressure over the top of the soil surface. Details of the experiment are given in the Appendix.

The test series consisted of a total of 7 cases, whereby six of them are single bay rectangular box structures and another one a multi-bay box structure. Dynamic analysis was conducted and the flexural and direct shear response time history and resistance functions were generated for each test. The forcing function was obtained from the airblast gauge on the free surface and the damping ratio used was 20% for flexural analysis and 5% for direct shear

analysis. A high damping ratio for the flexural mode was used to consider the significant energy dissipation due to soil-structure interaction (Krauthammer et al. 1986). The numerical results were compared against the measured test data and the comparison is presented in the following sections.

4.2.1 Test FH1

Test FH1 was conducted in a sand (non-cohesive) backfill at a depth of burial (DOB) equal to 50% of the short clean span. The reinforced concrete box had wall, floor and roof thickness of 5.6 inches, giving the roof slab a span to effective depth ratio of 10. The structure had one percent principal reinforcing steel in each face, with a concrete strength of 7000psi. The test charge density was 0.9 lb/ft^3 and produced a peak pressure of 2400psi.

The roof and floor of the structure suffered cracking and some permanent deflections, but there was no structural failure. The top surface had longitudinal cracks, located roughly above the inside walls, almost the entire length of the structure. The roof had a maximum permanent deflection at its midspan of about 0.44 inch. A photograph of the box slab after the sand backfill was excavated is shown in Figure 4-1.

The displacement time history for the flexural degree-of-freedom is plotted in Figure 4-2. The numerical results show that the permanent displacement at the center of the roof slab is about 0.5 inch, which compares well with the experimental result. The numerical analysis also indicated that the slab flexural response is still within the compression membrane mode. The flexural resistance function for FH1 is shown in Figure 4-3.

The numerical analysis shows that the roof slab did not fail in the direct shear mode, which is consistent with the experimental observation. The displacement time history and resistance function for the direct shear degree-of-freedom are plotted in Figures 4-4 and 4-5.

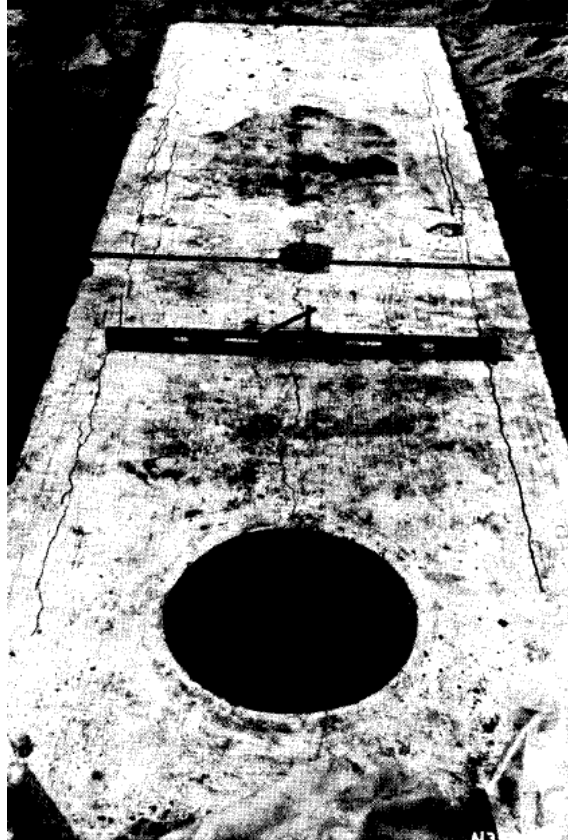


Figure 4-1. Post test view of FH1.

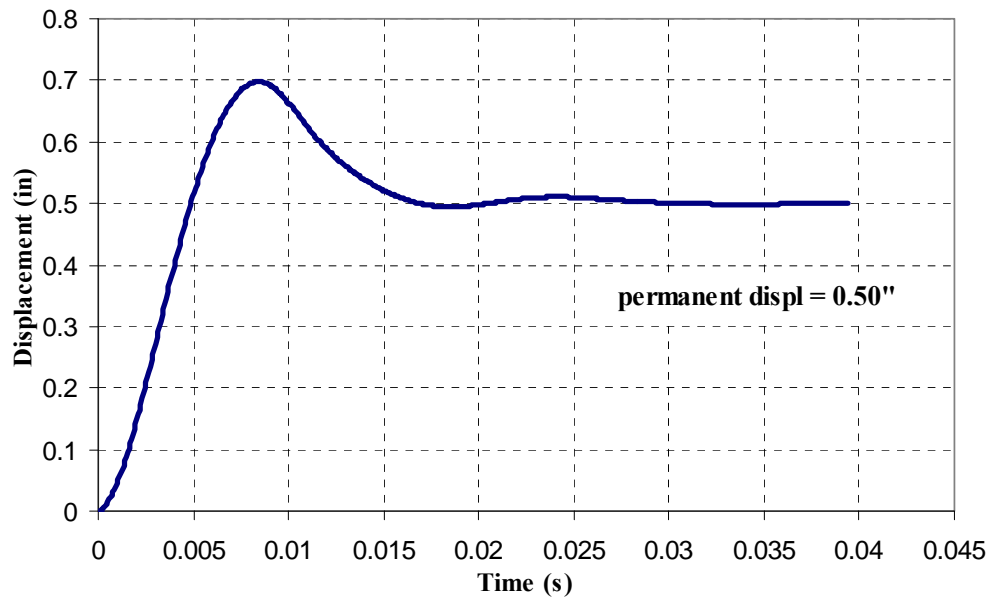


Figure 4-2. FH1 flexural displacement time history.

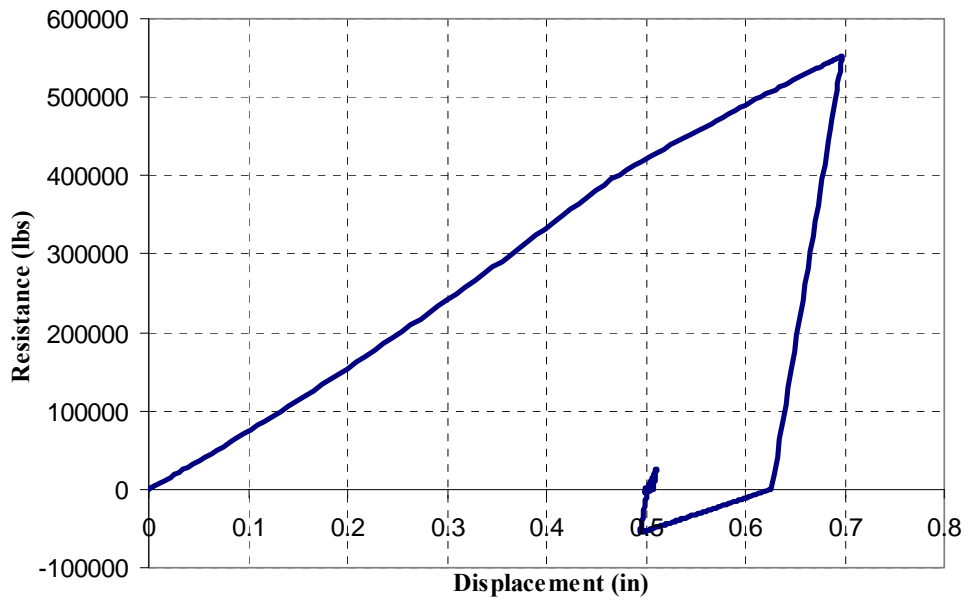


Figure 4-3. FH1 flexural resistance function.

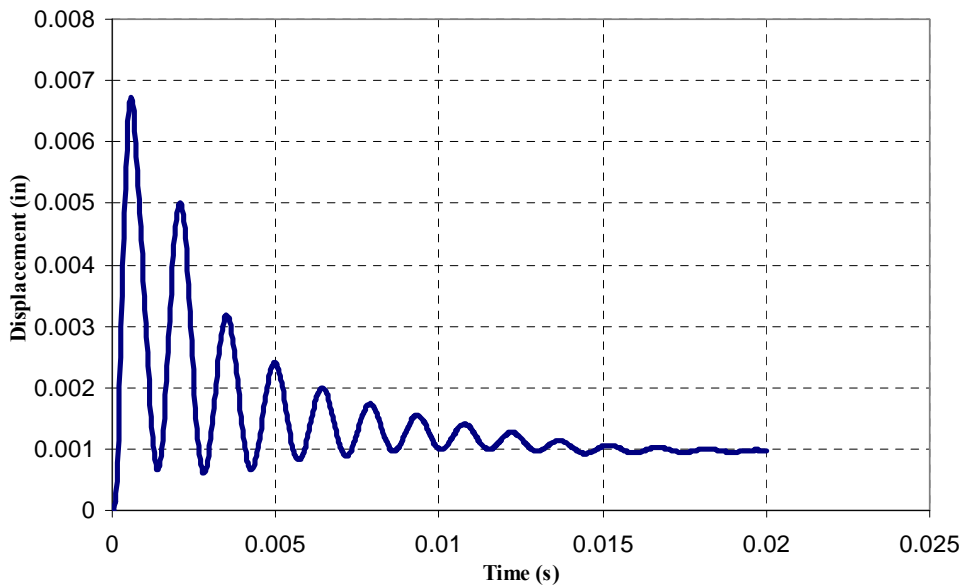


Figure 4-4. FH1 direct shear displacement time history.

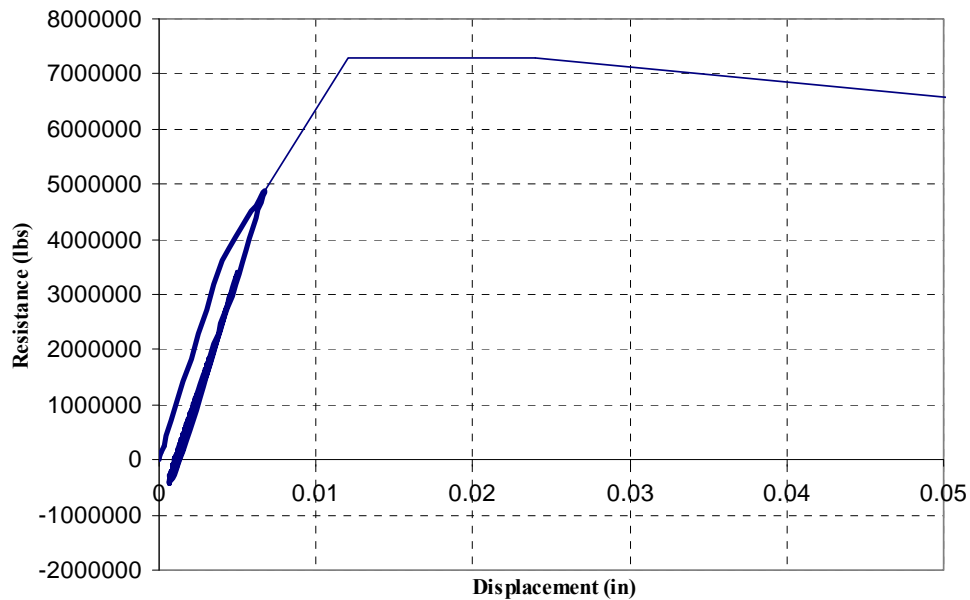


Figure 4-5. FH1 direct shear resistance function.

4.2.2 Test FH2

Test FH2 was conducted in a sand (non-cohesive) backfill at a depth of burial (DOB) equal to 50% of the short clean span. The reinforced concrete box had wall, floor and roof thickness of 5.6 inches, giving the roof slab a span to effective depth ratio of 10. The structure had one percent principal reinforcing steel in each face, with a concrete strength of 5200psi. The test charge density was 2.7 lb/ft³ and produced a peak pressure of 5250 psi.

The test bed had a distinct, elongated depression above the top of the structure. Excavation of the test bed revealed that the roof of the structure suffered complete failure. Post test examination indicated that the roof had been sheared off at the wall supports. The principal steel reinforcing bars, except a few that were not broken near the corners of the end wall, were necked down and broken at the wall supports. An inspection of the reinforcement bars near the center of the roof slab did not indicate the occurrence of significant flexure behavior. A photograph of the box slab after the sand backfill was excavated is shown in Figure 4-6.

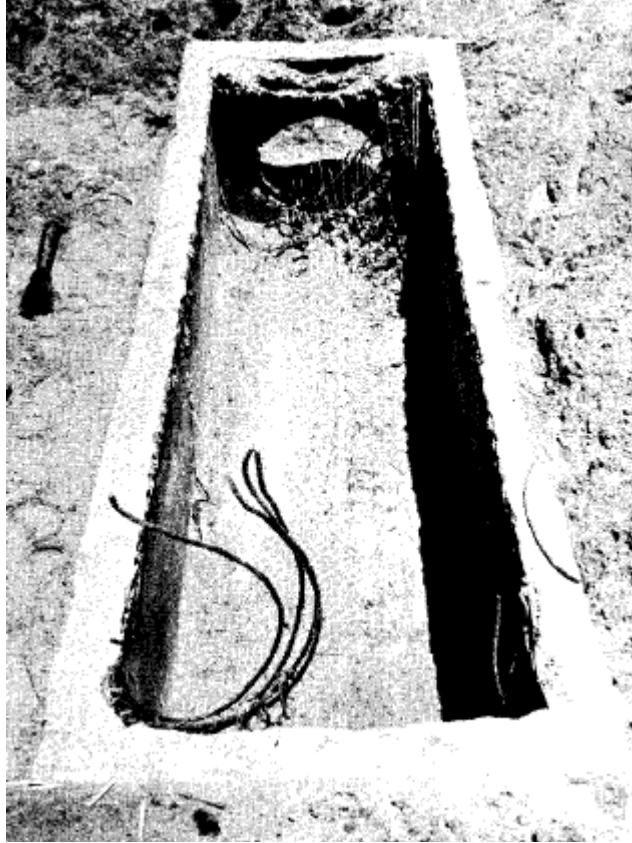


Figure 4-6. Post test view of FH2.

The displacement time history and resistance function for both the flexural and direct shear degree-of-freedom are plotted in Figure 4-7, 4-8, 4-9 and 4-10. The numerical results show that the roof slab failed in direct shear mode first, when the applied loading exceeded the direct shear resistance of the entire slab. The roof slab is also expected to fail in flexural mode in the numerical results. However, since the direct shear failure occurs at about 1 millisecond after the arrival of the loading, the slab will shear off the wall support and do not have enough time to go into the flexure response mode. The numerical prediction is therefore consistent with the experiment observation.

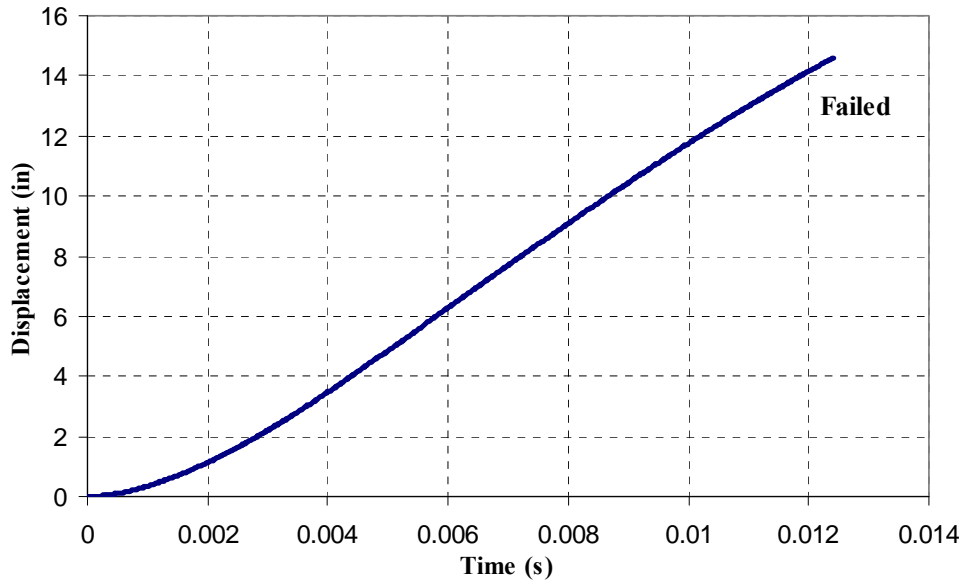


Figure 4-7. FH2 flexural displacement time history.

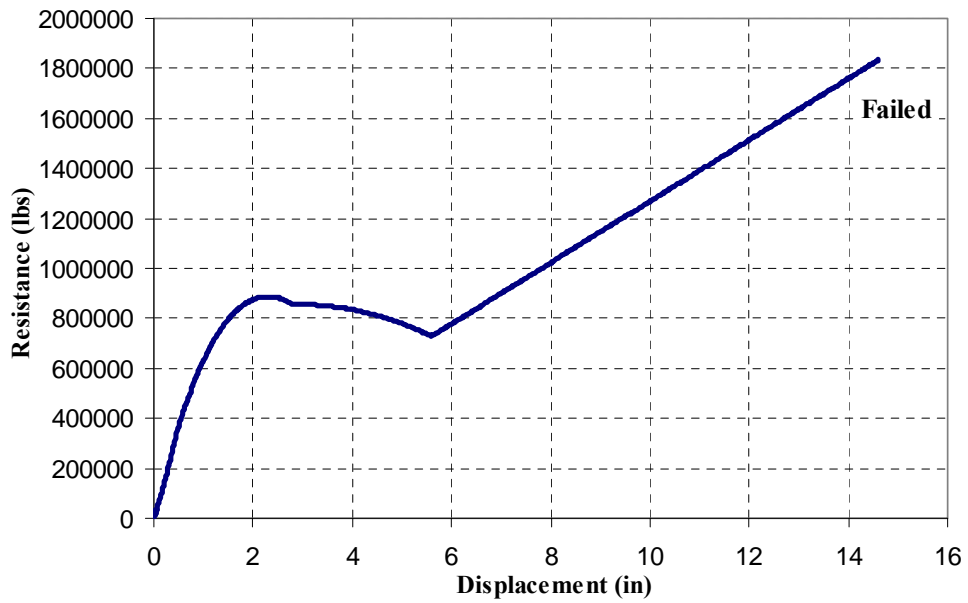


Figure 4-8. FH2 flexural resistance function.

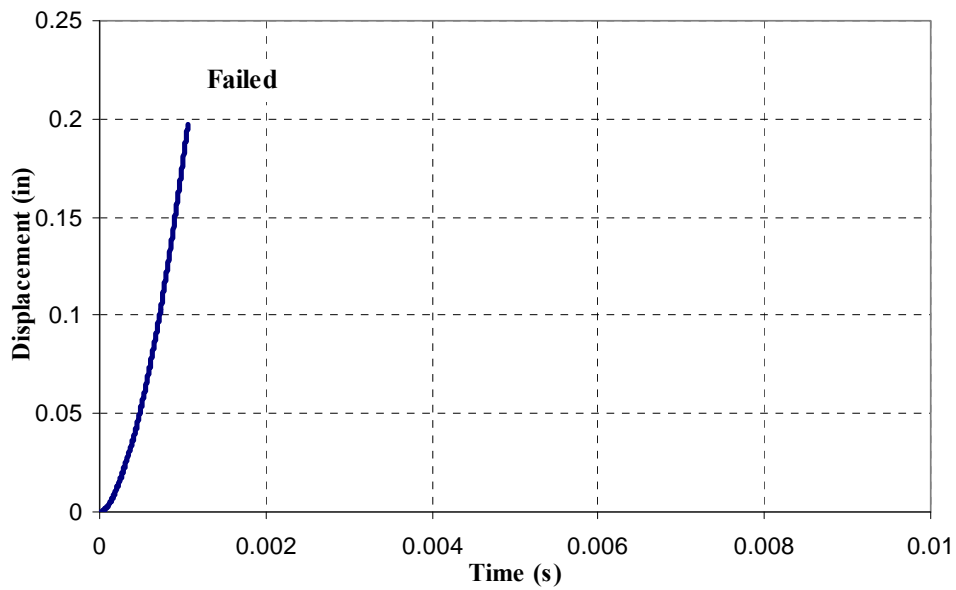


Figure 4-9. FH2 direct shear displacement time history.

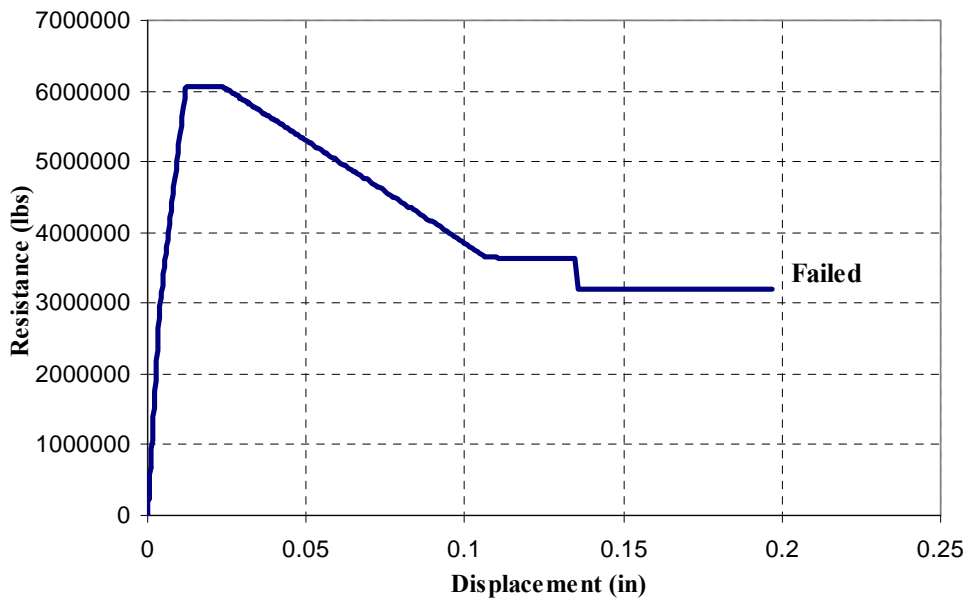


Figure 4-10. FH2 direct shear resistance function.

4.2.3 Test FH3

Test FH3 was conducted in a clay backfill at a depth of burial (DOB) equal to 50% of the short clean span. The clay backfill were wetted during the test to ensure the backfill would be a low shear strength material. The reinforced concrete box had wall, floor and roof thickness of 5.6 inches, giving the roof slab a span to effective depth ratio of 10. The structure had one percent principal reinforcing steel in each face, with a concrete strength of 7900psi. The test charge density was 0.9 lb/ft³ and produced a peak pressure of 2650psi.

After excavation, post test examination indicated that the roof slab responded primarily in the flexure mode, with a permanent center deflection of about 6 inches. Passive deflection gage recorded a maximum transient deflection of about 7 inches, indicating a rebound of about 1 inch after removal of load. Extensive longitudinal direction cracks were observed and they were concentrated along the edge of the wall supports and center area of the roof. This observation corresponded with a flexural response with three hinges forming at the two supports and at the center. The inside of the roof was extensively cracked longitudinally down the center with the concrete broken off and the reinforcing bars exposed. The exposed principal bars in the roof center were all necked down and some were broken. A photograph of the damaged box structure after excavation is shown in Figure 4-11.

The displacement time history and resistance function for the direct shear degree-of-freedom are plotted in Figure 4-12 and 4-13. The numerical results show that the roof slab did not fail in direct shear mode, same as the experimental observation.

The displacement time history for the flexural degree-of-freedom is plotted in Figure 4-14. The numerical results show that the permanent displacement at the center of the roof slab is about 5.9 inch, with a maximum transient deflection of 6.7 inches. This compares well with the experimental result. Looking at the resistance function shown in Figure 4-15, it indicates that the

slab underwent extensive deformation into the tensile membrane region. These numerical predictions are consistent with the experiment observations and measurement.



Figure 4-11. Post test view of FH3.

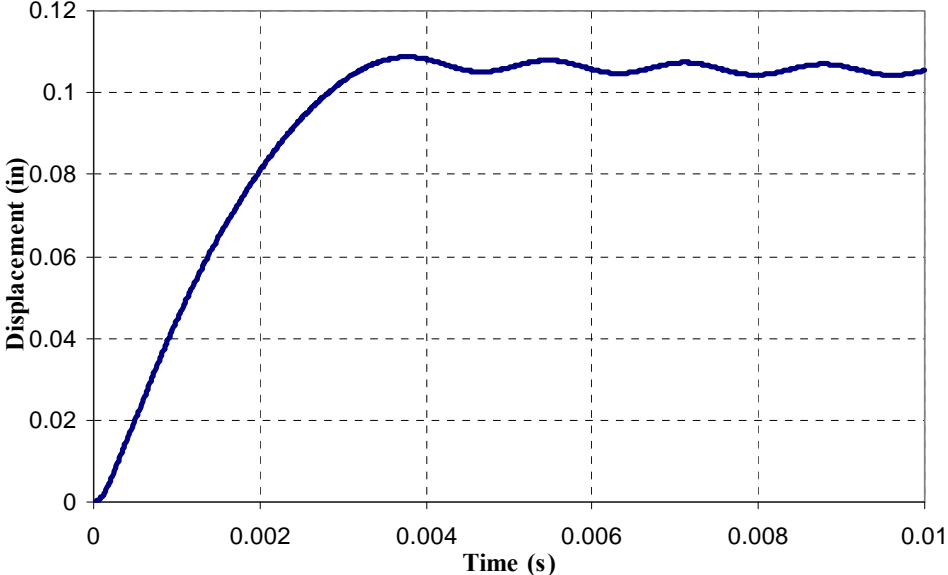


Figure 4-12. FH3 direct shear displacement time history.

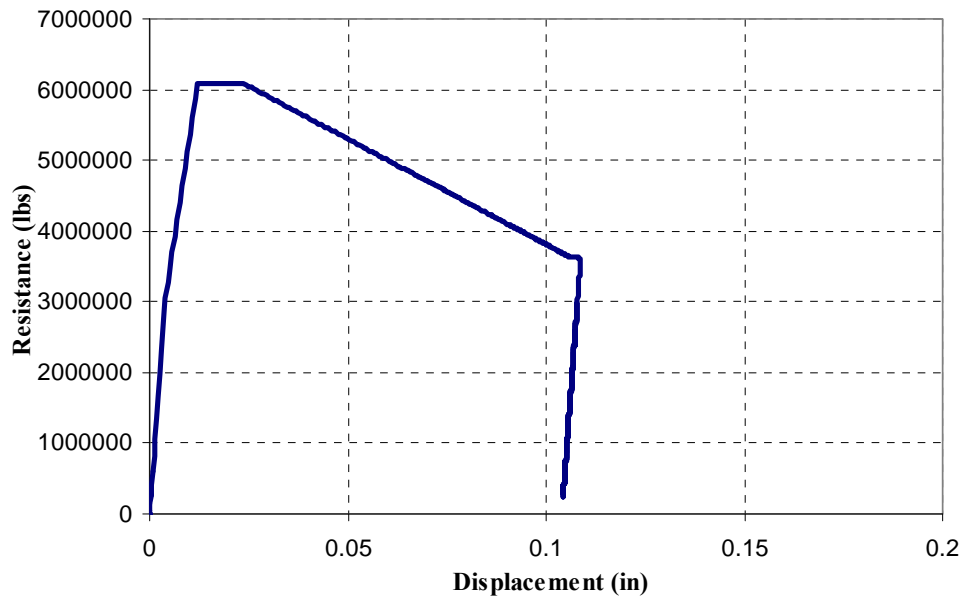


Figure 4-13. FH3 direct shear resistance function.

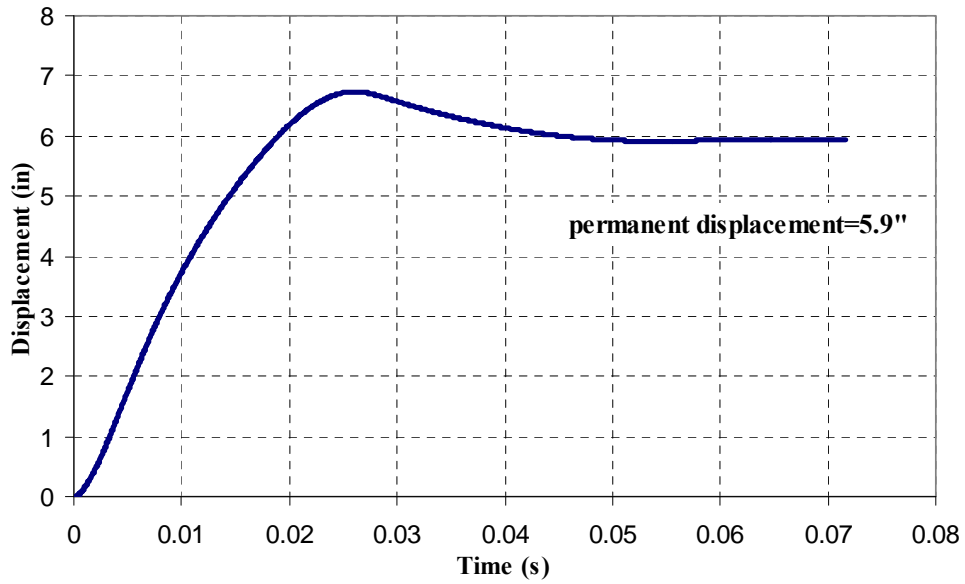


Figure 4-14. FH3 flexural displacement time history.

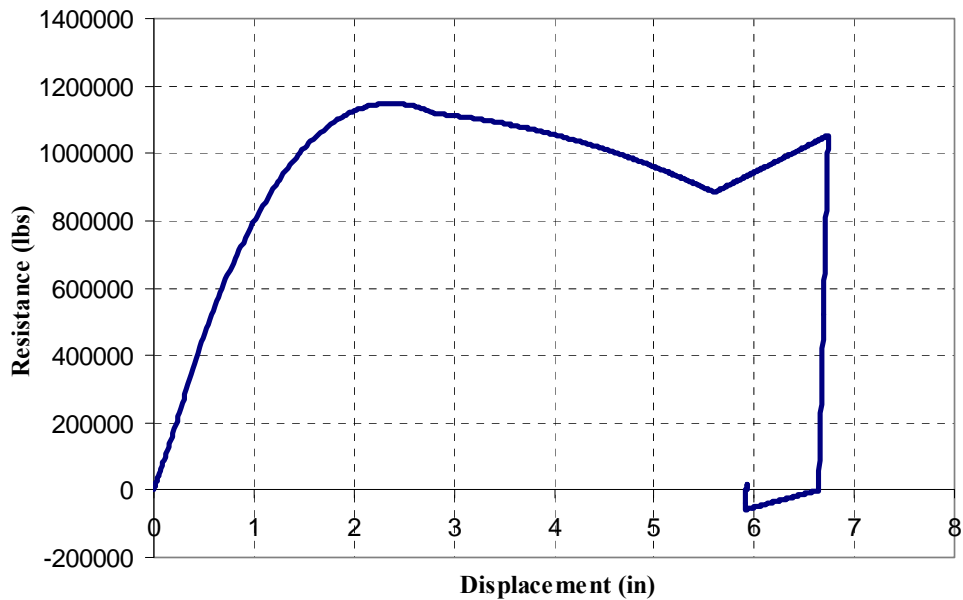


Figure 4-15. FH3 flexural resistance function.

4.2.4 Test FH4

Test FH4 was conducted in a sand backfill at a shallow depth of burial (DOB) equal to 20% of the short clean span. The reinforced concrete box had wall, floor and roof thickness of 5.6 inches, giving the roof slab a span to effective depth ratio of 10. The structure had one percent principal reinforcing steel in each face, with a concrete strength of 6700psi. The test charge density was 0.9 lb/ft³ and produced a peak pressure of 3000psi.

After excavation, post test examination indicated that the structure suffered severe damage with the roof slab on the verge of collapse. The measured permanent center deflection was about 12.5 inches. Passive deflection gage recorded a maximum transient deflection of about 13.5 inches, indicating a rebound of about 1 inch after removal of load. About 6 feet along one edge of the roof slab had failed along a vertical failure surface directly over the supporting wall and the steel reinforcement were necked down and broken. On the inside of the roof, much of the

concrete were spalled off and cracks went through the slab in some locations. A photograph of the damaged box structure after excavation is shown in Figure 4-16.

The displacement time history and resistance function for both the flexural and direct shear degree-of-freedom are plotted in Figure 4-17, 4-18, 4-19 and 4-20. The numerical results show that the roof slab did not fail in direct shear mode, same as the experimental observation. The numerical results for flexure show that the permanent displacement at the center of the roof slab is about 11.4 inch, which compares reasonably well with the experimental result. The numerical analysis also indicated that the slab underwent extensive flexural deformation into the tensile membrane region, very close to the calculated failure point at about 14.6 inches of deformation. The numerical prediction is consistent with the experiment observation.

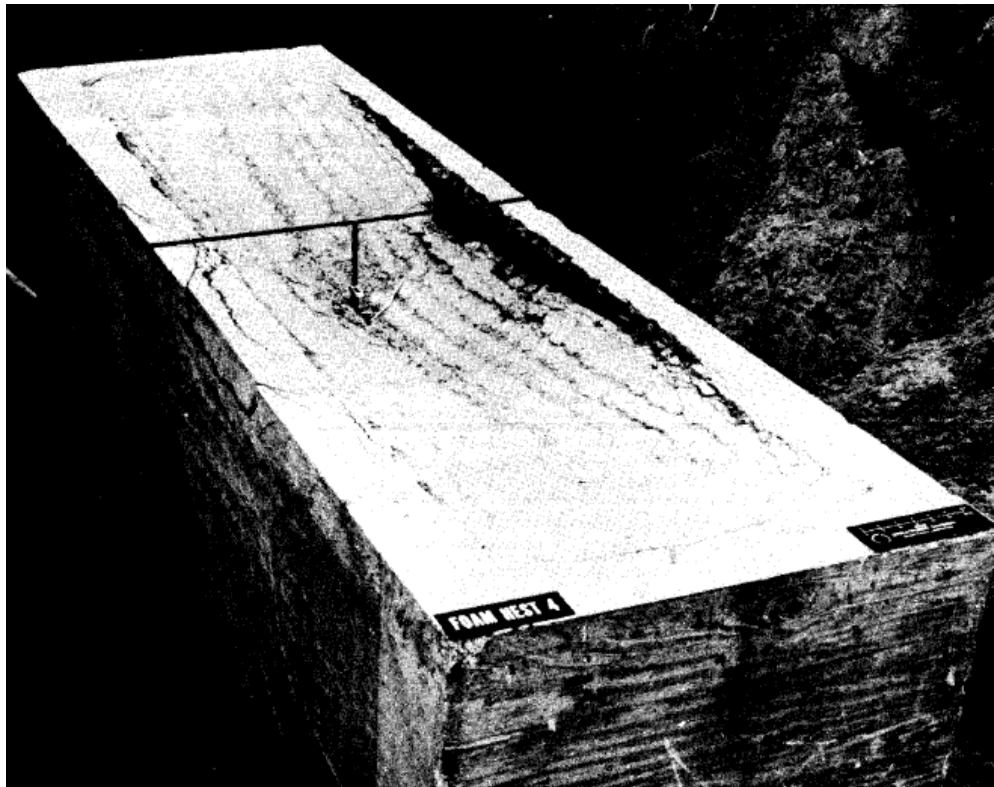


Figure 4-16. Post test view of FH4.

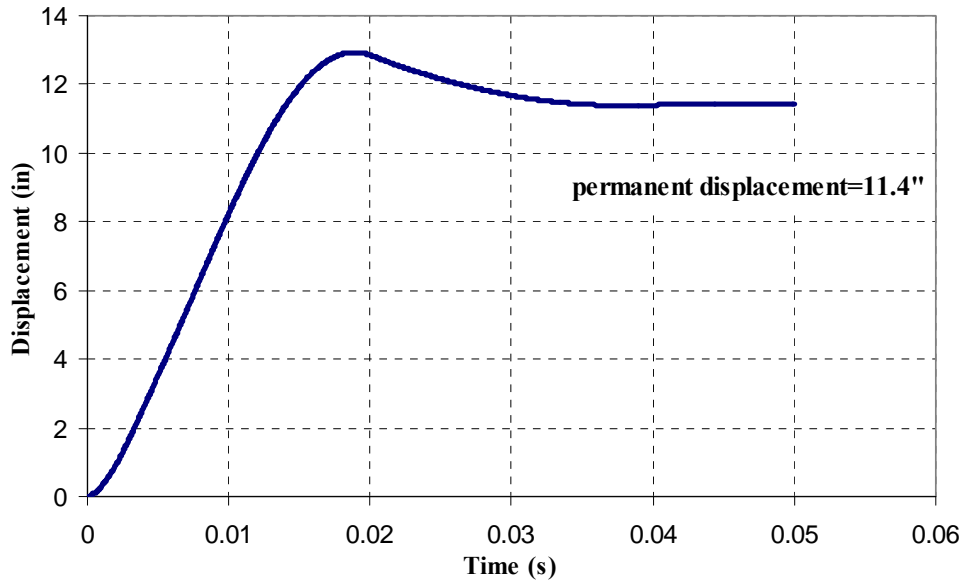


Figure 4-17. FH4 flexural displacement time history.

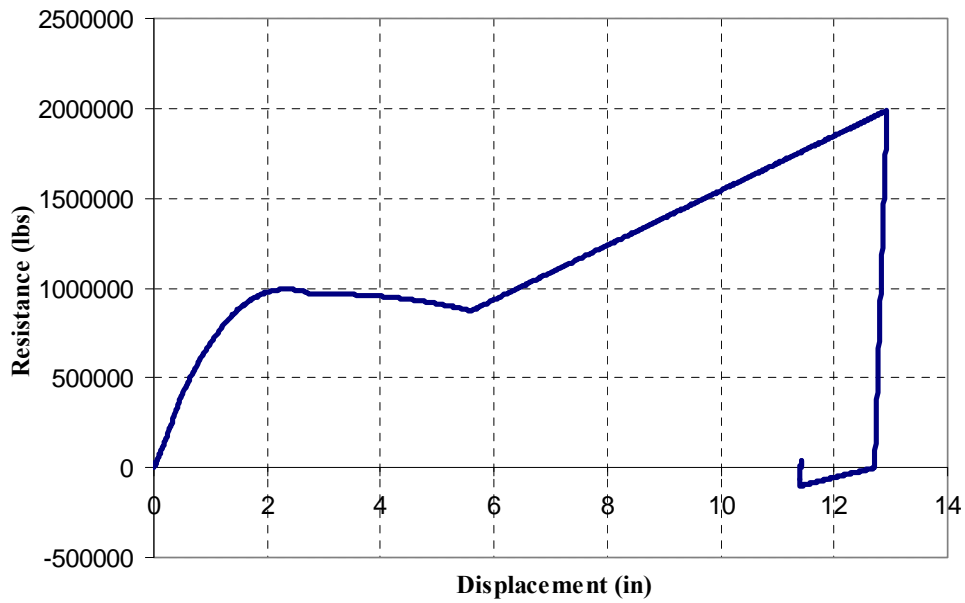


Figure 4-18. FH4 flexural resistance function.

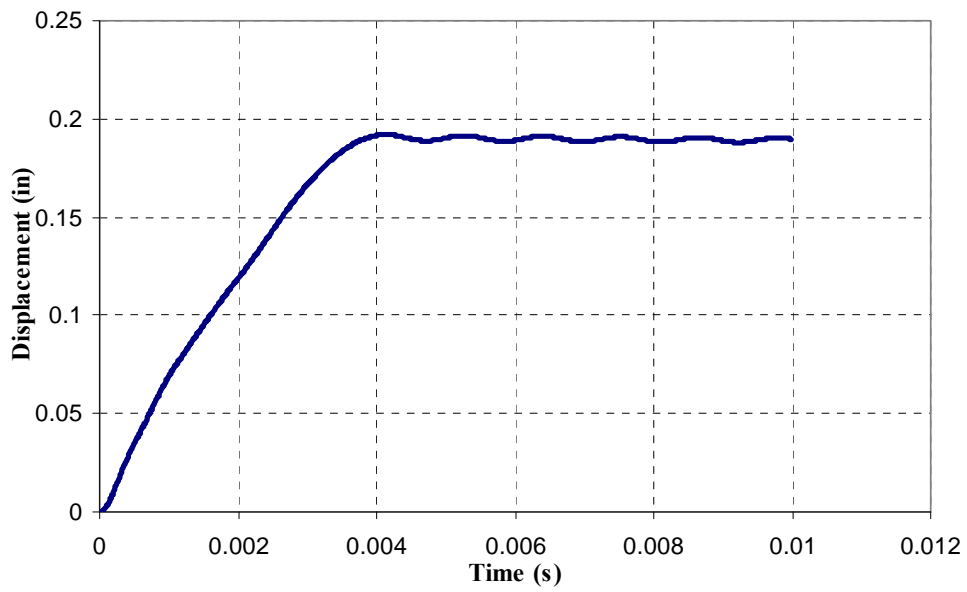


Figure 4-19. FH4 direct shear displacement time history.

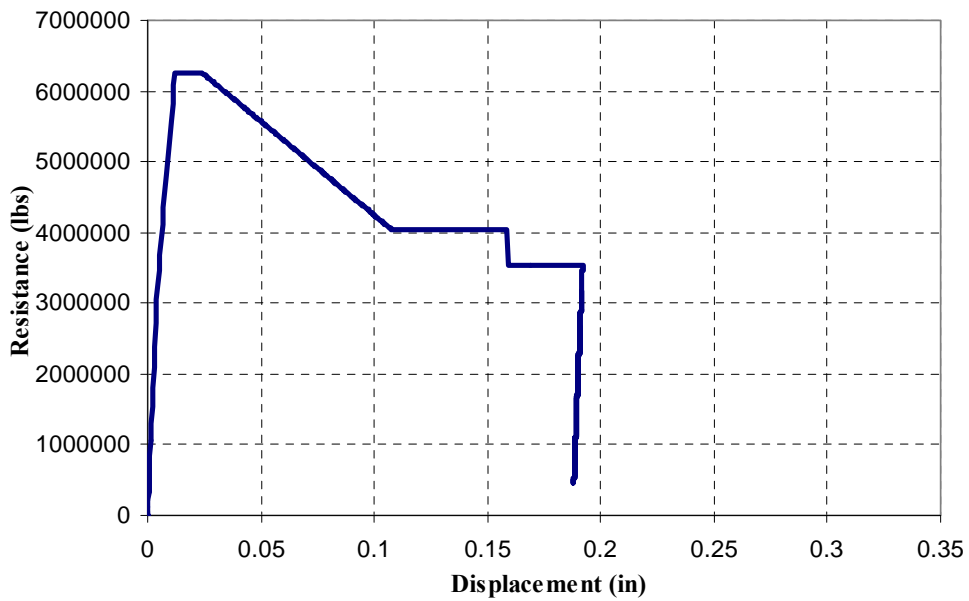


Figure 4-20. FH4 direct shear resistance function.

4.2.5 Test FH5

Test FH5 was conducted in a sand backfill at a shallow depth of burial (DOB) equal to 20% of the short clean span. The reinforced concrete box had wall, floor and roof thickness of 13.5 inches, giving the roof slab had a span to effective depth ratio of 4. The structure had 1.5 percent principal reinforcing steel in each face, with a concrete strength of 6000psi. The test charge density was 3.6 lb/ft³ and produced a peak pressure of 18,000psi.

Post test observation indicated that the sand backfill area above the buried structure was slightly depressed, with the sand backfill being sheared and making an outline of the structure perimeter. After excavation, it was observed that the structure suffered moderate damage with a permanent deflection of about 3.1 inches at the roof center. The roof slab was found to have failed in shear, with the cracked and deformed area near the supporting side walls. The center area is relatively flat. On the inside of the roof, the concrete had severely spalled off and the reinforcing bars were bent near the edges indicating a shear deflection. A photograph of the damaged box structure after excavation is shown in Figure 4-21.

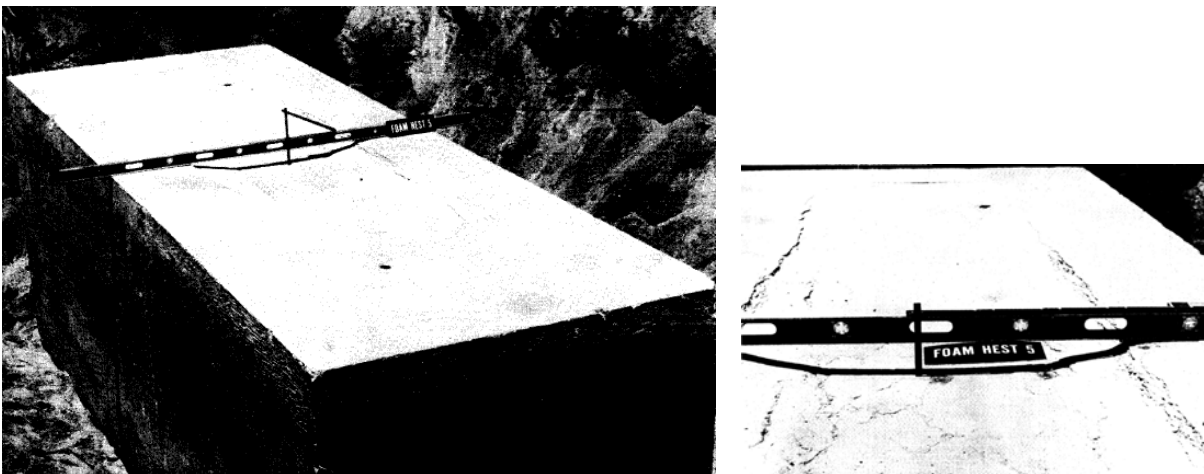


Figure 4-21. Post test view of FH5.

The displacement time history and resistance function for the direct shear degree-of-freedom are plotted in Figure 4-22 and 4-23. The numerical results show that the roof slab did not fail in direct shear mode, same as the experimental observation.

For the flexural response, the predicted displacement at the center of the roof slab center is about 0.71 inch (see Figure 4-24), which is much smaller than deflection measured in the experiment. The roof is a deep slab with a span to effective depth ratio of 4, therefore the slab is very stiff in the flexural response mode. However, based on the post test observation, the failure mode is in shear rather than flexure. Therefore it is not surprising that the numerical prediction and experimental data did not match up.

To overcome this shortcoming, a simplified approach to include the shear effect into the flexural resistance function was presented in Section 3.5. The new displacement time history and resistance function are plotted in Figure 4-25 and 4-26. The revised maximum permanent deflection at the center of the roof slab is calculated to be about 3.4 inches, and the resistance function shows that the slab had failed in shear before the slab could reach its maximum flexural capacity in the compression membrane mode. After failing in shear, the slab continues to deflect under load until the applied loading completed and the slab response reached equilibrium. With the proposed modification to the flexure resistance function to consider shear strength effect, the numerical prediction compares very well with experiment measurement and is consistent with the experiment observation.

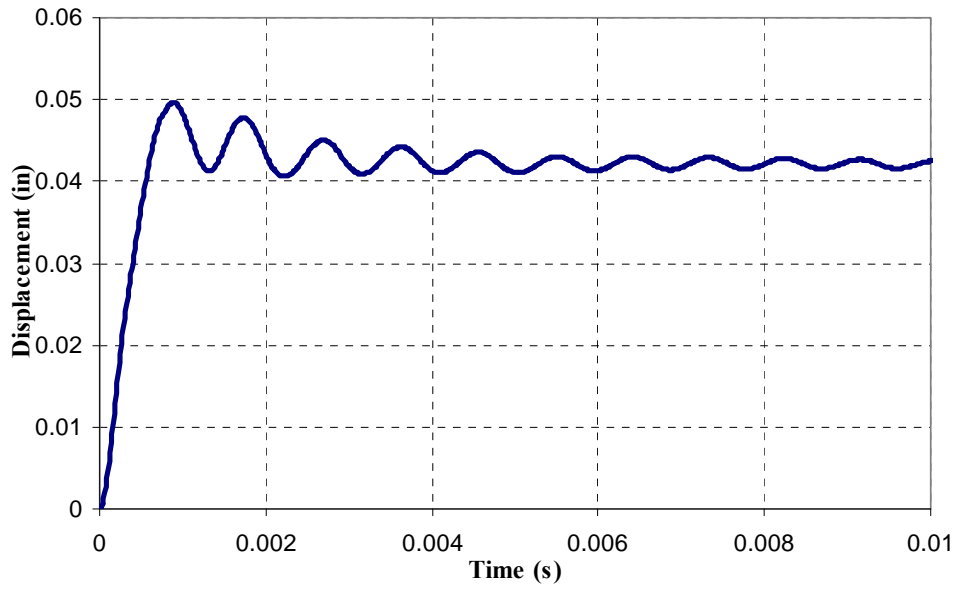


Figure 4-22. FH5 direct shear displacement time history.

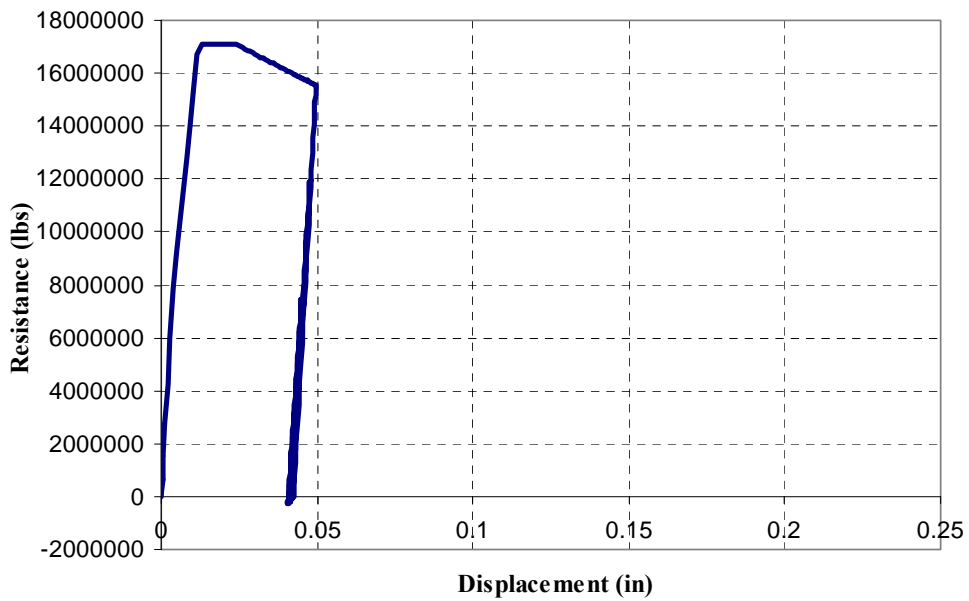


Figure 4-23. FH5 direct shear resistance function.

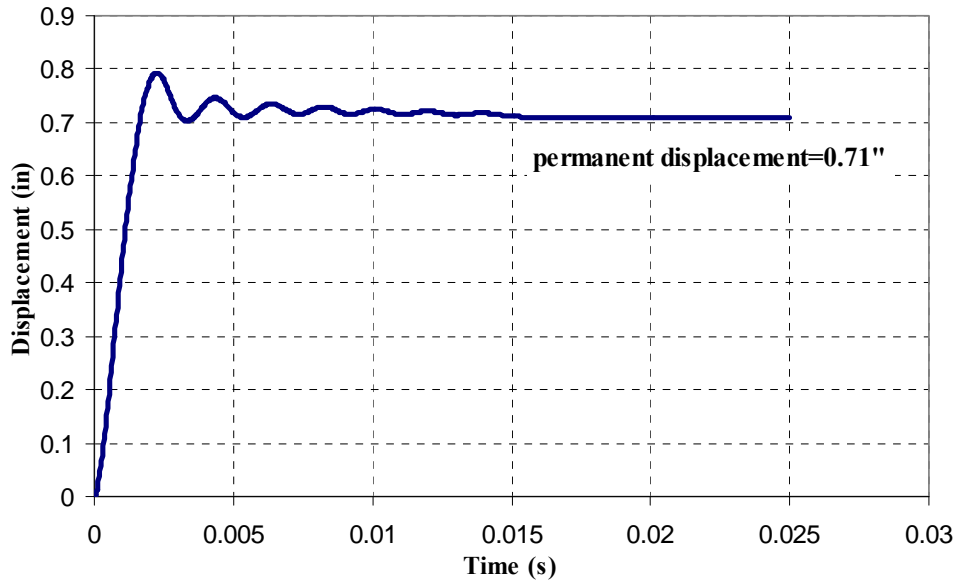


Figure 4-24. FH5 flexural displacement time history.

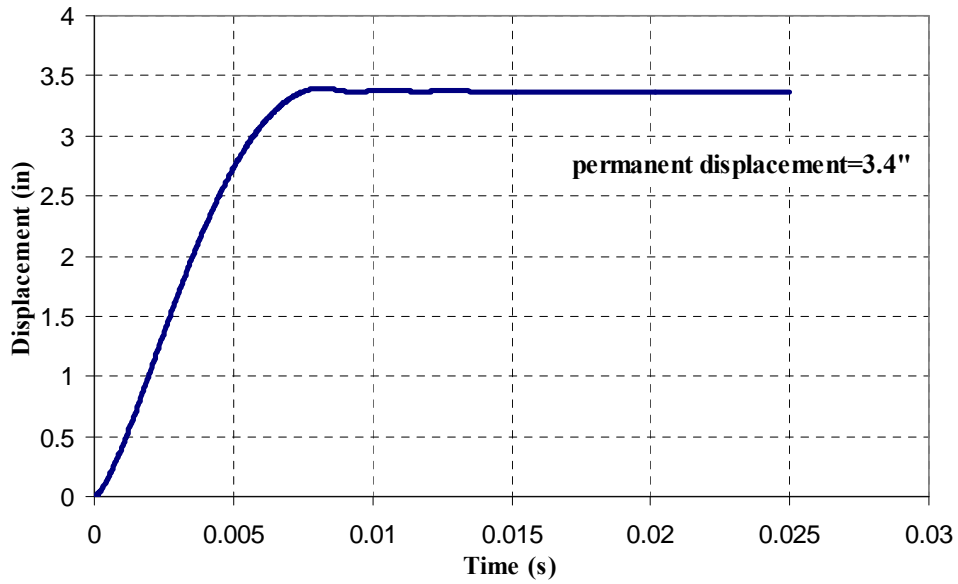


Figure 4-25. FH5 displacement time history.

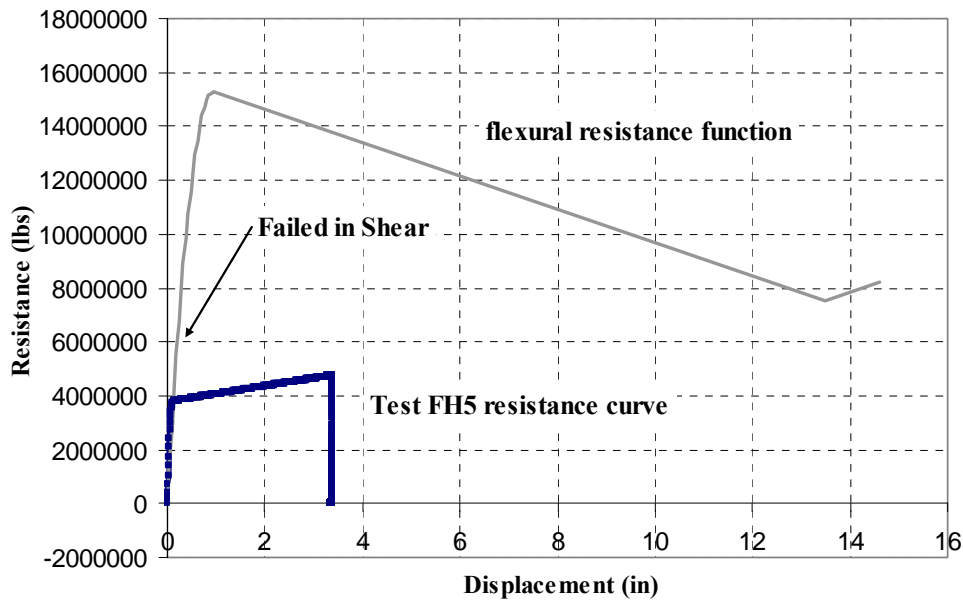


Figure 4-26. FH5 resistance function.

4.2.6 Test FH6

Test FH6 was conducted in a clay backfill at a depth of burial (DOB) equal to 50% of the short clean span. The reinforced concrete box had wall, floor and roof thickness of 5.6 inches, giving the roof slab had a span to effective depth ratio of 10. The structure had one percent principal reinforcing steel in each face, with a concrete strength of 6800psi. The test charge density was 1.8 lb/ft³ and produced a peak pressure of 8,320psi.

A photograph of the box slab after partial excavated is shown in Figure 4-27. Severe structural damage occurred and the roof collapsed completely. The lateral earth pressure pushed the side walls inward after roof collapse.

The numerical results show that the roof slab failed in both direct shear mode and flexural mode. When the applied loading exceeded the direct shear resistance of the entire slab, the slab will shear off the wall support and the failure occurs at about 1 millisecond after the arrival of the loading. The numerical prediction is therefore consistent with the experiment observation. The

displacement time history and resistance function for both the flexural and direct shear degree-of-freedom are plotted in Figure 4-28, 4-29, 4-30 and 4-31.



Figure 4-27. Post test view of FH6.

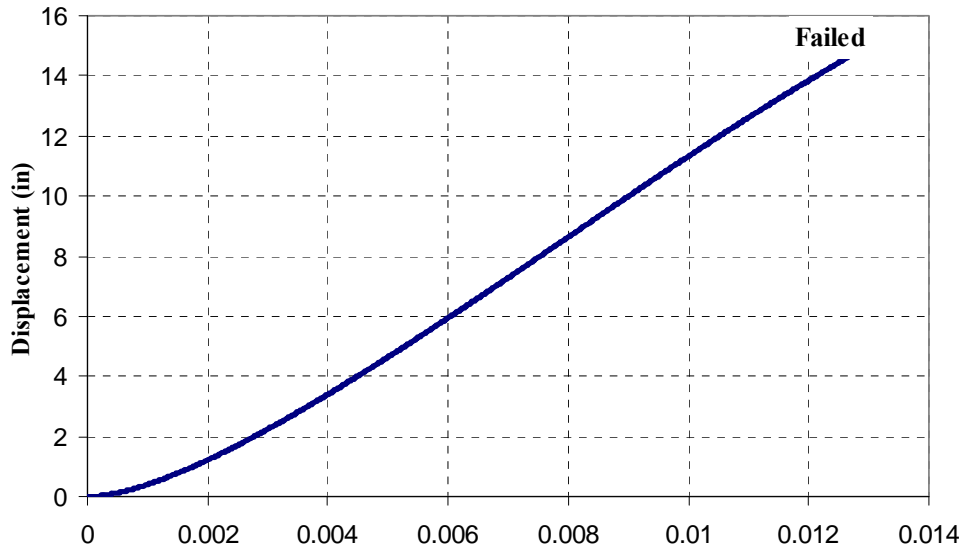


Figure 4-28. FH6 flexural displacement time history.

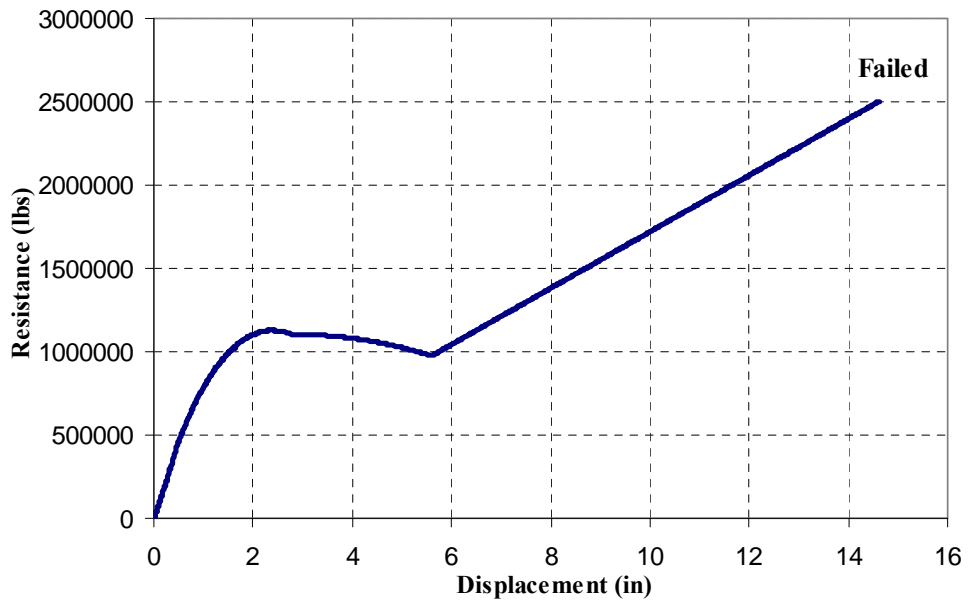


Figure 4-29. FH6 flexural resistance function.

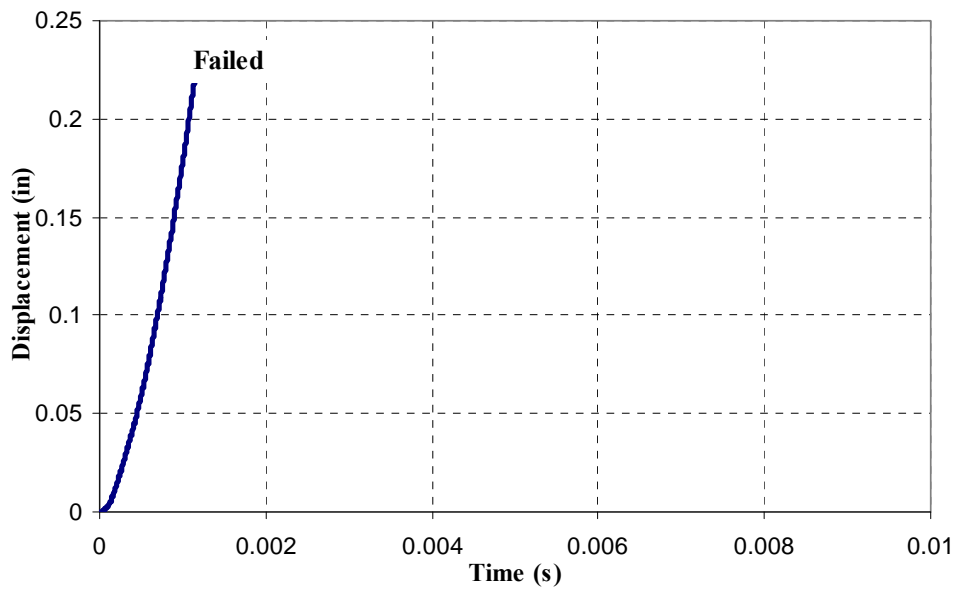


Figure 4-30. FH6 direct shear displacement time history.

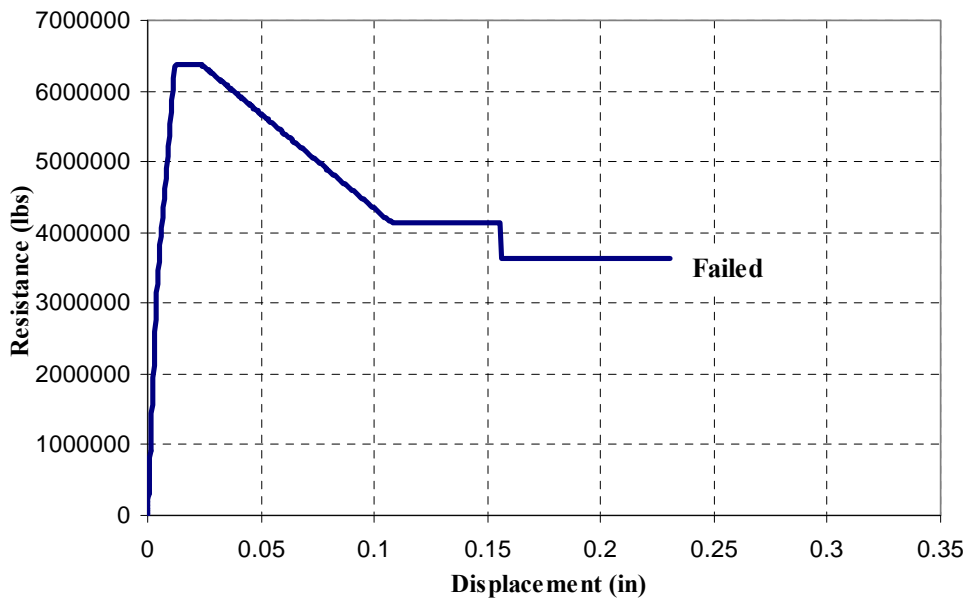


Figure 4-31. FH6 direct shear resistance function.

4.2.7 Summary

A summary of all the six tests present in the above sections is presented in Table 4-1.

Table 4-1. Summary of results

Test No.	Experiment Structural Behavior / Failure Mode	Average Peak Pressure (psi)	Measured Permanent Deflection (in) Δ_1	Numerical Structural Behavior / Failure Mode	Computed Permanent Deflection (in) Δ_2	$\frac{\Delta_2}{\Delta_1}$	Failure Direct Shear Slip (in)	Time of Failure (msec)
FH1	Flexure	2400	0.44	Flexure	0.50	1.14	--	--
FH2	Direct Shear	5200	Collapsed	Direct Shear	Collapsed	1.00	0.20	1.1
FH3	Flexure	2650	6	Flexure	5.9	0.98	--	--
FH4	Flexure	3000	12.5	Flexure	11.4	0.91	--	--
FH5	Shear	18000	3.1	Flexure / Shear	3.4	1.09	--	--
FH6	Direct Shear	8320	Collapsed	Direct Shear	Collapsed	1.00	0.23	1.2

4.3 Assessment by P-I Diagrams

For all the test cases presented in Section 4.2, Pressure-Impulse (P-I) diagrams were generated. The experiment measured pressure and corresponding impulse value was plotted on the same P-I graph. The assessment of the structural response using the P-I diagram were compared with the post test observations. The P-I diagrams are shown in Figure 4-32 to 4-37.

For tests FH1, FH3, FH4 and FH5, the experimental pressure-impulse point lies on the left side of both the flexure and direct shear mode threshold curve, and this agrees with the observations of the experiment whereby the structure did not suffer any complete failure.

For test FH2 and FH6, experiment observations indicated that the roof slab suffered completed failure in the test. The same result is obtained from the assessment using P-I diagram whereby the experiment pressure-impulse data point lies on the right side of the threshold curves.

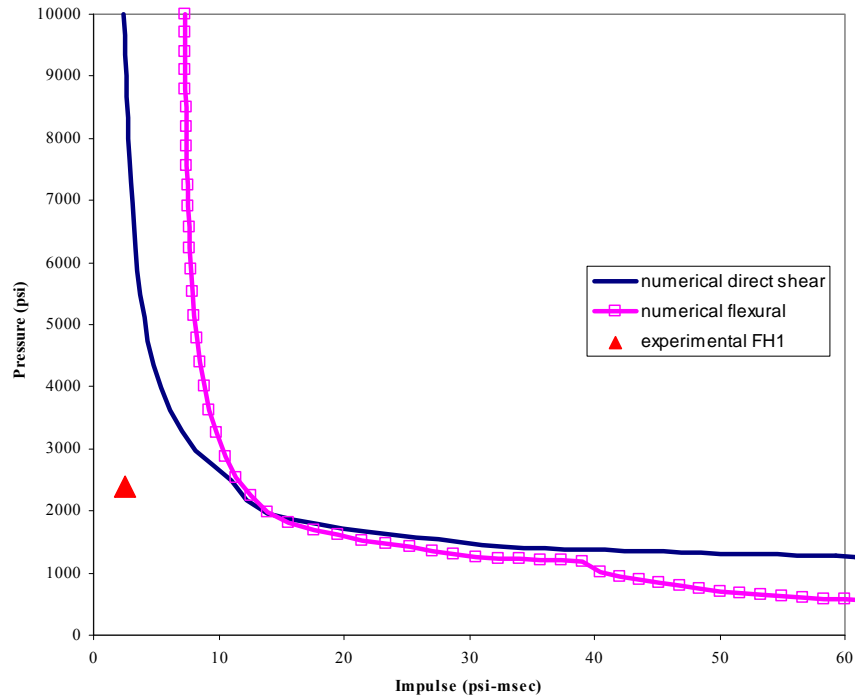


Figure 4-32. FH1 Pressure-Impulse diagram.

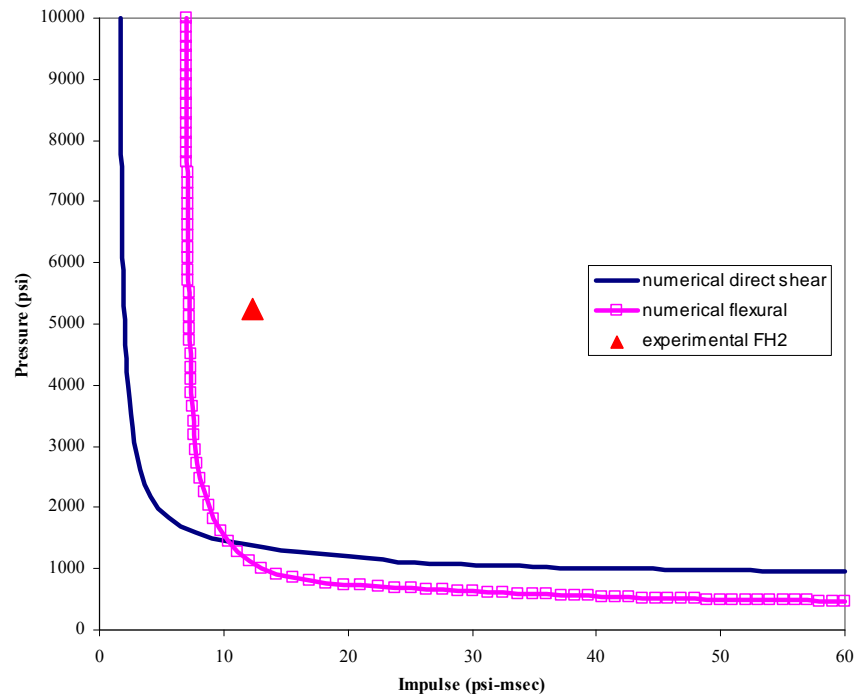


Figure 4-33. FH2 Pressure-Impulse diagram.

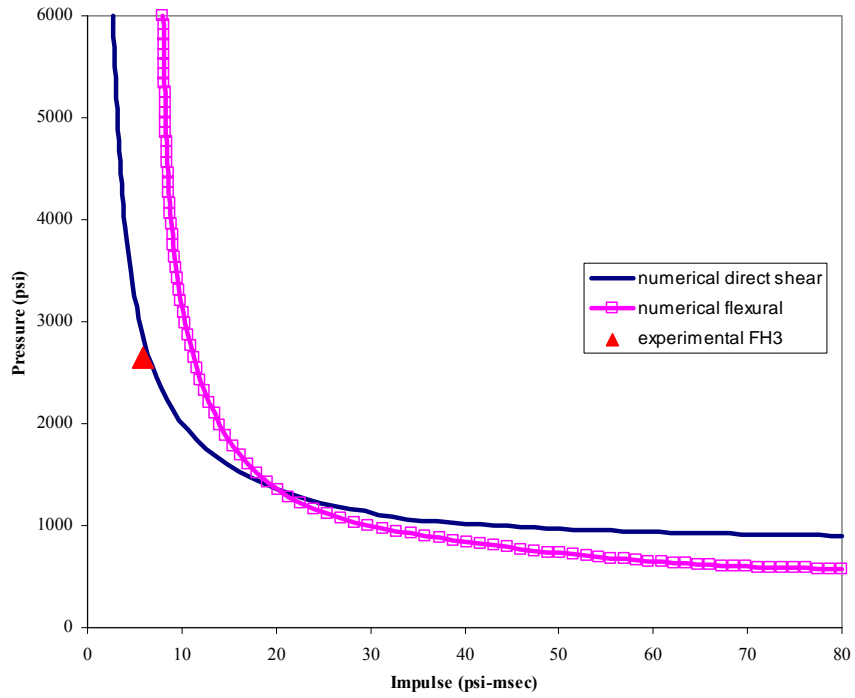


Figure 4-34. FH3 Pressure-Impulse diagram.

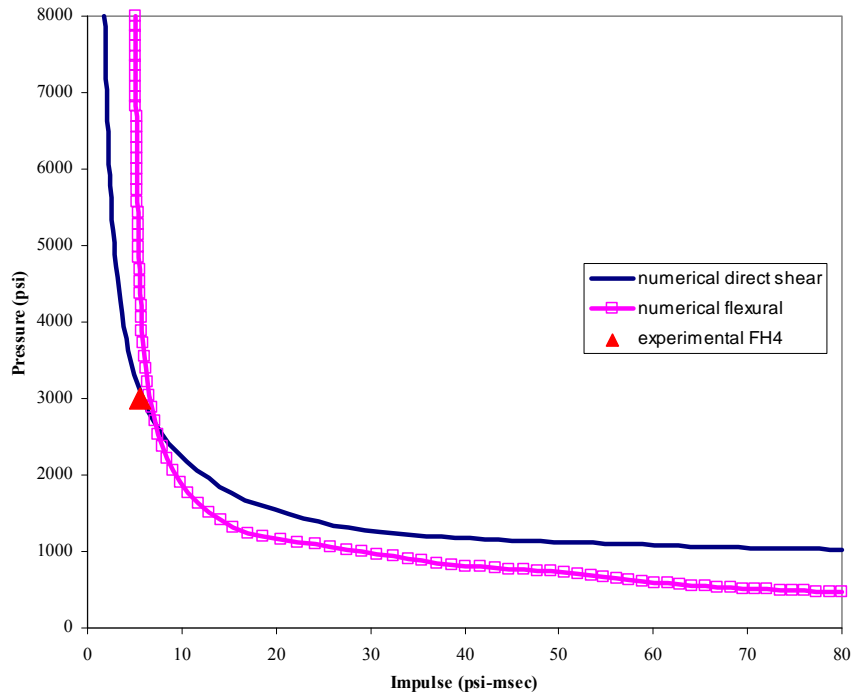


Figure 4-35. FH4 Pressure-Impulse diagram.

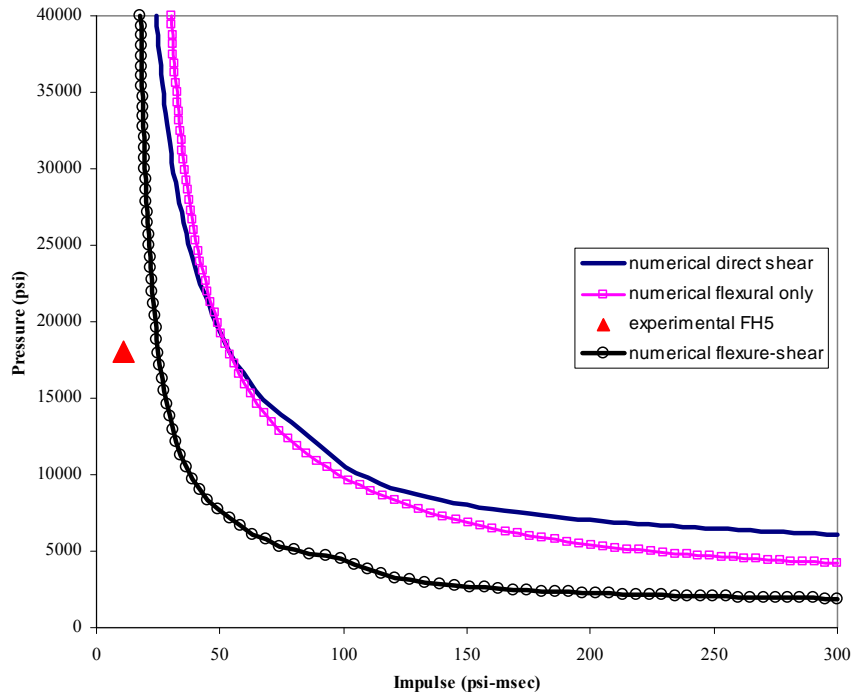


Figure 4-36. FH5 Pressure-Impulse diagram.

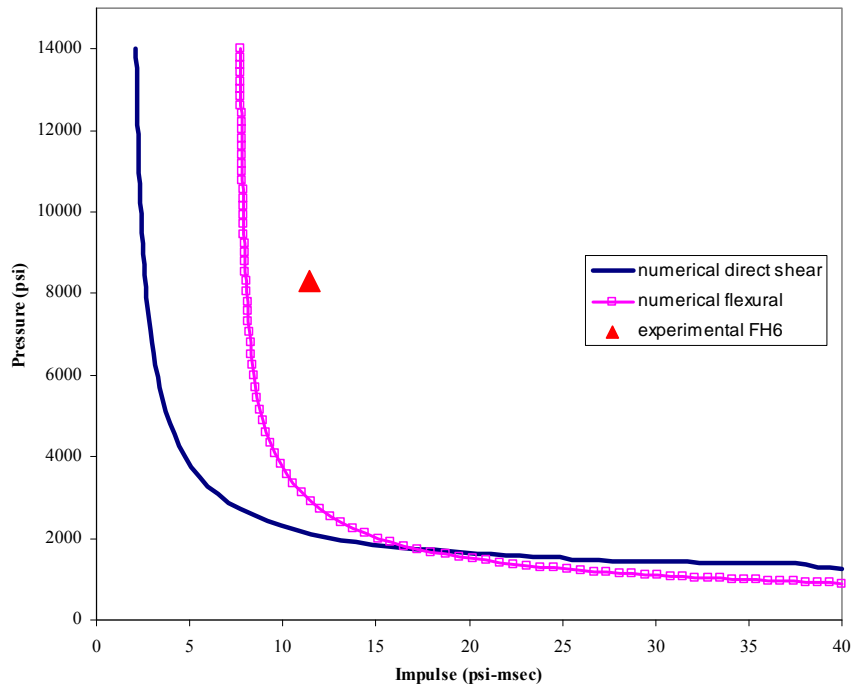


Figure 4-37. FH6 Pressure-Impulse diagram.

4.4 Summary

Based on the numerical approach presented in Chapter 3, the dynamic response for buried box structures are generated and the numerical results compared very well with the experimental data. The approach also correctly predicted the correct mode of failure by examining the response time history and resistance functions. Pressure-Impulse diagrams are also generated for all the test cases considered. The assessment of structure behavior using P-I diagram also predicted the correct result when compared with experiment data.

CHAPTER 5 CONCLUSIONS AND RECOMMENDATIONS

5.1 Summary

A numerical method for the dynamic analysis of shallow-buried reinforced concrete box-type structures subjected to air blast loadings was presented in this study. The proposed method adopted the Single-Degree-of-Freedom (SDOF) approach, where two loosely coupled SDOF systems were considered to model the flexural and direct shear mode of structural response.

An introduction to blast loads and the effects on buried structures was presented in Chapter 2. Dynamic structural behavior and analysis for real continuous system and the approximation into an equivalent SDOF system was reviewed. A review on the structural response mode for reinforced concrete slabs and the resistance model under static and dynamic loading as well as the background and applications of pressure-impulse diagrams was presented.

The proposed methodology to generate the resistance functions for reinforced concrete slabs of the buried box structure in both the flexural mode and direct shear mode was presented in Chapter 3. The issue of soil arching and the required modifications to the load and mass factors for the equivalent SDOF system was also discussed and incorporated into the proposed methodology. For the consideration of deep slab behavior, the flexural resistance function was incorporated with a modification to capture the possibility of shear failure in the slab.

The proposed procedure was implemented in a computer programming language and the results were validated using experimental data from a number of explosive tests on buried reinforced concrete boxes. The numerical results compared very well with experimental data.

5.2 Conclusions

Based on the results from this present study, the following conclusions can be drawn.

- The proposed methodology can be employed for the approximate analyses of reinforced concrete slabs, and structural systems that are composed of such elements.

- Single-degree-of-freedom analyses which are based on rational models for structural behavior mechanism have been validated, with good accuracy and consistency.
- The use of pressure-impulse diagram enables a quick and accurate assessment of the likely performance of the structure, by comparison of the location of the pressure and impulse point with respect to the flexural and direct shear threshold curves plotted on the P-I diagram.
- The proposed variation of the load and mass transformation factors for SDOF system enable a closer match of the factors with respect to the actual response regime of the structure under different loading combination.
- Dynamic soil arching effect reduced the load acting on the buried roof slab and changed the load distribution. The load and mass transformation factors must be modified with an appropriate reduction factor in order to reflect the soil arching effect and to obtain an accurate numerical result.
- Shear failure on the slab was not captured with the original proposed flexural and direct shear mode SDOF systems. A simplified approach to consider shear failure on the flexural resistance function was able to better model behavior for slab which failed in shear.

5.3 Recommendations for Future Study

Based on the results and observations, the following recommendations for future research are proposed.

- The current methodology assumed that the loading on the slab is assumed to be a uniformly distributed airblast load on the soil surface. Further consideration of non-uniform loads that may be caused by localized HE (high explosives) explosions is recommended.
- Direct shear mode of response was based on the Hawkins model and a single enhancement factor is applied to account for the effects of compression and rate effects. A detailed study of the significance of the possible variation of the enhancement factor is recommended.
- Shear failure mode is only considered in this study in a simplified way. A separate response model for tension shear may be considered and its significance can be studied in greater detail.
- To study the possible interaction between the roof, wall and floor elements and their effects on the structural response of the box structure under blast loads.

APPENDIX

EXPERIMENT TEST ON SHALLOW BURIED FLAT ROOF STRUCTURES

The series of experiment tests carried out by the United States Army Engineer Waterways Experiment Station, Structures Laboratory (Kiger and Getchell 1980) are used in Chapter 4 as validation data. The details of the experiment carried out are given in this appendix.

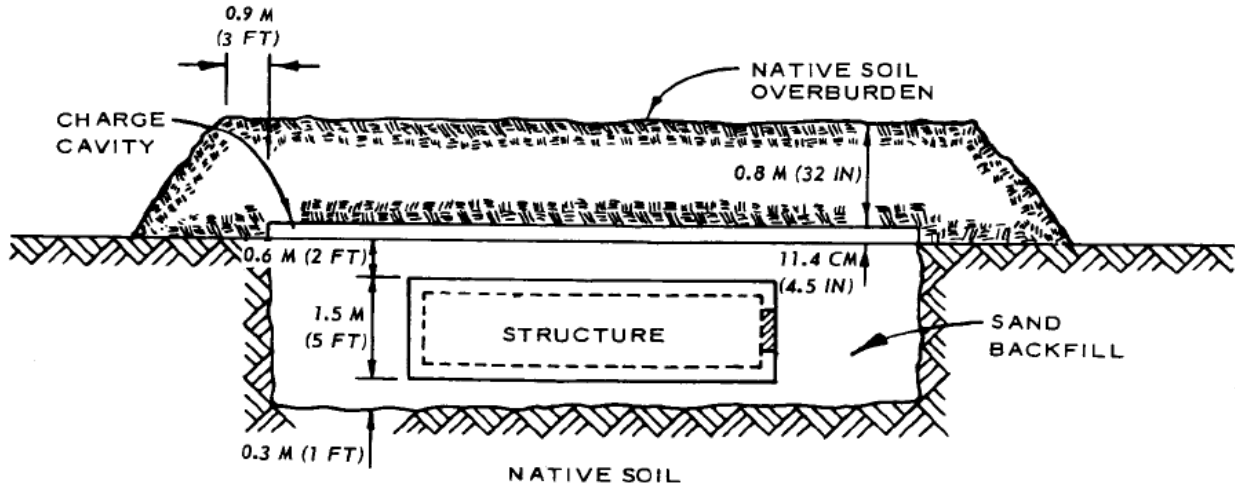
The tests were carried out to obtain structural response data in a simulated nuclear overpressure environment at the severe damage level for a buried reinforced concrete structure. Six quarter-scale models of rectangular, single bay reinforced concrete box structures with inside dimensions of 4 feet high, 4 feet wide and 16 feet long, were tested with simulated nuclear blast. The box structures were designed to model one bay from a rectangular multi-bay structure with span to effective depth ratios of between 4 and 10.

The box structure was tested in a shallow-buried configuration using a HEST (High Explosive Simulation Technique) test which can simulate the peak pressure and duration characteristic of the overpressure generated in a nuclear detonation. The charge cavity was composed of conventional high explosives and plastic foam for which the tests were designated Foam Hest (FH). The test involves distributing a high explosive over a relatively large surface area and covering the explosive with a soil overburden to momentarily confine the blast. The test configuration for FH3 is shown in Figure A-1.

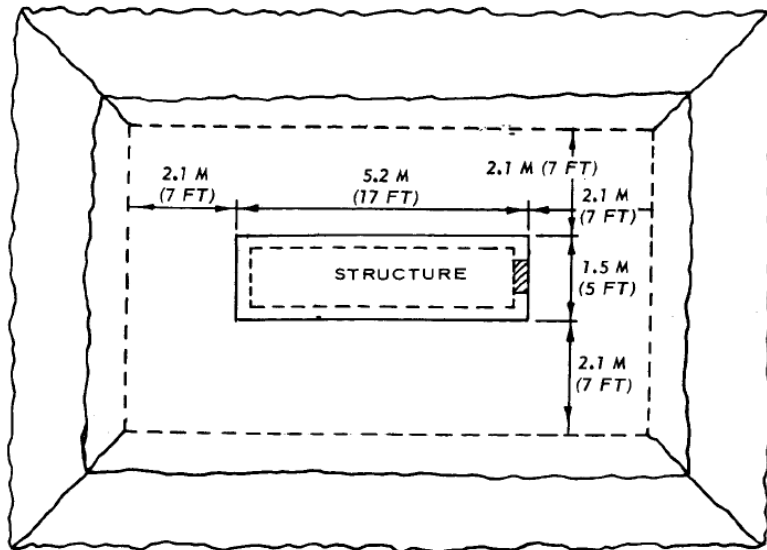
The material properties such as the concrete and steel strength, steel ratio and charge density were varied for all the six tests. The depth of burial for the tests was varied, with a ratio of depth of burial to the short clear span between 0.2 to 0.5. The parameters of the six cases presented in Chapter 4 are tabulated in Table A-1.

Construction details for FH1 and FH5 are shown in Figure A-2 and Figure A-3 respectively.

Parameters used in the numerical procedure are summarized in Table A-2, A-3, A-4, A-5, A-6 and A-7.



A



B

Figure A-1. Experiment test configuration for FH3. A) Elevation. B) Plan view.

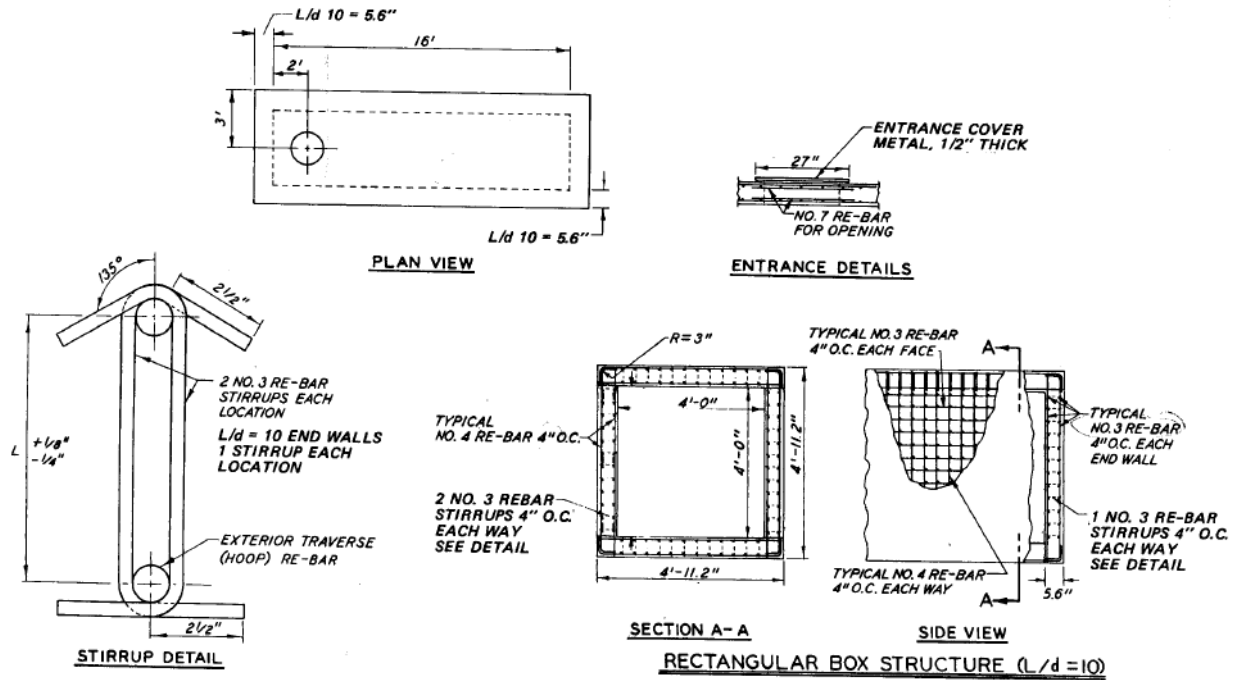


Figure A-2. Construction dimensions and details of FH1.

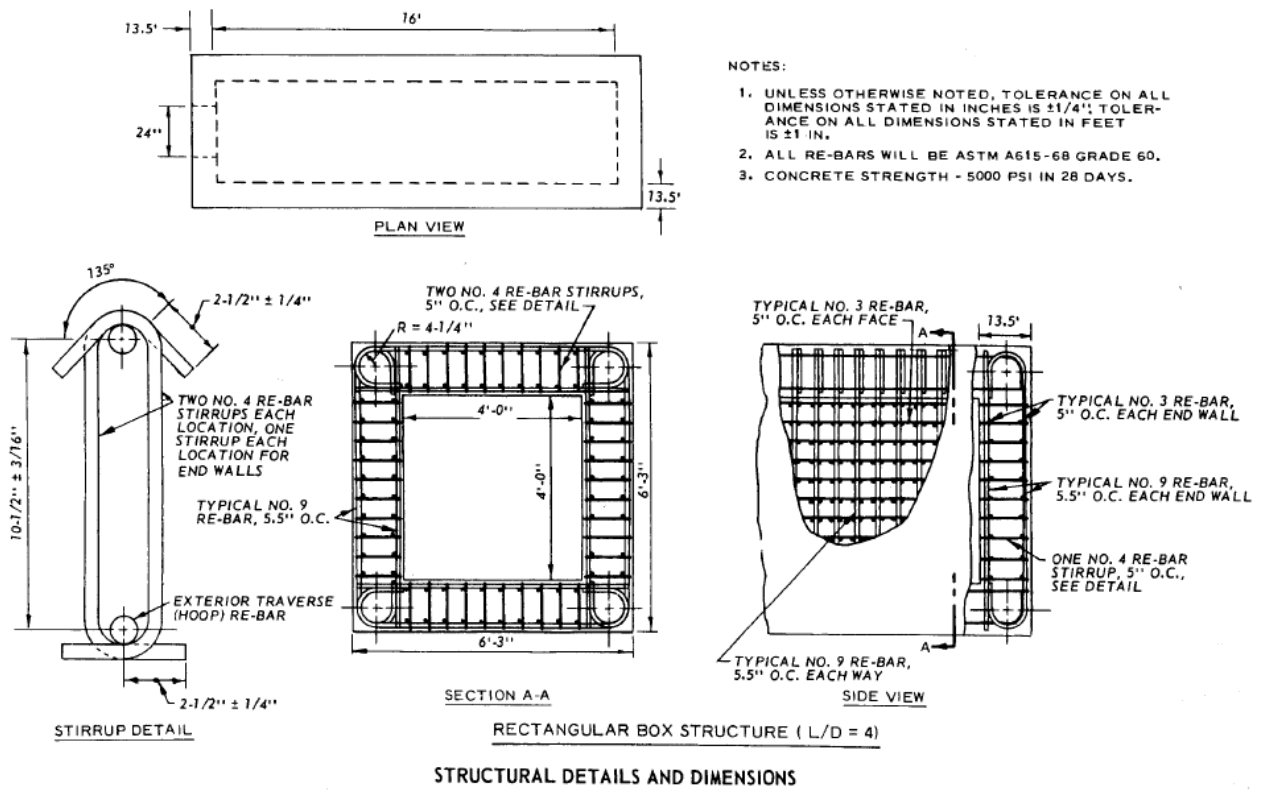


Figure A-3. Construction dimensions and details of FH5.

Table A-1. Parameters for FoamHest tests

Parameters	FH1	FH2	FH3	FH4	FH5	FH6
Height (ft)	4	4	4	4	4	4
Ls (ft)	4	4	4	4	4	4
L _L (ft)	16	16	16	16	16	16
Thickness (in)	5.6	5.6	5.6	5.6	13.5	5.6
Span-effective depth ratio	10	10	10	10	4	10
DOB (ft)	2	2	2	0.8	0.8	2
DOB-Ls ratio	0.5	0.5	0.5	0.2	0.2	0.2
Concrete strength (psi)	7000	7600	7900	6700	6000	6800
Fy (psi)	75,000	57,000	57,000	65,000	69,000	65,000
Percentage steel (%)	1	1	1	1	1.5	1
Soil Type	Sand	Sand	Clay	Sand	Sand	Clay
Charge density (pcf)	0.9	2.7	0.9	0.9	3.6	1.8

Table A-2. Test FH1 input parameters

Parameters	Value
Height	4 ft
L_x	16 ft
L_y	4 ft
Slab Thickness	5.6 in
Concrete cylinder strength	7000 psi
Concrete density	0.0868 lb/in ³
X-direction	
Reinforcement area	0.11 in ² / 4 in spacing
Reinforcement bar diameter	0.375
Reinforcement yield strength	75,000 psi
Reinforcement ultimate strain	0.21
Depth of top reinforcement	0.8 in
Depth of top reinforcement	4.8 in
Y-direction	
Reinforcement area	0.20 in ² / 4 in spacing
Reinforcement bar diameter	0.50
Reinforcement yield strength	75,000 psi
Reinforcement ultimate strain	0.21
Depth of top reinforcement	0.8 in
Depth of top reinforcement	4.8 in
Depth of burial (ft)	2
Soil Type	Sand
Soil density (pci)	0.061
Friction angle ϕ	35.5
Coefficient of static lateral earth pressure K_o	0.5
Soil wave velocity (in/s)	18,000
Damping (Flexure / Direct shear)	20% / 5%

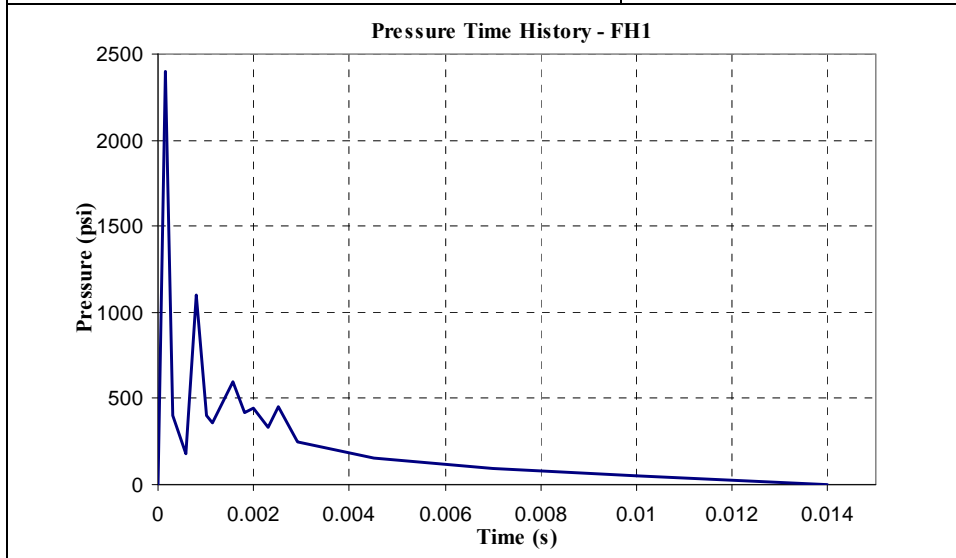


Table A-3. Test FH2 input parameters

Parameters	Value
Height	4 ft
L_x	16 ft
L_y	4 ft
Slab Thickness	5.6 in
Concrete cylinder strength	7600 psi
Concrete density	0.0868 lb/in ³
X-direction	
Reinforcement area	0.11 in ² / 4 in spacing
Reinforcement bar diameter	0.375
Reinforcement yield strength	57,000 psi
Reinforcement ultimate strain	0.21
Depth of top reinforcement	0.8 in
Depth of top reinforcement	4.8 in
Y-direction	
Reinforcement area	0.20 in ² / 4 in spacing
Reinforcement bar diameter	0.50
Reinforcement yield strength	57,000 psi
Reinforcement ultimate strain	0.21
Depth of top reinforcement	0.8 in
Depth of top reinforcement	4.8 in
Depth of burial (ft)	2
Soil Type	Sand
Soil density (pci)	0.0613
Friction angle ϕ	35.5
Coefficient of static lateral earth pressure K_o	0.5
Soil wave velocity (in/s)	18,000
Damping (Flexure / Direct shear)	20% / 5%

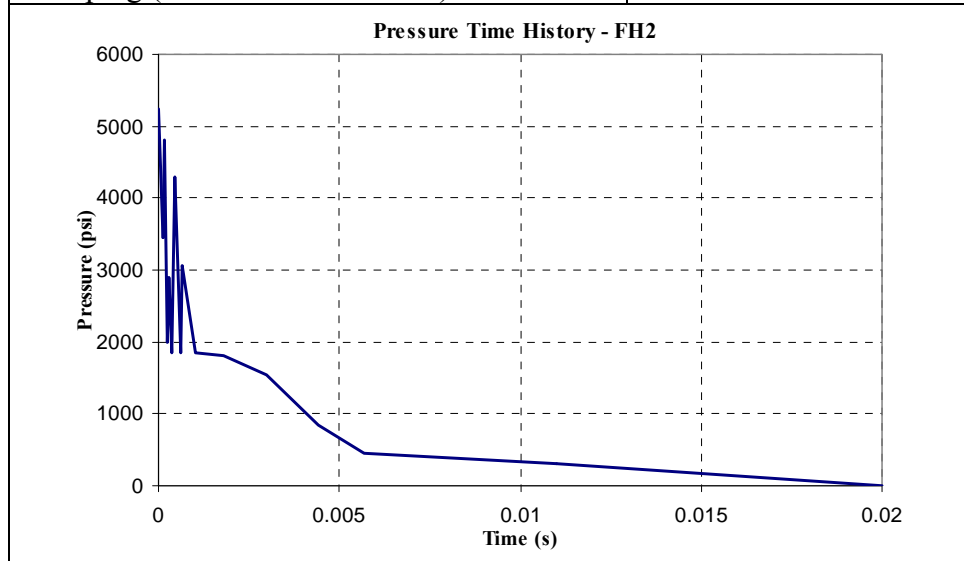


Table A-4. Test FH3 input parameters

Parameters	Value
Height	4 ft
L_x	16 ft
L_y	4 ft
Slab Thickness	5.6 in
Concrete cylinder strength	7900 psi
Concrete density	0.0868 lb/in ³
X-direction	
Reinforcement area	0.11 in ² / 4 in spacing
Reinforcement bar diameter	0.375
Reinforcement yield strength	57,000 psi
Reinforcement ultimate strain	0.21
Depth of top reinforcement	0.8 in
Depth of top reinforcement	4.8 in
Y-direction	
Reinforcement area	0.20 in ² / 4 in spacing
Reinforcement bar diameter	0.50
Reinforcement yield strength	57,000 psi
Reinforcement ultimate strain	0.21
Depth of top reinforcement	0.8 in
Depth of top reinforcement	4.8 in
Depth of burial (ft)	2
Soil Type	Clay
Soil density (pci)	0.0714
Friction angle ϕ	0
Coefficient of static lateral earth pressure K_o	1.0
Soil wave velocity (in/s)	24,000
Damping (Flexure / Direct shear)	20% / 5%

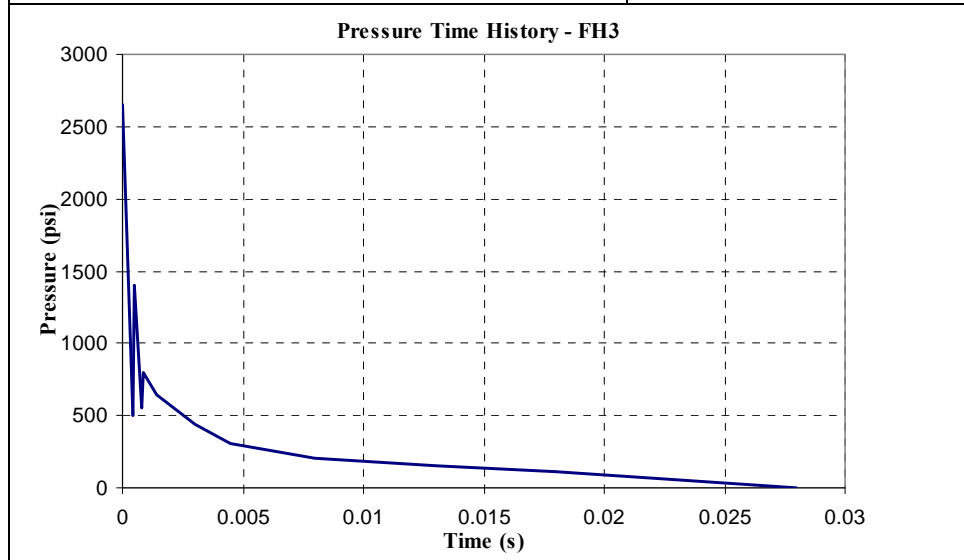


Table A-5. Test FH4 input parameters

Parameters	Value
Height	4 ft
L_x	16 ft
L_y	4 ft
Slab Thickness	5.6 in
Concrete cylinder strength	6700 psi
Concrete density	0.0868 lb/in ³
X-direction	
Reinforcement area	0.11 in ² / 4 in spacing
Reinforcement bar diameter	0.375
Reinforcement yield strength	65,000 psi
Reinforcement ultimate strain	0.21
Depth of top reinforcement	0.8 in
Depth of top reinforcement	4.8 in
Y-direction	
Reinforcement area	0.20 in ² / 4 in spacing
Reinforcement bar diameter	0.50
Reinforcement yield strength	65,000 psi
Reinforcement ultimate strain	0.21
Depth of top reinforcement	0.8 in
Depth of top reinforcement	4.8 in
Depth of burial (ft)	0.8
Soil Type	Sand
Soil density (pci)	0.0612
Friction angle ϕ	35.5
Coefficient of static lateral earth pressure K_o	0.5
Soil wave velocity (in/s)	18,000
Damping (Flexure / Direct shear)	20% / 5%

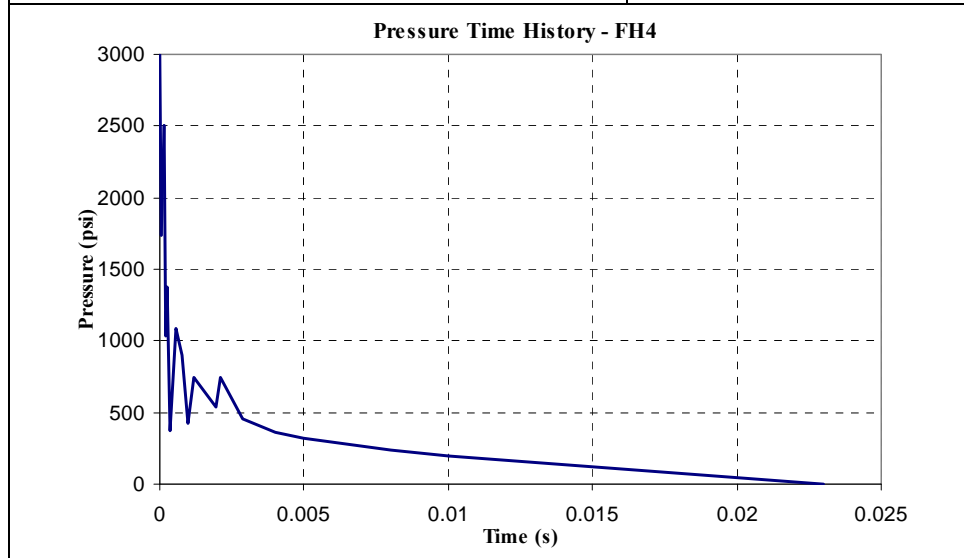


Table A-6. Test FH5 input parameters

Parameters	Value
Height	4 ft
L_x	16 ft
L_y	4 ft
Slab Thickness	13.5 in
Concrete cylinder strength	6000 psi
Concrete density	0.0868 lb/in ³
X-direction	
Reinforcement area	0.11 in ² / 5 in spacing
Reinforcement bar diameter	0.375
Reinforcement yield strength	69,000 psi
Reinforcement ultimate strain	0.21
Depth of top reinforcement	1.5 in
Depth of top reinforcement	12.0 in
Y-direction	
Reinforcement area	1.0 in ² / 5.5 in spacing
Reinforcement bar diameter	0.50
Reinforcement yield strength	69,000 psi
Reinforcement ultimate strain	0.21
Depth of top reinforcement	1.5 in
Depth of top reinforcement	12.0 in
Depth of burial (ft)	0.8
Soil Type	Sand
Soil density (pci)	0.0623
Friction angle ϕ	35.5
Coefficient of static lateral earth pressure K_o	0.5
Soil wave velocity (in/s)	18,000
Damping (Flexure / Direct shear)	20% / 5%

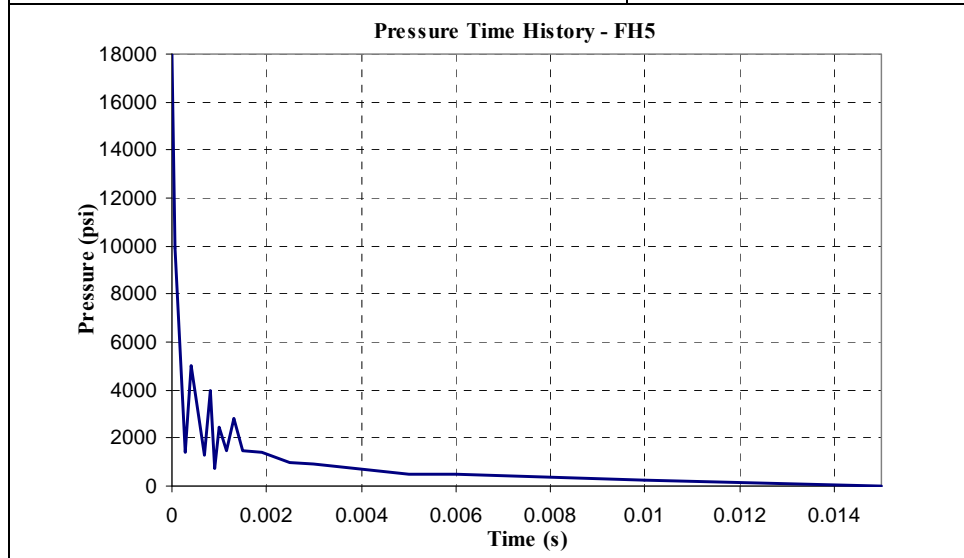
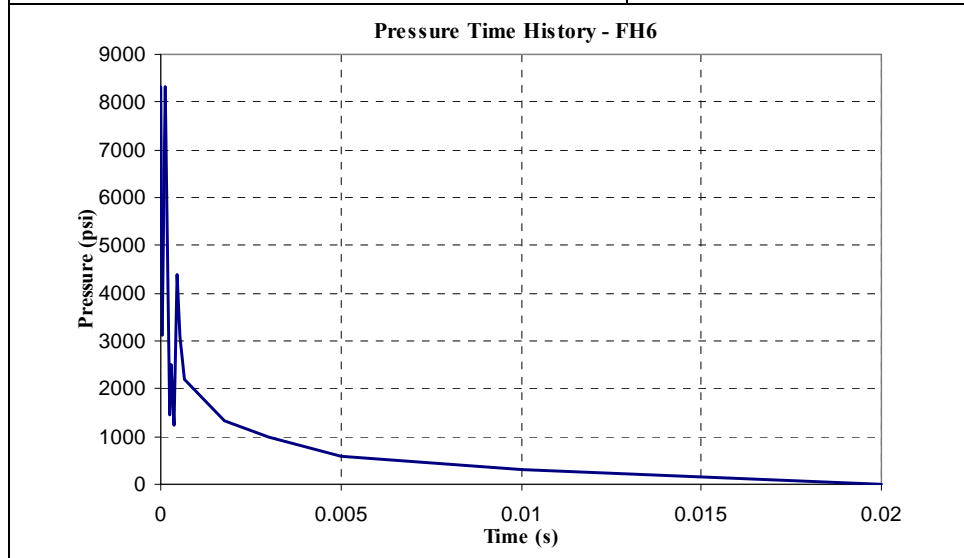


Table A-7. Test FH6 input parameters

Parameters	Value
Height	4 ft
L_x	16 ft
L_y	4 ft
Slab Thickness	5.6 in
Concrete cylinder strength	6800 psi
Concrete density	0.0868 lb/in ³
X-direction	
Reinforcement area	0.11 in ² / 4 in spacing
Reinforcement bar diameter	0.375
Reinforcement yield strength	65,000 psi
Reinforcement ultimate strain	0.21
Depth of top reinforcement	0.8 in
Depth of top reinforcement	4.8 in
Y-direction	
Reinforcement area	0.20 in ² / 4 in spacing
Reinforcement bar diameter	0.50
Reinforcement yield strength	65,000 psi
Reinforcement ultimate strain	0.21
Depth of top reinforcement	0.8 in
Depth of top reinforcement	4.8 in
Depth of burial (ft)	2
Soil Type	Clay
Soil density (pci)	0.0701
Friction angle ϕ	0
Coefficient of static lateral earth pressure K_o	1.0
Soil wave velocity (in/s)	24,000
Damping (Flexure / Direct shear)	20% / 5%



LIST OF REFERENCES

- ACI Committee 318. (2005). *Building code requirements for structural concrete (ACI 318-05) and commentary (ACI 318R-05)*, Farmington Hills, Mich, American Concrete Institute.
- ASCE. (1985). *Design of Structures to Resist Nuclear Weapon Effects*, ASCE Manuals and Reports on Engineering Practice No. 42, ASCE.
- Bathe, K.J. (1996). *Finite element procedures*, Englewood Cliffs, N.J.
- Biggs, J. M. (1964). *Introduction to structural dynamics*, McGraw-Hill, New York..
- Blasko, J.R., Krauthammer, T., and Astarlioglu, S. (2007). “Pressure–impulse diagrams for structural elements subjected to dynamic loads.” *Technical report PTC-TR-002-2007*, University Park, PA: Protective Technology Center, The Pennsylvania State University.
- Bowles, J.E. (1996). *Foundation Analysis and Design*, 5th Edition, McGraw-Hill.
- Clough, R. W., and Penzien, J. (1993). *Dynamics of structures*, McGraw-Hill, New York.
- Crawford, J. E., Holland, T.J., Mendoza, P.J. and Murtha, R. (1983). “A failure methodology based on shear deformation.” *Fourth ASCE Engineering Mechanics Division Specialty Conference*. Purdue University, Lafayette, IN.
- Crawford, J. E., Krauthammer, T., Karagozian, J. and Hinman, E. (1999). “Structural components – Analysis and design examples.” *Structural design for physical security: state of the practice*. Chapter 4, ASCE, SEI, Reston, Va.
- Department of Army (1986). *Fundamentals of protective design for conventional weapons*, Technical Manual No. 5-855-1, Headquarters Department of the Army, Washington, D.C..
- Frye, M. (2002). *Relationships between slender and deep reinforced concrete slabs subjected to short-duration dynamic loading*, MS Thesis, The Pennsylvania State University, PA.
- Hawkins, N.M. (1974). “The strength of stud shear connections.” *Civil Engineering Transactions*, IE, Australia, 39-45.
- Kiger, S.A. (1988). “Ultimate capacity of earth-covered slab.” *J. Struct. Eng.*, ASCE, 114(10), 2343-2356.
- Kiger, S.A., and Getchell, J.V. (1980-1982). “Vulnerability of shallow-buried flat roof structures.” *Technical Report SL-80-7*, five parts, U.S. Army Engineer Waterways Experiment Station, Vicksburg, Miss.
- Krauthammer, T. (1984). “Shallow-buried RC box type structures.” *J. Struct. Eng.*, ASCE, 110(3), 637-651.
- Krauthammer, T., Bazeos, N., and Holmquist, T.J. (1986). “Modified SDOF analysis of RC box-type structures.” *J. Struct. Eng.*, ASCE 112 (4), 726–744.

- Krauthammer, T., Shaana, H.M., and Assaadi-Lamouki, A. (1994). "Response of reinforced concrete structural elements to severe impulsive loads." *Computer & Structures*, 53 (1), 119–130.
- Krauthammer, T. (2008). *Modern protective structures*, Civil and environmental engineering, 22. New York, CRC.
- Mays, G., and Smith, P.D. (1995). *Blast effects on buildings: design of buildings to optimize resistance to blast loading*, T. Telford, London.
- MacGregor, J. G., and Wight, J. K. (2005). *Reinforced concrete: mechanics and design*, Prentice Hall, Upper Saddle River, N.J.
- Meamarian, N., Krauthammer, T., and O'Fallon, J. (1994). "Analysis and design of laterally restrained structural concrete one-way members." *ACI Structural Journal*, 91(6), 719-725.
- Nawy, E.G. (2000). *Reinforced concrete: a fundamental approach*, Prentice-Hall, N.J.
- Newmark, N. M., and Rosenblueth, E. (1971). *Fundamentals of earthquake engineering*, Prentice-Hall, Englewood Cliffs, N.J.
- Ng, P.H. (2004). *Pressure–impulse diagrams for reinforced concrete slabs*, MS Thesis, The Pennsylvania State University, PA.
- Park, R., and Gamble, W.L. (2000). *Reinforced concrete slabs*, Wiley, New York.
- Park, R., and Paulay, T. (1975). *Reinforced concrete structures*, Wiley, New York.
- Slawson, T. R. (1984). "Dynamic shear failure of shallow-buried flat-roofed reinforced concrete structures subjected to blast loading." *Technical Report SL-84-7*, U.S. Army Engineer Waterways Experiment Station, Vicksburg, Miss.
- Smith, P.D., and Hetherington, J.G. (1994). *Blast and ballistic loading of structures*, Butterworth-Heinemann, Oxford, Boston.
- Soh, T.B., and Krauthammer, T. (2004). "Load–impulse diagrams of reinforced concrete beams subjected to concentrated transient loading." *Technical report PTC-TR-006-2004*. University Park, PA: Protective Technology Center, The Pennsylvania State University.
- Tedesco, J. W., McDougal, W. G., and Ross, C. A. (1999). *Structural dynamics: theory and applications*, Addison Wesley Longman, Menlo Park, Calif.
- Terzaghi, K., and Peck, R. B. (1949). *Soil mechanics in engineering practice*, Wiley, New York.
- Zienkiewicz, O. C., and Taylor, R. L. (2005). *The finite element method for solid and structural mechanics*, Elsevier Butterworth-Heinemann, Amsterdam.

BIOGRAPHICAL SKETCH

Kay Hyang Chee was born in Singapore in 1973. He attended secondary school and junior college in Singapore. After obtaining his GCE “A” level in 1991, he served his national service in the army from 1991 to 1993.

He began his undergraduate studies in Civil Engineering at the National University of Singapore in July 1993. He graduated in July 1997 with his Bachelor of Engineering degree in civil engineering. He continued with his graduate studies at the National University of Singapore and obtained his Master of Engineering degree in 1999.

In August 1999, he joined the Defence Science and Technology Agency, Singapore, as a project engineer. In 2006, he was awarded a postgraduate scholarship to pursue a master’s degree in civil engineering, focusing on protective engineering at the University of Florida.